Examining the Atmospheric Transport of Microplastics using the HYSPLIT Model

ERIC WARD

A THESIS SUBMITTED TO
THE FACULTY OF GRADUATE STUDIES
IN PARTIAL FULFILLMENT OF THE REQUIREMENTS
FOR THE DEGREE OF

MASTER OF SCIENCE

GRADUATE PROGRAM IN EARTH AND SPACE SCIENCE
YORK UNIVERSITY
TORONTO, ONTARIO

April 2023

Abstract

Microplastics are tiny particles less than 5 mm in size and are a growing scientific concern, given the potential harm caused across ecosystems as plastic use increases globally. To further understand the atmosphere's role, the HYSPLIT model was utilized to identify differences in transport distance and deposition area by particle size and shape. The extent of microplastic transport and deposition varied significantly by shape for particles larger than 6 µm. Long fibres deposited over a 32% greater area than spherical particles at the largest size of 23.5 µm. The maximum deposition area occurred at 4.5 µm, varying in area by less than 0.25% by shape. As particles smaller than 10 µm have the largest potential to cause adverse health effects, accurately modelling the shape of atmospheric microplastic transport is crucial to determining the range and amount of deposition globally, especially in the 6 µm to 10 µm size range.

Acknowledgements

I would first like to thank Dr. Gordon for his guidance throughout my career at York University. He has taught many courses throughout my undergraduate and graduate studies and has been a great help with this thesis. He always provided a fast and detailed response to any questions I had while still allowing this work to be my own.

I would also like to thank my co-supervisor Dr. Hanson and committee member Dr. Chen for their support and guidance throughout my studies, along with Junhua Zhang at Environment and Climate change Canada for providing the VKT data used in this research.

Thanks to my colleague and friend Rhythm Reet, who has been there throughout my studies at York. Her support, thoughtful suggestions to improve my work and readiness to review my writing when needed are greatly appreciated.

A profound thanks to my parents, who have been tremendously supportive, always wanting to hear how experiments were going and curious to see what I found, no matter the content. Equally, my partner and best friend who has provided confidence and continuous moral support while writing the most difficult portions of this thesis. She pushed me to keep working and to continue growing to be a better scientist and person.

Finally, I gratefully acknowledge the Digital Research Alliance of Canada (formerly Compute Canada), who provided the necessary computer resources, and the NOAA Air Resources Laboratory (ARL) for the provision of the HYSPLIT transport and dispersion model used in this thesis.

Contents

List of Abbreviations

ASCII American Standard Code for Information Interchange

CAPE Convective available potential energy

ECCC Environment and Climate Change Canada

ERF Effective radiative forcing

FLEXPART Model FLEXible PARTicle Dispersion Model

GTA Greater Toronto Area

HYSPLIT Model HYbrid Single Particle Lagrangian Integrated Trajectory Model

NOAA National Oceanic and Atmospheric Association

$PM_{2.5}$ Particulate matter less than 2.5 μm

PM_{10} Particulate matter less than 10 μm

SATP Standard ambient temperature and pressure

TWP Tire wear particles

VKT Vehicle kilometres travelled

VOC Volatile organic compounds

List of Tables

List of Figures

1 -Introduction

Plastic pollution continues to be an ever-growing concern among communities, scientists, and environmentalists alike. Each year the amount of plastic produced worldwide increases as required to meet demand. As of 2019, plastic production was estimated at 460 million tons year^{-1} [OECD, 2019] and showed little slowing. Tiny particles are produced and transferred to the surrounding environment through the daily use, misuse, and disposal of plastic products. Plastic particles smaller than 5 mm are named microplastics and are the focus of this research. Microplastics became an area of concern around 2004, and since then, many scientists have studied them, looking to find their sources, effects, and total global burden [Thompson, 2018].

Like many other anthropogenic pollutants, the ability of microplastics to harm crucial aspects of the environment is becoming a growing issue. Since microplastics are extremely small, little force is needed to lift them into the atmosphere where they can be transported. When airborne, microplastics pose major threats, two of which are direct harm to humans and wildlife through inhalation and as an aerosol with the potential to contribute to effective radiative forcing (ERF). In large urban centres such as Tehran, outdoor microplastic exposure has been estimated to be 3 to more than 500 particles per day [Abbasi et al., 2018]. When inhaled or consumed in large quantities, the less than 10 µm-sized particles can cause adverse effects, including chronic inflammation of lung tissue [Abbasi et al., 2018] and absorption of associated toxic compounds. The radiative effects of microplastics are still in the early stages of research, and with the extreme variability of microplastic compositions and concentration, accurate estimates of the total ERF are relatively unknown. Revell et al., 2021 found that airborne microplastics have an ERF of 0.044 ± 0.399 mW m^{-2} when modelled uniform in density up to 10 km height, but when confined to the lowest 2 km, the ERF was -0.746 ± 0.553 mW m^{-2}. The substantial difference in these values further highlights the challenges faced in predicting the radiative effects of microplastics, particularly as concentration increases with a growing and developing population. Atmospheric microplastics affect the climate even once deposited onto the ground. Plastics transported to more sensitive remote areas such as the Arctic or Antarctica [Aves et al., 2022] can cause accelerated melting of snow and ice due to a lowering of the surface albedo – an effect likened to that of black carbon [Evangeliou et al., 2020]. Although many studies exist today on

microplastics, work on the atmospheric aspect and related effects have only recently been explored as an area of interest [Brahney et al., 2021].

This research contributes to the growing knowledge base of atmospheric microplastics by modelling the transport of various sizes and shapes of microplastics throughout North America and the Arctic. The ability to accurately predict the extent of travel through the atmosphere is critical, as the numerous combinations of shapes, sizes, and materials present difficulty in accurately simulating their transport, as many parameters need to be simplified for large-scale modelling. With the potential harm caused across ecosystems and to all life on the planet, examining the atmospheric component of microplastic transport is an important step in mitigating the damage caused. This study simulates microplastic particles using the HYSPLIT atmospheric dispersion and trajectory model to quantify the potential transport distance and dispersion area based on their size and shape. The steps taken to achieve this goal follow with a detailed literature review, an overview of the HYSPLIT model, methods for the model including the emissions, size, and shape of particles, key graphic results, comparison to related research, detailed numerical analysis of transport area by size and shape, and investigation into the reasoning for changes in transport by shape. Accurate microplastic modelling can help to quantify and further understand the effects of environmental policies to protect vulnerable ecological regions such as the Arctic.

1.1 Related Work

The first major in-situ study suggesting the atmosphere as a critical pathway for microplastic transport was conducted by Dris et al., 2016. Their work primarily involved plastics collected from marine sites, however, the large degree of variation in the microplastics found led to further investigations into the source of these pollutants. Over the past six years, numerous studies have been conducted to explore the role of the atmosphere in microplastic transport. Since 2016, the number of publications related to atmospheric microplastics has increased significantly, and as of early 2022, almost 500 peer-reviewed research articles have been published [Allen et al., 2022]. Even with the yearly number of publications increasing, the complexity and scale of the problem leave significant gaps in knowledge regarding atmospheric microplastic transport. Current challenges in this area are also compounded by the disparity in the methods used for in-situ field

studies, as there is not yet a standard for conducting or reporting experimental data [Allen et al., 2022]. Looking at modelling studies, major gaps in this area include the emission sources, the shapes and sizes modelled, and the equations regarding the deposition of microplastic particles. This thesis provides new data concerning the differences in atmospheric transport by particle size and shape. Modelling studies have been a good start in quantifying the atmospheric microplastic burden, however, more details are needed to reduce the uncertainty in the results [Zhang et al., 2020].

The literature reviewed here provides essential details on the state of atmospheric microplastic research and answers critical questions required to formulate the study in this thesis. The sections follow in order of complexity, beginning with the characteristics of microplastics, how they are formed, and the most common composition of microplastics. Next, specific research on long-range atmospheric transport and deposition quantifies the most common sizes, shapes, and amounts of microplastics in urban and remote regions. Tire wear as a primary plastic is then reviewed for the availability of data and suitability as a large plastic source. Finally, specific details and limitations of current remote deposition data are provided to identify significant knowledge gaps.

1.1.1 Identification of Sources and Microplastic Characteristics

Microplastics consist of a wide range of plastic materials, and there has been much discussion in the past few years on finding a proper definition. A suggested definition describes microplastics as regular or irregularly shaped synthetic particles ranging from 1 μm to 5 mm [Frias and Nash, 2019]. With this definition, sources of microplastics can include primary manufacturing, such as microbeads and glitter, or secondary sources caused by the breakdown of larger plastics, with everyday items being grocery bags, tires, clothes, and bottles. Primary sources of microplastics are more easily identifiable and can be quantified as they are purposely manufactured and sold. Secondary microplastics are more challenging to quantify, as many possible mechanisms are involved. Larger plastics can degrade and emit microplastic particles through physical and chemical means. Physical abrasion creates microplastics from various widely used products, including plastic containers, tires, and shedding from clothes and other

textiles [Brahney et al., 2021]. Chemical changes in large plastics such as discarded grocery bags can make them brittle and susceptible to breaking down into microplastics. A commonly used example is the photodegradation of plastics from solar UV radiation [Revell et al., 2021]. Since microplastics are formed from various substances, determining the quantity emitted into the atmosphere is generally challenging. Previous modelling studies involving microplastics used tire wear particles (TWP) as the primary type of plastic, with climate modelling of exhaust CO_2 emissions and vehicle distance travelled as the primary methods to quantify the global atmospheric microplastic load [Evangeliou et al., 2020]. Compared to other types of microplastics, data related to TWP are more readily available, and as such, TWP are a suitable candidate as a source in modelling microplastic transport.

Two summary review papers by Brahney et al., 2021 and Zhang et al., 2020 examined a wide variety of published research on the atmospheric transport of microplastics. The properties of microplastics were found to vary drastically by location, time, analysis ability, and the methods used to categorize them. As such, the focus was placed on the results from remote locations to ensure the inclusion of microplastics from long-range atmospheric transport. Table 2 from Zhang et al., 2020 showed a greater abundance of fragmented and fibrous particles over other common types and generally ranged in size from 11 μm to 475 μm. Particles below 11 μm were not quantified in either remote study [Bergmann et al.,2019 and Allen et al.,2019], and particles smaller than 4 μm in size have not been quantified in any studies yet, so any implications are all assumed [Brahney et al., 2021]. Table 1.1 lists the relevant findings given by Zhang et al., 2020 and includes studies from urban and rural regions.

Reviewing previous studies gives vital information regarding the size and distribution of microplastics deposited. The size distribution of plastics found in large, populated areas such as London, Dongguan, and Shanghai were much larger than in the two remote regions. Particles found in urban areas ranged in size from 20 μm to over 700 μm, while in the remote regions, most of the sampled particles were less than 300 μm. Furthermore, the shape of microplastics collected varied based on the sample location, with urban areas having more film and foam-shaped particles compared to the remote regions, which mainly had fibres and fragments. The outlier of this trend was the West Pacific Ocean collection, which had the most widespread sample range from 20 μm to 2 mm. The extensive range could be due to the spatial variation in

Table 1.1: Brief summary of in-situ collection studies of microplastics, as presented by Zhang et al., 2020. All studies found some amount of polystyrene, the primary plastic component of vehicle tires. The two highlighted rows represent the two remote studies, while the four remaining were performed in urban areas.

Study area	MP size	shape	Reference
Arctic Europe	11-250 µm >80% ≤ 25 µm	Fibres	Bergmann et al., 2019
Dongguan, China	200-700 µm length	80% Fibres Foams	Cai et al., 2017
London, U.K.	20-25 µm diameter 400-500 µm length	92 % Fibres Fragments	Wright et al., 2019
Pyrenees Mountains, France	100-300 µm length	68% Fragments Fibres	Allen et al., 2019
Shanghai, China	428.81 µm (mean) 121.4 µm (mean)	43% Fibres 48% Fragments	Lui et al., 2019b
West Pacific Ocean	20 µm – 2 mm	60% Fibres 31% Fragments	Lui et al., 2019b

the collection, as a running cruise ship was used as the site in this study. The modelled and in-situ collection of microplastics also provides more detail on the types of plastics found by chemical composition. The review by Zhang et al., 2020 provided the types of plastic found across the collection sites, although there is significant variation in the types over different regions. The most common components (and uses) found in urban China were polyethylene terephthalate (food containers), polyvinyl chloride (pipes), polyethylene (plastic bags), polypropylene (disposable water bottles), polycarbonate (reusable water bottles), and polystyrene (Styrofoam). In European cities, ethylene vinyl acetate (yoga mats) was found alongside many other polymers similarly found in China. In remote regions like the Pyrenees Mountains and European Arctic, polystyrene, polyethylene, ethylene vinyl acetate, rubbers (tires), and polyamides (textiles) were found. Zhang et al., 2020 also indicate little correlation in the types of microplastics found at the various collection sites, and further research is required in this area.

Other experiments further helped identify key size ranges for use in this thesis. Bergmann et al., 2019 found that among other polymers, polystyrene in rubber was a significant contributor to microplastic pollution along the Fram Strait between Greenland and Svalbard. The size and shape of particles found here compared well with Allen et al., 2019 with 80% of analyzed particles being less than 25 µm in size. The minimum recorded size from this study was 11 µm,

however, many particles captured below this size could not be quantified, suggesting the importance of smaller particles in the cumulative concentration. For the largest particle sizes, 3 mm was the longest fibre deposited in the Pyrenees Mountains [Allen et al., 2019b]. The particles collected in the two remote regions studied were predominantly below 250 and 300 μm for the length of fragmented and fibrous particles, respectively. The findings from this review demonstrated that larger microplastics dominated deposition in urban areas, while smaller fragmented and fibrous particles were more abundant in remote regions.

1.1.2 Tire Wear Particles as a Source

Microplastics can be found from diverse sources and at variable concentrations across the planet, as discussed. To formulate a proper study on atmospheric microplastic transport, the source of microplastic emissions must be reasonably quantifiable by the type of plastic, temporally for the emission rate, and spatially for where the emissions occur. Many studies of tire wear particle (TWP) characteristics, emissions, and estimated contributions to global microplastics have been published and are used as background material in this thesis.

TWP are primarily the result of abrasion between a road surface and a rubber tire. The friction between the two materials causes physical wear of the tire and creates particles of various sizes. The larger particles mostly deposit on the road surfaces nearby, while smaller particles may be released as airborne microplastics and transported away from their original source [EPA, 2014]. The specific size range and shape of TWP emitted are critical for this study. A study by Sommer et al., 2018 investigating roadside capture of tire wear found a wide distribution of particles in the 10 μm to 80 μm range. The most common shape here was largely asymmetrical fragments, with very few fibres documented. A general description of the particles was that they are elongated in nature, resembling a cigar [Sommer et al., 2018]. Another study applied the FLEXible PARTicle Dispersion model (FLEXPART) to examine the global distribution of tire wear in the particulate matter less than 2.5 μm ($PM_{2.5}$) and particulate matter less than 10 μm (PM_{10}) size range [Evangeliou, 2020], as these smaller particles remained airborne for longer due to their lower settling velocity. Looking at the abundance of TWP emitted, Baensch-Baltruschat et al., 2020 found that only a small portion of emitted TWP were

transported as airborne particles. They estimated that roughly 5% of the total TWP produced by mass were within the PM_{10} range. Nevertheless, Brahney et al., 2021 provided estimates of the atmospheric burden of microplastics over the western United States to be 1000 tons, with 84% sourced from road, tire, and brake wear emissions. These studies indicate that even with a relatively low emission rate into the atmosphere, the extensive use of vehicles is a significant source of airborne microplastics in the form of TWP. The data presented here will formulate the model settings in this thesis work and act as a proxy for general microplastic transport.

The specific composition of a tire differs depending on numerous factors, including local government policies, weather conditions, type of vehicle, and manufacturer. Getting the exact composition of tires by volume or mass is extremely difficult since it is generally a closely guarded secret by tire manufacturers. As such, the ingredients used in tires have been estimated by Sommer et al., 2018 to follow a simplistic list of the most common components. The primary material of a tire is rubber. This can be natural rubber or, more commonly, a mix of natural and synthetic rubbers, including styrene-butadiene rubber or butadiene rubber. The rubber components comprise roughly 50% of the tire and are the primary plastic or polymer components. The remaining 50% comprises fillers, softeners, vulcanization agents, and additives, including soot, silica, oils, sulphur, and preservatives.

While data concerning TWP are readily available, the limited particle shapes (fragments) of tire wear do not accurately represent microplastics collected from in-situ samples by the proportion of shape. As such, TWP, as described, are used to represent the emissions of a wide range of microplastic shapes and sizes found in different plastics. Fibrous-shaped microplastics are more likely to originate from softer plastics such as polyethylene (plastic wrap), polyamides (textiles), and polyester, although data concerning the emissions of such plastics are relatively unknown.

1.1.3 Transport Measurements

Remote atmospheric transport of microplastics was the focus of two studies performed by Allen et al., 2019 and Bergmann et al., 2019. Allen et al., 2019 focused on the continuous collection of microplastic particles from the remote Pyrenees mountains, while Bergmann et al.,

2019 focused on the Fram Strait and Svalbard regions. The Pyrenees Mountain site was located at the Bernadouze Meteorological Station in the South-West region of France near the Spain-France border. The area surrounding the station had few populated settlements, with the closest town of about 10,000 people located roughly 25 km northeast. Bergmann et al., 2019 included many locations, however, unlike Allen et al., 2019 the site results were discrete samples rather than continuous collection. Surface snow was collected from 14 sites, nine from ice floes in the Fram Strait and five from Svalbard, between 2016 to 2018. The results from these studies help in quantifying the role of the atmosphere in the long-range transport of microplastics and give an initial look into the total deposition of microplastics away from the direct influence of large cities. These studies also help to identify the types and shapes of microplastics found in remote regions. Unfortunately, local results from microplastic collection studies in North America are sparse. Preliminary results have been gathered from an ongoing study in the Canadian Arctic by Granados-Galván et al., 2022 and will be used to discuss and compare the results found in this thesis. The study in the Canadian Arctic involves sample collection from three sites, including Yellowknife, Northwest Territories, Cornwallis Island, Nunavut, and Alert, Nunavut.

A consistent limiting factor in microplastic collection studies globally has been the lack of data on the smallest particle sizes, primarily those under 10 μm. Bergmann et al., 2019 found that 80% of microplastics collected were ≤ 25 μm in size, and the general trend in the number distribution was a decrease in the number of particles for increasing sizes. As such, estimating the microplastic burden of the smallest particle sizes is more complex, and many assumptions are needed for modelling these particles. Overall, the studies done by Allen et al., 2019 and Bergmann et al., 2019 will be the basis for the modelling setup and the comparisons to the results found.

1.2 The HYSPLIT Model

The HYSPLIT model created within the National Oceanic and Atmospheric Administration (NOAA) Air Resources Laboratory is a complete system capable of simulating the atmospheric transport, dispersion, chemical transformations, and deposition of a wide array of constituents [Stein et al., 2015]. The model's name was initially used as an acronym for the HYbrid Single Particle Lagrangian Integrated Trajectory model, with the first edition being

released for use within the NOAA in 1982. However, the initial idea and motivations for a model with trajectory capabilities existed as far back as 1949 for tracking Soviet nuclear testing. Since the first version in 1982, HYSPLIT has undergone four major revisions, with the most recent major update added in April 2020, bringing HYSPLIT up to version 5.0 [NOAA, 2022]. Minor updates to the model's functionality have since been implemented, with the recent distribution of HYSPLIT v5.2.0 acquired for use in this research. HYSPLIT was chosen for this study primarily due to the accessibility of the model, the ability to incorporate a wide array of meteorological data sets, and the ability to incorporate any size or shape of particle. Although more features are present, this thesis discusses only the relevant applications of the model for simulating microplastic transport, with all details and appropriate equations in the following section sourced from Draxler and Hess, 1997.

1.2.1 Governing Equations

This research applies HYSPLIT's hybrid Lagrangian and Eulerian transport, dispersion, and deposition calculations in all model outputs. The hybrid approach utilizes advection and dispersion calculations within a Lagrangian framework and applies the results onto a fixed grid defined by the user. Before the model can perform any dispersion calculations, the meteorological data must be processed to ensure that multiple datasets are specified on the same vertical coordinate system. While specific details on the meteorological datasets can be found in section 2.2.3, the vertical coordinate systems of the three models used in this study were the Global Forecast System (GFS) hybrid sigma-pressure, the North American Mesoscale Forecast System (NAM) pressure, and the High-Resolution Rapid Refresh (HRRR) sigma coordinate system. HYSPLIT modifies these systems onto the internal terrain following sigma coordinate system

$$\sigma = \frac{Z_{top} - Z_{msl}}{Z_{top} - Z_{gl}} \tag{1.1}$$

$$z = 30k^2 - 25k + 5 \tag{1.2}$$

with Z_{top}, Z_{msl}, Z_{gl} being the height at the model's top, at the mean sea level, and ground level, respectively, and k being the model's internal index height. Further interpolating specific

variables depends on the coordinate systems used by the meteorological data. For the GFS and NAM conversion, the following equations apply in finding the ground level, the upper-level air densities, and the vertical motion. These data were provided in detail within the HRRR dataset, so Equations 1.3 – 1.5 were unnecessary in the relevant domain. Height is related to pressure as

$$\Delta z = \frac{\ln\left(\frac{P_1}{P_2}\right) R_d \overline{T_{v12}}}{g} \tag{1.3}$$

with Δz being the height increment as integrated from the hypsometric equation, P_1 and P_2 are the first and second pressure levels, R_d is the gas constant for dry air, $\overline{T_{v1}}$ is the average virtual temperature for the layer, and g is the acceleration of gravity. Additional data for the upper fields were found using the following equations. The air density at a specific level is found using

$$\rho = \frac{P}{TR_d} \tag{1.4}$$

where P and T are the pressure and temperature for the given level, the vertical motion is converted into sigma coordinates by

$$W_\sigma = \frac{W_p}{\rho g Z_{top}} \tag{1.5}$$

where W_p is the vertical motion in units Pa s^{-1}. Fortunately, the meteorological datasets contained the variables required in Equations 1.3 – 1.5, so further modifications were unnecessary. The specific datasets and included variables are further discussed in section 2.2.3.

The advection and dispersion calculations within HYSPLIT depend primarily on the emission type, which comprises individual 3D particles for this study. Linear advection of a particle is applied using the mean wind vectors and follows for each time step as

$$P'(t + \Delta t) = P(t) + V(P, t)\Delta t \tag{1.6}$$

$$P(t + \Delta t) = P(t) + 0.5[V(P, t) + V(P', t + \Delta t)]\Delta t \tag{1.7}$$

where $P'(t + \Delta t)$ is the first guess position, $P(t)$ is the initial position, $V(P, t)$ is the initial wind velocity, Δt is the timestep, $P(t + \Delta t)$ is the final position, and $V(P', t + \Delta t)$ is the wind vector at the final position and time. Figure 1.1 shows an ensemble of trajectories using single tracer

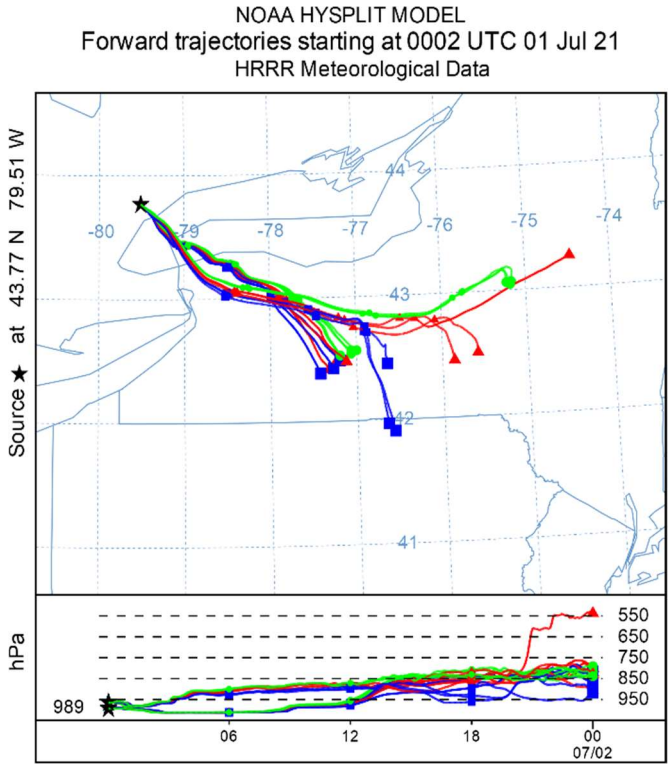

Figure 1.1: A sample ensemble of tracer particles following the linear advection equations. Each model run modified the meteorological grids by 1 grid space horizontally and 0.01 sigma units vertically to get 27 unique tracer paths. The upper plot shows the 2D movement and the lower chart shows the vertical movement in pressure units along the simulation time.

particles in the HYSPLIT model, where the meteorological data fields were modified slightly for each consecutive tracer. The source location used in this example is York University's Keele Campus in Toronto (43.77° N 79.51° W). Based on the equations provided, the tracers demonstrate how individual particles travel in a 3D space and how slight changes in the model data's initial conditions can impact the particles' final transport location.

Equations 1.6 and 1.7 provide the basis for trajectory calculations, however, for more complex dispersion of particles involving turbulent mixing and deposition, different processes must be applied. The first steps in computing the particle dispersion involve finding the boundary layer stability and the mixing coefficients. The method used to find the boundary layer stability depends on the variables present in the meteorological data, however, all follow the same process. The friction velocity and friction temperature are found from the model data or calculated using

$$u_* = \left(\frac{|F|}{\rho}\right)^{0.5} \tag{1.8}$$

$$T_* = \frac{H}{\rho C_p u_*} \tag{1.9}$$

where $|F|$ is the vector momentum flux, H is the sensible heat flux, and C_p is the specific heat constant for dry air. The Monin-Obukhov similarity theory is applied to obtain the stability parameter ($\frac{z}{L}$) relating to the friction values found in the form

$$\frac{z}{L} = \frac{Z_2 k g T_*}{u_*^2 T_2} \tag{1.10}$$

where L is the Obukhov length, k is the Von Karman constant (0.4), and Z_2 and T_2 are the height and temperature at the model's second level, respectively. The equations for the vertical mixing of particles vary depending on the atmospheric stability and the particles' vertical height. Furthermore, the method of calculating the turbulent velocity variance can be chosen from different sets of equations depending on the data available in the meteorological files. In a stable or neutral boundary layer where $0 \leq \frac{z}{L} \leq 10$ using equation 1.10, the calculations follow

$$u'^2 = 4.0u_*^2 \left(1 - \frac{z}{z_i}\right)^{\frac{3}{2}} \tag{1.11}$$

$$v'^2 = 5.0u_*^2 \left(1 - \frac{z}{z_i}\right)^{\frac{3}{2}} \tag{1.12}$$

$$w'^2 = 1.7u_*^2 \left(1 - \frac{z}{z_i}\right)^{\frac{3}{2}} \tag{1.13}$$

where $u'^2, v'^2,$ and w'^2 represent the variance in each vector direction and z_i is the height of the convective boundary layer. Within the lowest level surface layer, the above equations are simplified further to

$$u'^2 = 4.0u_*^2 \tag{1.14}$$

$$v'^2 = 5.0u_*^2 \tag{1.15}$$

$$w'^2 = 1.7u_*^2 \,. \tag{1.16}$$

In an unstable boundary layer with $-2 \leq \frac{z}{L} \leq 0$, the three velocity variances become functions of the convective velocity and follow as

$$W_* = \left|\frac{g u_* T_* z_i}{T}\right|^{\frac{1}{3}} \tag{1.17}$$

$$w'^2 = W_*\left(\frac{z}{z_i}\right)^{\frac{2}{3}}\left(1-\frac{z}{z_i}\right)^{\frac{2}{3}}\left(1+0.5R_h^{\frac{2}{3}}\right) \tag{1.18}$$

$$u'^2 = v'^2 = 0.36W_*^2 \tag{1.19}$$

with W_* being the convective velocity and R_h being the ratio of heat flux at the surface to the heat flux at the inversion, assumed to be 0.2. Within the lowest surface layer, the horizontal velocity variance follows Equation 1.19, however, the vertical velocity variance calculation now follows

$$w'^2 = 1.74u_*^2\left(1-3\frac{z}{L}\right)^{\frac{2}{3}}. \tag{1.20}$$

Along with the equations for turbulence, a small random motion is applied to each particle with every timestep to simulate proper atmospheric dispersion of the pollutants. The total movement of particles between timesteps is then finally calculated by combining the advection equations 1.6 and 1.7 with the turbulent motion into the equations

$$X_{final}(t+\Delta t) = P(t+\Delta t) + U'(t+\Delta t)\Delta t G \tag{1.21}$$

$$Z_{final}(t+\Delta t) = P(t+\Delta t) + W'(t+\Delta t)\Delta t Z_{top}^{-1} \tag{1.22}$$

where U' and W' are the horizontal and vertical turbulent components, G and Z_{top} are conversion factors, $R(\Delta t)$ is an autocorrelation coefficient, $U"$ ($or\ W"$) is a random number generated by HYSPLIT. The associated equations containing the turbulent, autocorrelation, and random number components follow with

$$U'(t+\Delta t) = R(\Delta t)\,U'(t) + U"(1-R(t)^2)^{0.5} \tag{1.23}$$

$$\frac{W'}{\sigma_w}(t+\Delta t) = R(\Delta t)\frac{W'(t)}{\sigma_w(t)} + \frac{W"}{\sigma_w(t)}(1-R(\Delta t)^2)^{0.5} + T_{LW}\big(1-R(\Delta t)\big)\frac{\partial \sigma_w(t)}{\partial z} \tag{1.24}$$

$$\sigma_w(t+\Delta t) = \sigma_w(t) + W'(t)\Delta t\frac{\partial \sigma_w(t)}{\partial z} \tag{1.25}$$

$$R(\Delta t) = e^{(-\frac{\Delta t}{T_{Li}})} \tag{1.26}$$

$$U"(\ or\ W") = \sigma_i \lambda. \tag{1.27}$$

σ_i is the turbulent velocity variance in either the vertical (w) or horizontal (u) direction, T_{Li} is the constant Lagrangian timescale, and λ is Gaussian random number. Since the timestep (Δt) and Lagrangian timescales chosen are constant, the value of $R(\Delta t) \approx 1$ in the horizontal directions and $R(\Delta t) \approx 0$ in the vertical direction. Ultimately this results in the random component $W"$ having a more significant influence in the vertical direction, and horizontal turbulence is based primarily on atmospheric stability and the related equations.

The model output is displayed on static grids of user-defined size. The size implemented for the experiment here is described in the following chapter, although all details of the governing equations remain independent of the chosen size. Air concentration and deposition are calculated using a similar process; however, air concentration is output as an average value for each time interval, and deposition is the sum of all time interval values. Since 3D particles are used in this work, the method for adding to grid cell concentrations follows as

$$dC = \frac{m}{dV(x, y, z)} \tag{1.28}$$

with m being the total particle mass and $dV(x, y, z)$ being the volume of the grid cell. The average concentration of each grid cell would then be the total incremental values found in Equation 1.29 divided by the number of timesteps $(t \times \Delta t)$ over the averaging period. Particles are emitted at a constant rate from emission sources throughout the simulation, with a single particle modelled in HYSPLIT representing a set mass of microplastic emissions from a point location. As such, HYSPLIT employs a mass concentration or amount as the reported value in any data output instead of a number concentration.

2 -Methods

To simulate microplastic transport as accurately as possible, previous in-situ studies were the primary source on which this work was designed. TWP were designated as the microplastic type simulated, as the vehicle kilometres travelled (VKT) data were readily available and contained all the required information, including the gridded data of vehicle travel distance for the entirety of 2011 across the United States and Canada. Particle size and shape parameters were applied within the HYSPLIT model, and the simulation ran for July 2021. The results consisted of 140 shape and size combinations, with the transport distance and coverage area being the primary focus for analysis. Further evaluation of the results was made by comparing the deposition amount to recorded in-situ microplastic collection studies.

2.1 Emissions

Microplastics, by nature, vary significantly in size, shape, density, and composition. As such, estimations of the total production of microplastics and the atmospheric burden are generally unknown. Common microplastics include textiles, packaging, tires, micro-beads, and pellets. To this extent, TWP were the specified plastic in this thesis, which have been found to consist primarily of polystyrene and rubber compounds of numerous sizes and shapes [Panko et al., 2019]. TWP are one of many types of plastics that contribute to the total microplastic burden. They were chosen as the source of plastics because of the availability of VKT data and the work of previous studies. Some studies reviewed provided numerical data, including the average tire wear produced by vehicle type [Sommer et al., 2018] and the proportion of particulate matter less than 10 μm caused by TWP in the range of 0.84 to 10% [Panko et al., 2019]. The emission rates and particle size distributions were then parameterized into the HYSPLIT model using the particle diameter, shape factor, and average density.

2.1.1 Vehicle Kilometres Travelled (VKT)

The use of a CO_2 ratio along with VKT data to calculate tire wear emissions has been used for global estimates of microplastic transport [Evangeliou et al., 2020], however, for evaluating the transport distance over a smaller domain, a more direct approach was applied. This study's emissions data were related to localized traffic density estimated using VKT. The VKT data were provided by Environment and Climate Change Canada (ECCC) and consisted of 10 km square grid cells that covered the entirety of the continental United States (U.S.) and Canada [Zhang et al., 2012]. The data were presented in files separated by the hour and weekday for each month of 2011. Each 100 km^2 grid space contained vehicle travel data in units of km s^{-1}. The units for VKT represent the average total distance travelled by all vehicles over a given time duration. VKT is further divided into three categories of vehicle type. CVKT included all small personal vehicles and was most of the VKT measured at 81% by the total distance travelled. MVKT was designated as all mid-sized vehicles, including vans and personal trucks, totalling ~11% of VKT. Lastly, TVKT was all large transport trucks, public buses and related vehicles, accounting for the remaining ~8% of the total vehicle distance. The designation of VKT by group significantly impacted the total emissions and is discussed further in section 2.1.3. Before these data could be utilized for the emission of microplastics, the files provided had to be processed to get the average VKT for the entire year. All files in the same month were examined to get the average monthly VKT for each vehicle type and grid space. This process condensed

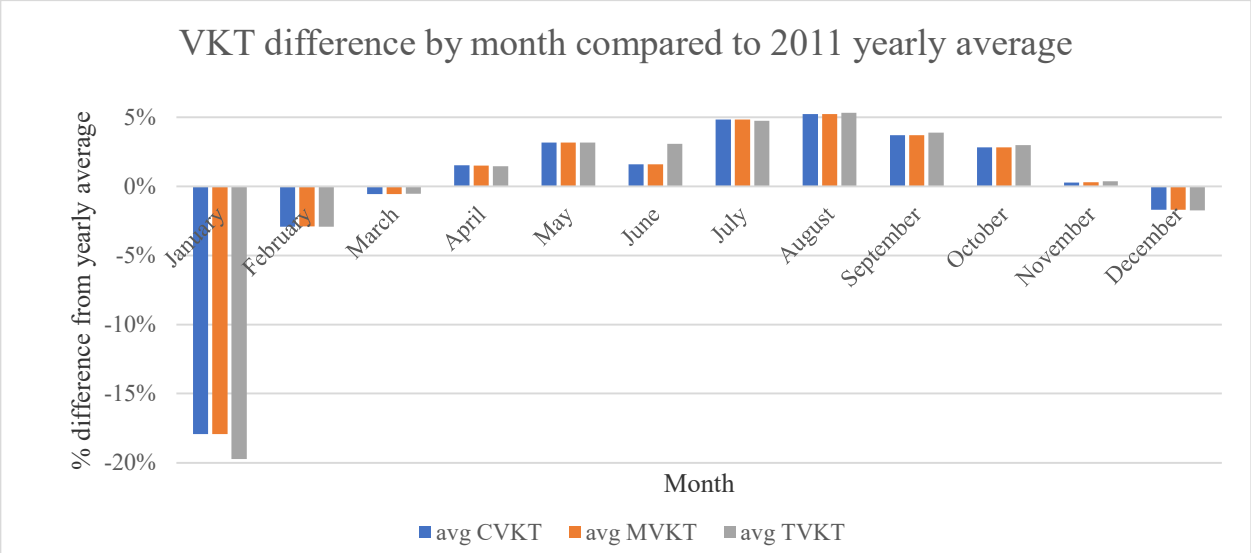

Figure 2.1: A comparison of the relative change in VKT by month for 2011. The average VKT for small vehicles (CVKT), medium sized vehicles (MVKT), and large vehicles (TVKT) are plotted.

the dataset to thirteen records, with twelve consisting of the monthly VKT averages for comparison, as shown in Figure 2.1.

In the final (thirteenth) record, a cumulative yearly average of VKT was obtained, and these yearly average data points were used as the VKT in finding the total amount of microplastics emitted in HYSPLIT modelling. The use of the yearly average allows direct comparison with future work using VKT as an emission source over a different time period. Except for January, the monthly average VKT values all fell within ±5.3% of the yearly average. For a longer-term study, the low difference in VKT would be less significant than other factors, such as meteorological conditions. With the VKT data prepared, the next step was consolidating the domain into manageable emission points for the HYSPLIT model. While the model could use the entire field provided for emissions, reducing the area to include only largely populated metropolitan areas allowed for a more detailed final analysis of total transport distance and the atmospheric load by location.

2.1.2 ArcGIS Spatial Analysis

To determine the emission points for the model, ArcGIS was employed to perform spatial analysis based on the top 100 most populated cities in Canada and the continental U.S. The choice of 100 cities provided a balanced combination of spatially diverse sources of emissions while still being manageable to model and analyze the results. Population datasets of each country's most recent census data were obtained and sorted. This selection gave a minimum city population of 245 000 people, with 18 cities in Canada and 82 in the continental U.S. Due to time constraints, the 2021 census data for Canada was not yet available to be included, so as a result, the 2016 population dataset was used. For the population of the United States, the 2020 census was available for use.

Overlaying the VKT grid and setting the grid values outside the 100 designated cities to zero reduced the total nonzero VKT to 1.9% of the original domain by area, however, it still incorporated roughly 63% of the total VKT (in km s^{-1}) across the emission area. Overlapping cities with nonzero VKT were combined into a single city emission point to simplify the data further. This reduced the number of individual cities from 100 to 67 while maintaining all VKT

data points for the initial 100 cities. For the exact source point for emissions, the coordinates of the centroid of each city polygon were collected from ArcGIS, and these points were used in each model run as the 67 locations, as shown in Figure 2.2. An example of the reduction of individual cities is shown for the Greater Toronto Area (GTA) being modified to one location at the geographic midpoint of the combined cities. Figure 2.3 shows the example for Toronto, with all nonzero VKT grids and the centre point labelled. These simplifications were done to reduce the time and computational power needed in the HYSPLIT model while maintaining the total emissions released.

The locations of the emission points show the general spread of population centres across North America. There are two primary regions with a high number of emission points. The first is on the west coast in California, and the second is a much larger region extending from Tennessee to the eastern Great Lakes basin and the St. Lawrence River in Quebec. The opposite is found in The Great Plains regions of Canada and the United States, with much fewer large cities spread further apart, giving fewer emission points.

Emission source points

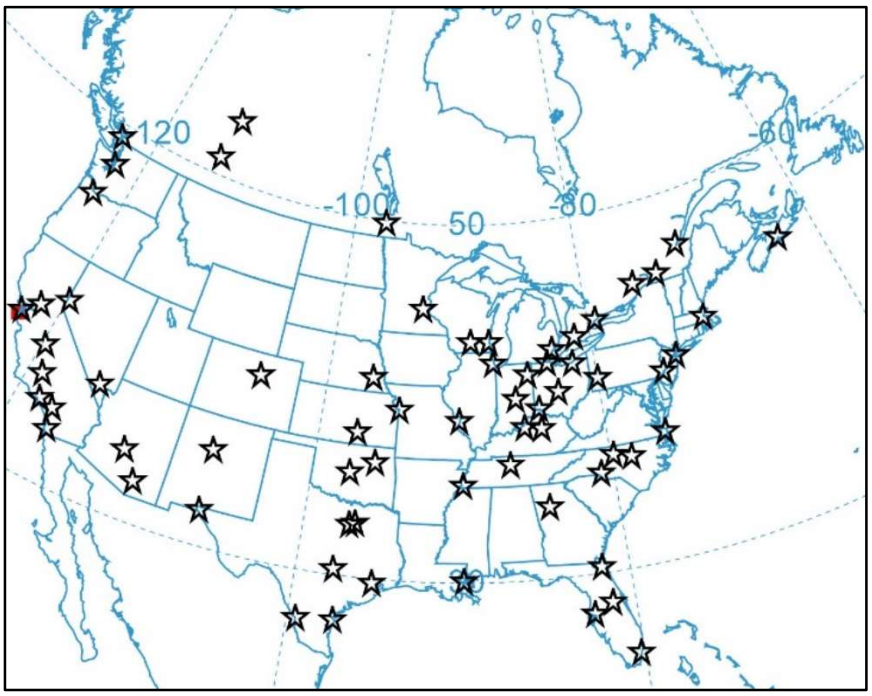

Figure 2.2: The 67 emission points used in HYSPLIT to model atmospheric microplastic transport. The location of emissions corresponds to major cities across the United States and Canada with a minimum population of 245,000 people.

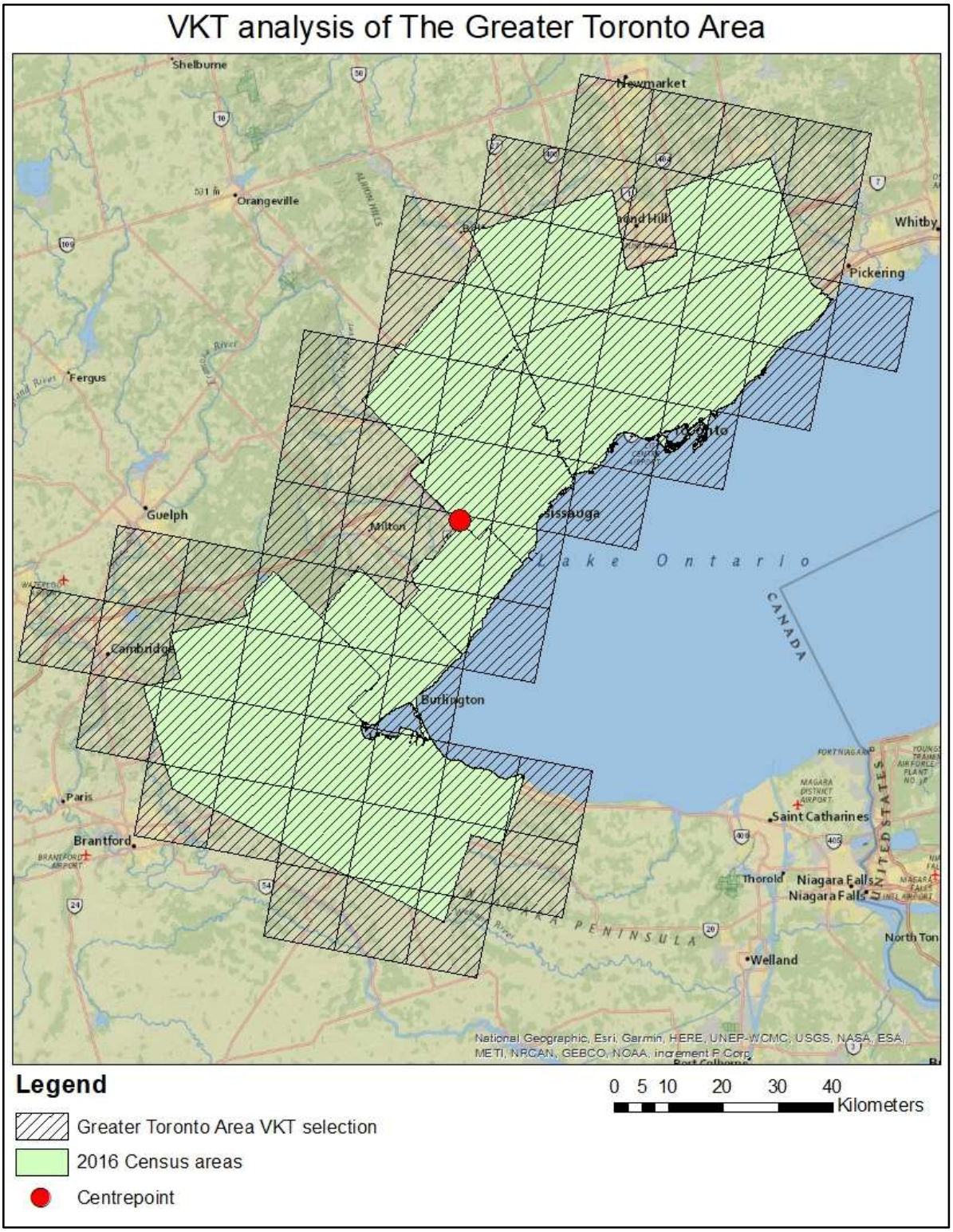

Figure 2.3: Visual representation of the method applied to isolate the VKT grids associated with the largest 100 cities. The selected VKT grids overlapped all city areas and the regions surrounding to account for emissions near city boundaries. The centre point of the VKT grids represented the emission source point used in HYSPLIT.

2.1.3 Tire Wear Particle Emission Rate

The final step before converting the VKT data into emissions for use in HYSPLIT required the review of in-situ tire wear studies. Tire wear collected from several studies showed a significant variation in the mass of particles produced per distance travelled. Baensch-Baltruschat et al., 2020 provided a list of data from these studies (in their Table 1) that included the vehicle type and the emission factor in units of mg km^{-1}. Separating the vehicles into categories by size showed how the emissions varied. Lightweight and mid-sized vehicles (CVKT and MVKT), including motorcycles, cars, vans, and similar-sized vehicles, had emissions ranging from 7 to 360 mg km^{-1}. Heavier vehicles (TVKT), including buses and transport trucks, ranged from 107 to 1500 mg km^{-1}. The considerable variation found can be expected as tire wear emission is a function of several factors, including but not limited to the composition of the tire and road surface, weather conditions, vehicle mass, and driving style. For the work in this thesis, the focus was placed on smaller particles with a diameter of less than 25 μm. For only the fine particles in the PM_{10} range, lightweight vehicle emissions had a much-reduced range of 1.72 to 14 mg km^{-1}, and heavy-duty vehicles had a range of 7.5 to 47 mg km^{-1}. Since the range of emissions varied widely and depended on multiple factors, the average emissions found by Sommer et al., 2018 were used in this work as their estimation included a wider range of particle sizes than those listed by Baensch-Baltruschat et al., 2020. CVKT and MVKT were given an emission rate of 20 mg km^{-1}, and TVKT was set as 200 mg km^{-1}. Converting from the VKT data into the hourly emissions for each city was done using conversion factors and is shown in Table 2.1. VKT grids for each city were summed into a single value for all CVKT, MVKT, and TVKT and then multiplied by their respective emission rate to get a final value for citywide emissions in units of kg hr^{-1}.

Table 2.1: The conversion process applied in changing the VKT values of km s^{-1} into emission values in kg hr^{-1} that HYSPLIT could use. This example shows the data for the cities within the Greater Toronto Area. The yearly average VKT in the three-vehicle classes was converted to TWP mass emissions using the average rate and then finalized in the HYSPLIT required mass and time units of kg hr^{-1} through conversion factors.

Greater Toronto Area emissions	**CVKT**	**MVKT**	**TVKT**	**Total**
Distance (km s^{-1})	1937.29	174.76	204.62	2316.67
Rate (mg km^{-1})	20.0	20.0	200	-
Emissions (kg hr^{-1})	139	12.6	147	**299**

2.2 HYSPLIT

In this study, microplastics were simulated using the HYSPLIT model's particle dispersion and deposition components, allowing for complete control over the atmospheric physics, particle shape and size, domain, and grid sizing, among other parameters. The configuration of the model described here remained constant throughout consecutive runs, with the primary dependent variable being the shape and size of the microplastic particles. The following sections are organized based on the complexity of the parameters involved and the effects of choices on the model results.

2.2.1 Initial Setup

The main setup in HYSPLIT contained all the fundamental inputs to run the model. The model run started at 00Z on July 1st, 2021, and continued until 00Z on July 29th, 2021, to simulate approximately one month of microplastic transport. The total run time was set accordingly, and the vertical method used the meteorological conditions to calculate the vertical particle motion. The sub-menus contained the remaining essential options, including grid sizing and particle data. For the grid setup, the model domain spanned 180° longitudinally and 80° latitudinally, resulting in the south-west and north-east corners of 10°N, 150°W and 90°N, 30°E respectively. A visual depiction of the domain is shown in Figure 2.4. The domain encompasses crucial regions, including North America (apart from western Alaska), Greenland, Iceland, western Europe, northwest Africa, the Atlantic Ocean, and the Gulf of Mexico.

A spatial resolution of 0.081° was chosen for longitude and latitude. In metric units, this converted to grid spacings of approximately 9.0 km by 6.4 km (lat, long) at 45°N. The horizontal grid size was balanced to provide data on the microplastic deposition amount and reduce the time needed to run the model. Vertically, the model extended to 12000 m above ground level, encompassing the majority of the troposphere. Modelling above 12000 m was unnecessary as very few particles lifted above this level, and these were unlikely to settle on the ground within the simulation timeframe. The relatively few particles lifted above 12000 m that would have deposited were primarily due to the wet scavenging of particles within convective clouds.

HYSPLIT domain

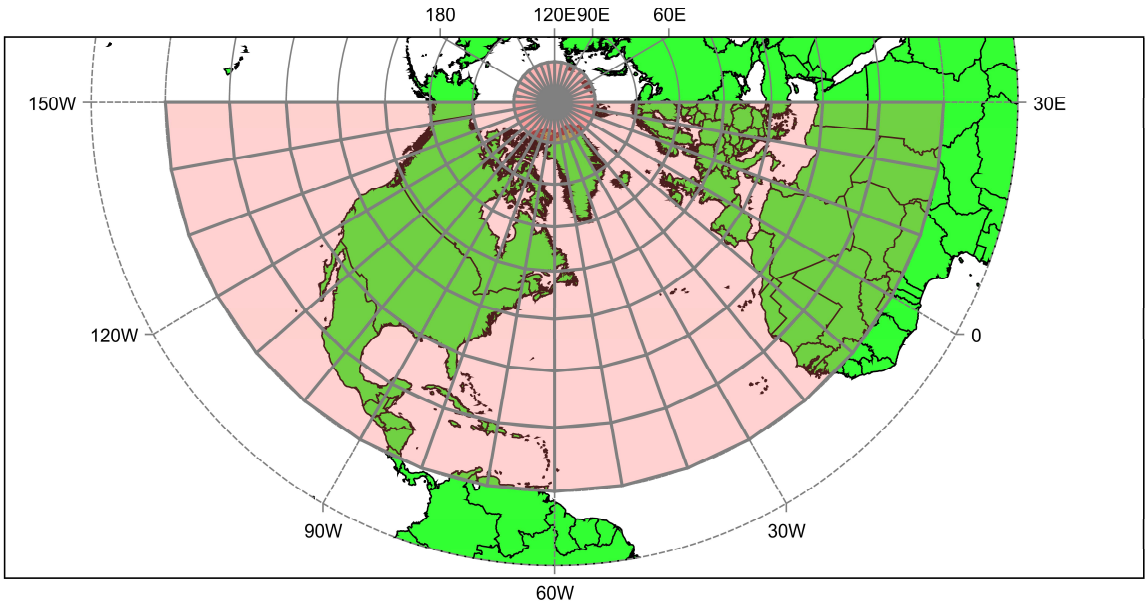

Figure 2.4: The domain used in all HYSPLIT model runs shaded in red. This configuration retained almost all emitted particles for their lifetime and encompassed key areas in the Arctic.

The deposition menu controlled all aspects of the microplastic shape, size, and parameters involving dry and wet deposition. HYSPLIT utilized the particle settling velocity and a probability function for the dry deposition calculations, discussed in the following section. Wet deposition in HYSPLIT is calculated from the following equations,

$$\beta_{wet} = \frac{dC}{dt} = \Lambda C \tag{2.1}$$

where C is the particle concentration in kg m^{-3}, and Λ is the scavenging coefficient in s^{-1} described by

$$\Lambda = Ar^{B} \tag{2.2}$$

where A and B represent the scavenging parameters, and r represents the precipitation rate provided by the meteorological data in mm hr^{-1} [Stein et al., 2015]. The total wet scavenging was separated into in-cloud and below-cloud values, with cloud base and top defined by the relative humidity levels. The cloud base started where the relative humidity exceeded 80% and extended until the relative humidity dropped below 60%. For a dispersed particle size range above 10 μm in diameter, the A scavenging parameter varied with the raindrop and particle sizes through values of 5.0×10^{-5} to 3.5×10^{-4} [Sportisse, 2007]. The default value of A supplied by HYSPLIT

(8.0×10^{-5}) was modified slightly for this experiment, resulting in scavenging parameters of 8.4×10^{-5} for *A* and 0.79 for *B*. As data for microplastic behaviour due to wet scavenging has not been investigated, the values here were chosen as they best applied to general washout and dynamic rainout scavenging. The limitation of this value was the potential for undercounting the total scavenging from a heavy convective rainout. Fortunately, intense convective storms are mostly limited to continental regions within the mid-latitudes, so undercounting deposition due to convective rain is likely limited to small regions close to sources. A relatively moderate *A* value ensures microplastic deposition due to wet scavenging is accounted for, while not limiting the transport of particles due to less intense precipitation events.

2.2.2 Size, Shape and Deposition

Evaluating all data presented and discussed in section 1.1.1, the size range for microplastic particle size used in this study was from 2 to 25 µm. This range allowed for comparisons with previous studies while limiting the larger particle sizes that were insignificant for long-range atmospheric transport. The results from particulate matter in the $PM_{2.5}$ and PM_{10} size groups were also included as focal points in the results, as these are most impactful to human and wildlife health [Akhbarizadeh et al., 2021]. The specific sizes were chosen with bins applied in HYSPLIT. The initial bins chosen were 2.56, 5.12, 10.24, and 20.48 µm to match the bin sizes in Zhang et al., 2018. This was done to keep the bin sizing in line with other related studies and provide some ability to compare results. The specific study by Zhang et al., 2018 focused on multiscale air quality modelling of volatile organic compounds (VOC) at different particle sizes. In this thesis, twenty particle sizes were calculated from the four bins, resulting in five particle sizes per bin and a size distribution arranged by HYSPLIT in a $\frac{dV}{d(\log(r))}$ format. All references to the particle size in this thesis indicate the diameter of an equal-volume sphere rather than the diameter of a specific shape. The spherical particle diameters, according to the four bins, ranged accordingly from 1.68 to 2.94 µm, 3.38 to 5.89 µm, 6.76 to 11.76 µm, and 13.51 to 23.53 µm. Twenty sizes were chosen as they provided a reasonable distribution of particle diameters, with the largest size gap being 3.04 µm. Fewer sizes risked being unable to produce demonstrable results, while more than twenty sizes were unnecessary, as increasing the

number of particle sizes one step further to twenty-eight only reduced the largest gap to 2.35 µm. The additional increase in computation time required to run the additional eight sizes further affected the final choice. The twenty sizes give a particle size range of 1.68 µm to 23.53 µm.

For parameterization of the shapes, an assumption was made that all non-spherical particles were represented as cylindrical for simplicity and to more easily identify how particle shape changes the total distance travelled and coverage area. To include a variety of shapes, two aspect ratios each were used to signify fragments and fibres. The length for the first fragment was gathered from the modal aspect ratio of TWP found in a comparison of previous studies by Kreider et al., 2010. Further research by Sommer et al., 2018 found that over 90% of elongated TWP analyzed had an aspect ratio of <0.6 ($a = d/L$). The second fragment was given an aspect ratio half of the first to simplify the scaling of sizes and apply the results of Sommer et al., 2018 resulting in aspect ratios of 0.64 and 0.32. The two fibrous shapes were modelled using aspect ratios of 0.1 and 0.01 for a factor of 10 difference. Table 2.2 demonstrates all twenty sizes and the respective diameters of the cylindrical particles based on the sphericity. The cylindrical diameters were found using Equation 2.3 below. The final column lists the equal spherical diameters (d_{eq}) of long fibres with a particle diameter (d) equal to the HYSPLIT particle size and aspect ratio of 0.01 to sample larger particle sizes. An equivalent volume sphere was included to find differences in atmospheric transport between the larger long fibres with equal mass.

To input these values into HYSPLIT, the aspect ratios were converted to a sphericity factor, a ratio of the surface area of a sphere with equal volume to the surface area of the chosen particle. The sphericity factor varied from 0 to 1, with 1 representing a perfect sphere. The equation for the sphericity of a cylinder follows

$$\phi = \frac{\pi d_{eq}^2}{A_{Cylinder}} = \frac{\pi \sqrt[3]{\left(\frac{3d^2L}{2}\right)^2}}{\pi dL + 2\pi\left(\frac{d}{2}\right)^2} = \frac{\sqrt[3]{a\left(\frac{3}{2}\right)^2}}{1 + \frac{a}{2}} \tag{2.3}$$

with d_{eq} representing the diameter of a sphere with the same volume as the particle, $A_{Cylinder}$ representing the surface area of the cylindrical particle, L and d are the length and diameter of

the cylindrical particle, respectively, and a is the aspect ratio. Figure 2.5 shows a scaled comparison between all shapes, with the base length representing one spherical diameter.

Table 2.2: All particle shapes and sizes modelled within HYSPLIT. Sphericity and aspect ratio were used to find the diameters of the cylindrical particles. The final column represents the diameter of a sphere with an equivalent volume to the long fibre. Bins separate the groups of particle sizes.

Sphericity (ϕ)	**1**	**0.85**	**0.77**	**0.58**	**0.28**	**1 & 0.28**
Aspect ratio(a=d/L)	N/A	0.64	0.32	0.1	0.01	N/A & 0.01
Shape	Sphere	Short Fragment	Long Fragment	Short Fibre	Long Fibre	Equal diameter long fibre & equal volume sphere
HYSPLIT particle size (μm) ↓	Diameter (μm)	Diameter (μm)	Diameter (μm)	Diameter (μm)	Diameter (μm)	Diameter (μm)
1.68	1.68	1.27	1.01	0.685	0.318	8.99
1.94	1.94	1.46	1.15	0.787	0.365	10.3
2.23	2.23	1.67	1.33	0.904	0.420	11.9
2.56	2.56	1.92	1.53	1.03	0.482	13.6
2.94	2.94	2.21	1.75	1.19	0.553	15.7
3.38	3.38	2.54	2.01	1.37	0.636	18.0
3.88	3.88	2.92	2.31	1.57	0.730	20.7
4.46	4.46	3.35	2.66	1.80	0.839	23.8
5.12	5.12	3.85	3.05	2.07	0.964	27.3
5.88	5.88	4.42	3.51	2.38	1.11	31.4
6.76	6.76	5.08	4.03	2.73	1.27	36.0
7.76	7.76	5.84	4.63	3.14	1.46	41.4
8.91	8.91	6.71	5.32	3.61	1.67	47.5
10.24	10.24	7.71	6.12	4.15	1.92	54.6
11.76	11.76	8.85	7.02	4.76	2.21	62.7
13.51	13.51	10.17	8.07	5.47	2.54	72.0
15.52	15.52	11.68	9.27	6.29	2.92	82.7
17.83	17.83	13.42	10.65	7.23	3.35	95.0
20.48	20.48	15.42	12.23	8.30	3.85	109
23.53	23.53	17.72	14.06	9.54	4.42	125

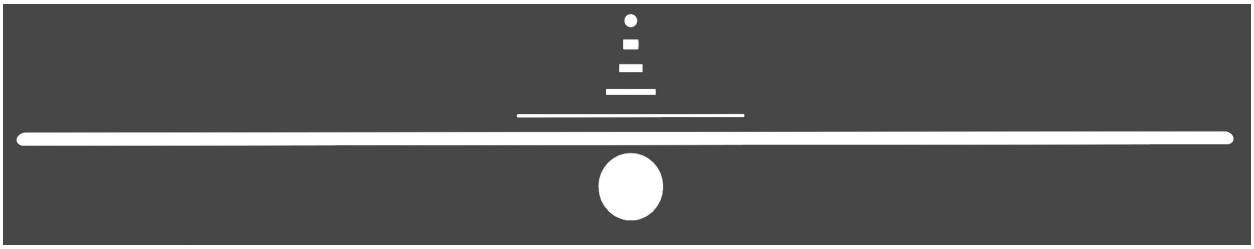

Figure 2.5: A diagram showing the difference in size based on the aspect ratio in Table 2.2. A sphere with diameter d is on the bottom, followed by the short fragment ($a = 0.64$)*, long fragment* ($a = 0.32$)*, short fibre*($a = 0.10$)*, long fibre*($a = 0.01$)*, and long fibre/sphere of equal diameter/volume. All shapes here are scaled to their relative size.*

As discussed earlier, HYSPLIT separates deposition into categories of wet and dry. For the dry deposition calculations, the vertical settling velocity of the particles followed Ganser, 1993 as

$$k_1 = \left(\frac{1}{3} + \frac{2}{3}\phi^{-0.5}\right)^{-1} \qquad k_2 = 10^{1.8148(-\log(\phi))^{0.5743}} \tag{2.4}$$

$$C_D = k_2\left(\frac{24}{\alpha}(1 + 0.1118\alpha^{0.6567}) + \frac{0.4305}{1 + \frac{3305}{\alpha}}\right) \qquad \alpha = Rek_1k_2 \tag{2.5}$$

$$Re = \frac{\rho_f U d_p}{\mu} \tag{2.6}$$

$$U = \sqrt{\frac{4d_p g(\rho_p - \rho_f)}{3\rho_f C_D}} \tag{2.7}$$

where k_1 and k_2 are Stoke's and Newton's shape factors for non-spherical objects, C_D is the drag coefficient, Re is the particle Reynolds number, $d_p$is the particle size, g is gravitational acceleration, ρ_f and ρ_p are the fluid and particle densities, μ is dynamic fluid viscosity, and U is the final settling velocity of the particle. This set of equations was not the default method used by HYSPLIT, however, the modifications applied by the shape factor in Equation 2.4 were applicable for a broader range of particle sizes as they included Stoke's and Newton's shape factor. Further detail on the dynamics involved and the implications of the results are discussed in section 4.3. The unknown values, including the fluid density and dynamic fluid viscosity, were estimated using the applicable meteorological data used for the modelling, while the

particle diameter, density, and sphericity were set in the model. The particle density was chosen to be 1.26 g cm^{-3} from the average density found in in-situ TWP [Sommer et al., 2018]. Figure 2.6 shows the settling velocity of all particle shapes and sizes at the standard ambient temperature and pressure (SATP) using the above values and equations. The figure was created using code through an iterative process to solve Equations 2.5 to 2.7 and has a maximum computation error of ± 1.0×10^{-4} cm s^{-1}. The smallest long fibre (size of 1.68 µm) had the lowest settling velocity at just 6.93×10^{-3} cm s^{-1}. The sphere with the same volume had a settling velocity of 1.10×10^{-2} cm s^{-1} or 1.6 times faster velocity. At the largest size of 125 µm, the long fibre and equivalent volume sphere had settling velocities of 20.4 cm s^{-1} and 46.9 cm s^{-1}, respectively, with the sphere settling velocity 2.3 times faster than the long fibre settling velocity. All other particle shapes fit between the listed values, as shown below in Figure 2.6.

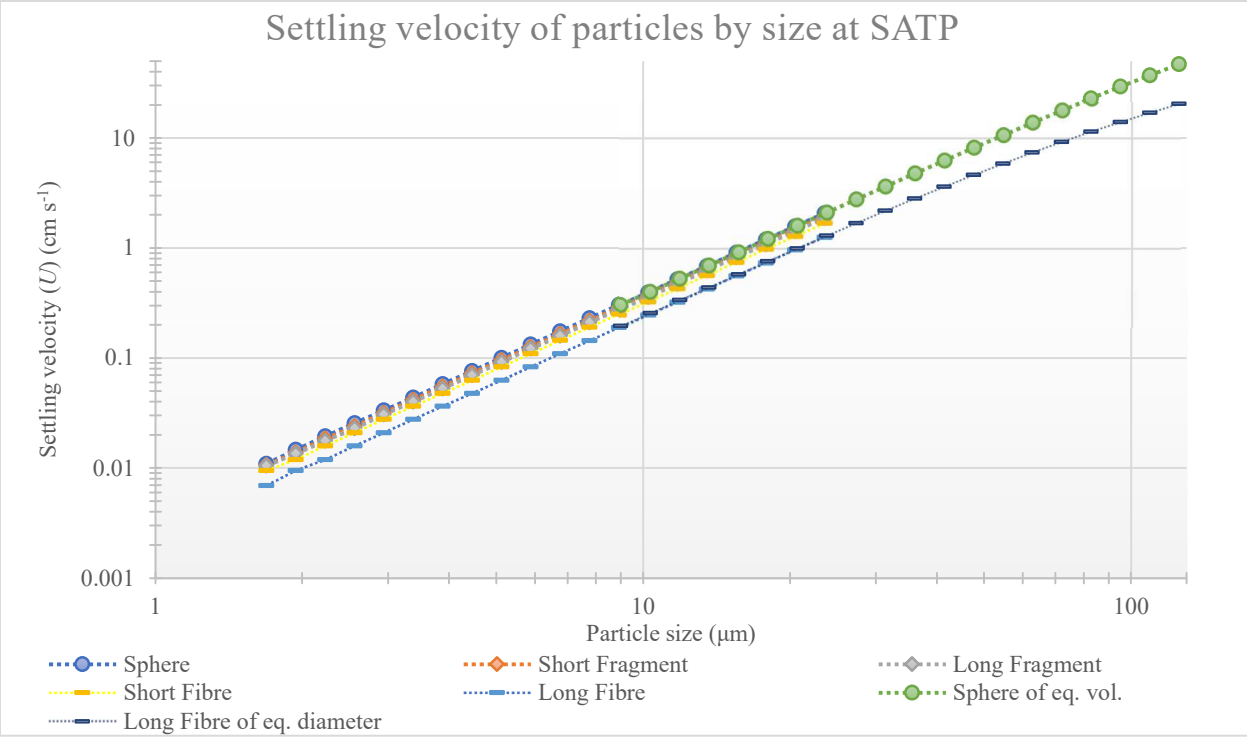

Figure 2.6: The settling velocity of all particles on a log-log plot as found using equations 2.4-2.7. All velocities were found using the standard temperature and pressure of 288.15 K and 101,325 Pa. When modelled using real-world meteorological data, the velocities would fluctuate as a function of temperature, pressure, and viscosity.

The final set of equations below was the method applied within HYSPLIT to calculate the total deposition rate.

$$\beta_{dry} = U\Delta Z_p^{-1} \tag{2.8}$$

$$M_{Total} = m(1 - \exp[-\Delta t(\beta_{dry} + \beta_{wet})]). \tag{2.9}$$

Here β_{dry} is the dry removal constant calculated as a function of the settling velocity, U, and the air concentration of particles within the surface layer of size ΔZ_p. The total deposition equation is applied within each grid cell and includes m as the simulated particle mass within the lowest layer, Δt as the time step (60 seconds), and $\beta_{dry}\ and\ \beta_{wet}$ as the two rate constants. Only the dry rate constant was a factor in grid cells with zero precipitation. As a simulated particle entered and travelled within the surface layer, mass was reduced from the particle and added to the total deposition in each timestep based on these equations. In this method, fewer particles were needed in the model to simulate the mass of all emission sources, as calculated previously.

2.2.3 Meteorology

For the meteorological data, all were sourced from the NOAA's HYSPLIT database [NOAA, 2022b] and consisted of three models, namely the Global Forecast System (GFS), North American Mesoscale Forecast System (NAM), and High-Resolution Rapid Refresh (HRRR). The GFS was included as the global model with key features of 0.25 degree (~28km) horizontal resolution, 55 vertical pressure levels, and model outputs of 3-hour intervals, with the model being run every 6 hours. The GFS was used for all meteorological parameters in the long-range transport as the particles travelled outside the two higher-resolution model domains. The high-resolution models focused on the continental United States and southern regions of Canada, where the initial emission areas were set up. The NAM was included to act as a buffer between the high-resolution 3 km HRRR and the lower-resolution GFS, as initial HYSPLIT runs demonstrated a noticeable area of particle deposition following the outline of the HRRR domain. The increased deposition here was likely due to the sudden change in winds and precipitation between the models and is noted accordingly in the results. The NAM had spatial resolutions of 12.2 km horizontally, which fit roughly halfway between the GFS and HRRR resolutions.

Temporally it was the same as the GFS, with model outputs every 3 hours and running every 6 hours. The final model was the HRRR, with a much higher horizontal resolution of 3 km and 36 vertical levels using the sigma coordinate system, all run hourly for much higher temporal resolution compared to the NAM or GFS.

Along with the improved resolution, the HRRR and NAM also included a convection parameter in the form of the convective available potential energy (CAPE), which allowed HYSPLIT to apply enhanced vertical mixing in the two higher-resolution domains. The variables used by all three datasets include the temperature, pressure, relative humidity, and the wind in each of the u, v, w components at each vertical level. At the surface, variables included are the pressure, surface height, temperature, specific humidity, wind and momentum flux in the u, v components, 6-hour precipitation total, sensible and latent heat flux, short wave radiation flux, cloud cover percentage, friction velocity, and the surface roughness. All meteorological files were applied for the simulation duration from July 1st to 29th, 2021. Figure 2.7 shows the coverage of the higher-resolution HRRR and NAM models. Both model domains covered all of the United States and southern regions of Canada, as discussed, while the GFS domain covered the remaining HYSPLIT domain.

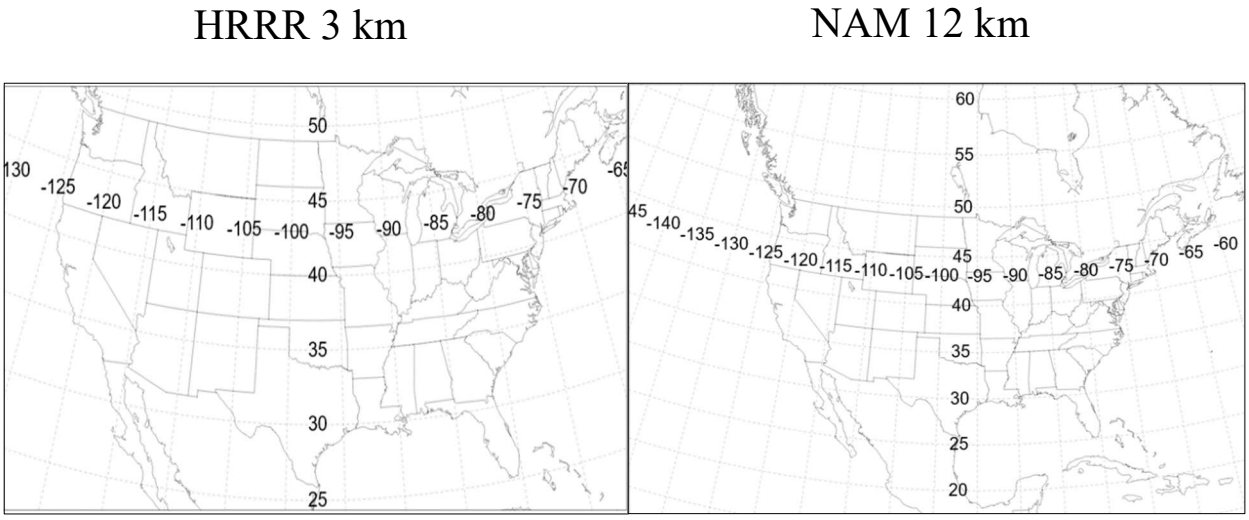

Figure 2.7: a) Spatial domain for the HRRR meteorological data, which covers the entire continental US and extreme southern regions of Canada. All sources are contained within this domain except for Edmonton, Alberta. b) Spatial domain of the NAM meteorological data. This domain extends further in all directions from the HRRR domain.

One caveat of using multiple meteorological datasets occurs as particles are transported between model domains. Model data update intervals change from 1 hour to 3 hours between the HRRR and NAM. This change means particles transported between the models could encounter temporal changes in wind conditions of up to 2 hours difference and spatial changes as the model grid sizing increases from 3 km to 12.2 km. A similar change occurs between the NAM and GFS, where spatial resolution decreases from 12.2 km to ~28 km, although the update intervals are temporally equal, once every 3 hours. The primary effect of changes in the wind data is a sudden increase or decrease in the deposition field in the areas adjacent to the HRRR and NAM domains. Using a single global dataset would eliminate the discontinuity at the cost of losing the high-resolution meteorological data within the continental regions of North America.

2.2.4 Additional Parameterizations and Model Run

The advanced setup of the model made slight changes from the default configuration to ensure consistency between the model runs and proper parameterization for simulating microplastic transport. The timestep was changed from an advection ratio, the maximum fraction of a grid cell that a particle was allowed to travel per time step, to the minimum set value of one-minute to reduce any possible integration errors and timestep differences between model runs. A set timestep value also ensured the emissions occurred at the same rate and time in each separate model run. As previously discussed, the proportion of TWP produced that was emitted as small airborne particulate matter (PM_{10}) was relatively low, at roughly 5% [Baensch-Baltruschat et al., 2020]. As such, the emission cycling was set to release particles for the first six minutes of each hour, simulating the airborne microplastic proportion of TWP to be 10% of the total produced as a function of VKT. It also reduced the total particle count and the compute time required to complete the simulation as the model tracked each particle. The lack of data concerning the residence time of airborne microplastics was another significant consideration in the model setup. Since the residence time largely depends on the aerodynamic shape and size and the meteorological conditions present, estimates varied significantly. Brahney et al., 2021 estimated that road sources such as TWP had residence times of 1 hour to 2.9 days, while all microplastics ranged from 1 hour to 6.5 days. The smallest particle size simulated in that study was 0.3 μm, much smaller than this research at 1.68 μm. For this study, the maximum particle simulation

time was set to 12 days to account for the reference study's differences in methods and meteorological conditions.

Each model run was set with two phases: an emission phase and a transport phase. From July 1st to July 21st, particles were emitted each hour to simulate the continuous release of microplastics. For the remainder of the month, emissions were removed, and the model simulated the transport of the remaining particles to ensure every introduced particle was accounted for in the long-range transport. The total simulated mass of microplastics in every run was found by summing each city's emissions, as demonstrated in Table 2.1. The total emission rate was 810 kg hr^{-1} (or 40.5 kg hr^{-1} for each of the twenty particle sizes). For 21 days of emission, the total mass amounted to 0.409 kT or 0.0204 kT per particle size. The emission rate and total mass data were used to compare and verify this study with the modelling data from Evangeliou et al., 2020 as detailed in section 2.3.

HYSPLIT modelled particle dispersion using Equations 1.21 to 1.27, as described in section 1.2.1. The calculation of the turbulent velocities u'^2, $v'^2$and w'^2 utilized equations by Kantha-Clayson, 2000, which were chosen based on recommendations from the HYSPLIT user guide and the meteorological data required. The Kantha-Clayson equations required the momentum and heat fluxes to calculate the turbulence, which were found in all three meteorological datasets. Other methods of calculating the turbulence required variables that were not readily available in the meteorological datasets and would have meant additional calculations were needed, adding to the model run time. Furthermore, the Kantha-Clayson equations were the most recent addition to HYSPLIT and have been the recommended method for general dispersion purposes.

The model was executed entirely on the Graham compute cluster managed by The Digital Research Alliance of Canada (formerly Compute Canada before April 1st, 2022). Modifying variables and running the model was accomplished through scripts and batch files submitted to the cluster. The scripts modified the shape and size parameters according to the distribution described earlier, resulting in 140 raw concentration files from the five shapes and twenty sizes. For each model run, the computational time required averaged around 106 hours per CPU core. In total, the time required to produce all concentrations files was approximately 1.7 core years (A core year is equivalent to using 1 CPU core for a full year). The concentration files were

converted to ASCII format for analysis using a built-in HYSPLIT utility. The ASCII files included the sum for each grid cell with nonzero deposition in units of μg m^{-2}. Numerical analysis of these data was used to find the total deposition area, the ratio of emitted to deposited mass, and the furthest extent of transport relative to the emission sources.

2.3 Comparisons

Once the results were analyzed, comparisons to in-situ and other modelling studies were made. Most microplastic collection studies have focused on Europe [Allen et al., 2019, Bergmann et al., 2019], so general assumptions were made based on the distance between the study site and nearby large urban areas. As mentioned in section 1.1, research on microplastic collection in the Canadian Arctic is ongoing, and preliminary results from the study by Granados-Galván et al. 2022 are included here in this thesis. One of the main limiting factors in comparing studies was that the in-situ collection was reported using number concentration in units of particles per litre (# L^{-1}) or in particles per metre squared per day (# m^{-2} d^{-1}). In contrast, the HYSPLIT output was in mass units for the total monthly deposition. An average mass per particle was applied to the HYSPLIT results to convert to a number amount, however, this used the constant particle density of 1.26 g cm^{-3} [Sommer et al., 2018]. Further discrepancy between this study and the in-situ collection originated from factors such as seasonality, variable particle emission rates, and the methodology applied in collecting and analyzing particles. A direct comparison of this study's results to the real-world collection should be interpreted with these conditions in mind.

The study performed by Evangeliou et al., 2020 has the most similarities to this study and was used as a comparison. The study analyzed global microplastic deposition in the $PM_{2.5}$ and PM_{10} ranges for TWP using the FLEXPART model, with the results in units of deposition by mass. Specific comparisons were made between the microplastic emissions and deposition to this work in the relevant geographical areas. Since the study by Evangeliou et al., 2020 assumed spherically shaped particles, a direct analysis between the studies could only be applied to the similarly sized spherical particles in this work. The main differences between the models were the grid sizing, model run time, total emissions, and the location of emissions. The grid sizing from Evangeliou et al., 2020 was set to uniform 0.5°x0.5° grids, roughly 38 times larger than the

grids used in this study. Emissions were also set for each grid space, whereas this study had set sources based on population centres. The results from Evangeliou et al., 2020 were plotted as annual deposition amounts, meaning the results from this study needed to be extrapolated to get an estimate for the total yearly deposition. Finally, the particle diameters modelled differ slightly between the studies. For the numerical comparison, particle diameters of 2.1 μm and 9.5 μm were chosen from Evangeliou et al., 2020 model data, and 2.23 μm and 8.9 μm particle diameters were chosen from this work. With these factors considered, the main goal of the comparison was to look at the overall trend in deposition across the relevant domain.

3 -Implementation and Results

The model results were separated into categories based on the particle shape. Deposition and particle distribution plots of the smallest and largest bin sizes of 2.56 µm and 20.48 µm for each shape are shown, as they show the extent of the modelled data near the smallest and largest particle sizes. For the statistical analysis of the results, all twenty sizes per shape and five shapes were included for a total of 140 data points. The analysis included comparing the total deposition area, the maximum transport distance, and a comparison of results between previous research by Allen et al., 2019, Bergmann et al., 2019, Evangeliou et al., 2020, and preliminary results from Granados-Galván et al., 2022.

3.1 Size and Shape Factor

The plots in Figure 3.1 demonstrate the deposition for the fives shapes at two sizes during the simulation. The plots are separated into four panels based on particle size, with the sizes equal along the columns of panels of each figure. The deposition amount was drawn according to a logarithmic scale ranging from 0.1 µg m-2 to greater than 1000 µg m-2 of microplastics to provide a straightforward visual comparison between plots. The minimum value of 0.1 µg m-2 was chosen as it provided the most practical plots regarding the deposition area. A smaller value of 0.01 µg m-2 created significant noise in the plots and reduced the comparability of the particles by different sizes. The plots follow the order in Table 2.2 from spherical to short and long fragments, to short and long fibres, and finally, the equivalent volume sphere for long fibres. Two sizes for each sphericity are shown to visually compare small and large particles, resulting in fourteen plots. The first five plots on the left are of a particle size of 2.56 µm, and the plots on the right are of 20.48 µm. In the last plots for the equivalent diameter long fibre and equivalent volume sphere, the particle sizes are 13.64 µm on the left and 109.2 µm on the right.

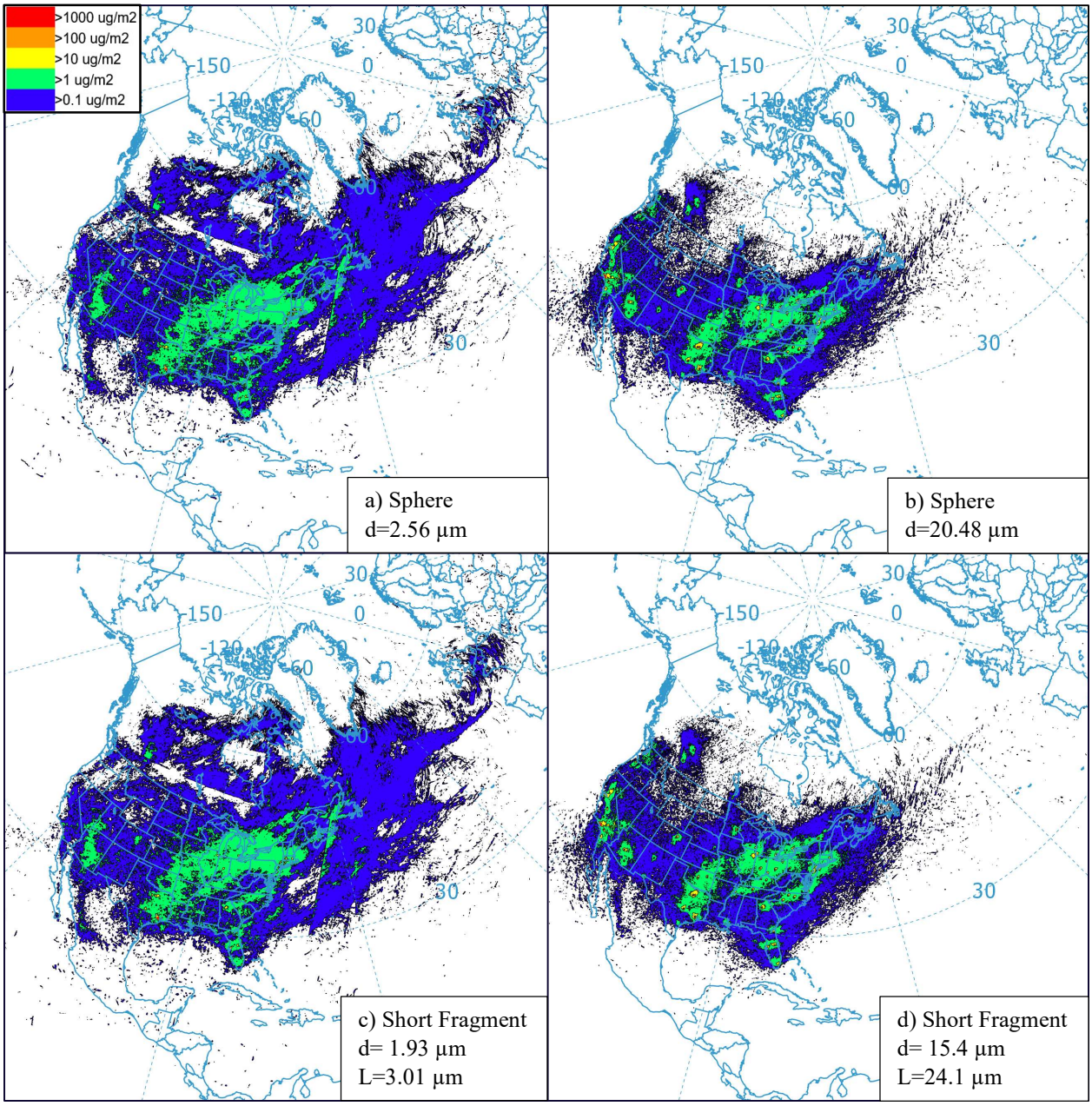

Figure 3.1: Fourteen individual frames showing the total deposition amounts from July 2021 of two microplastic sizes across the domain. The first ten frames are particles in descending order of particle shape, beginning with the spheres. The final two frames show the spheres of equivalent volume to the long fibres. All frames overview the same area at a constant scale for ease of comparison.

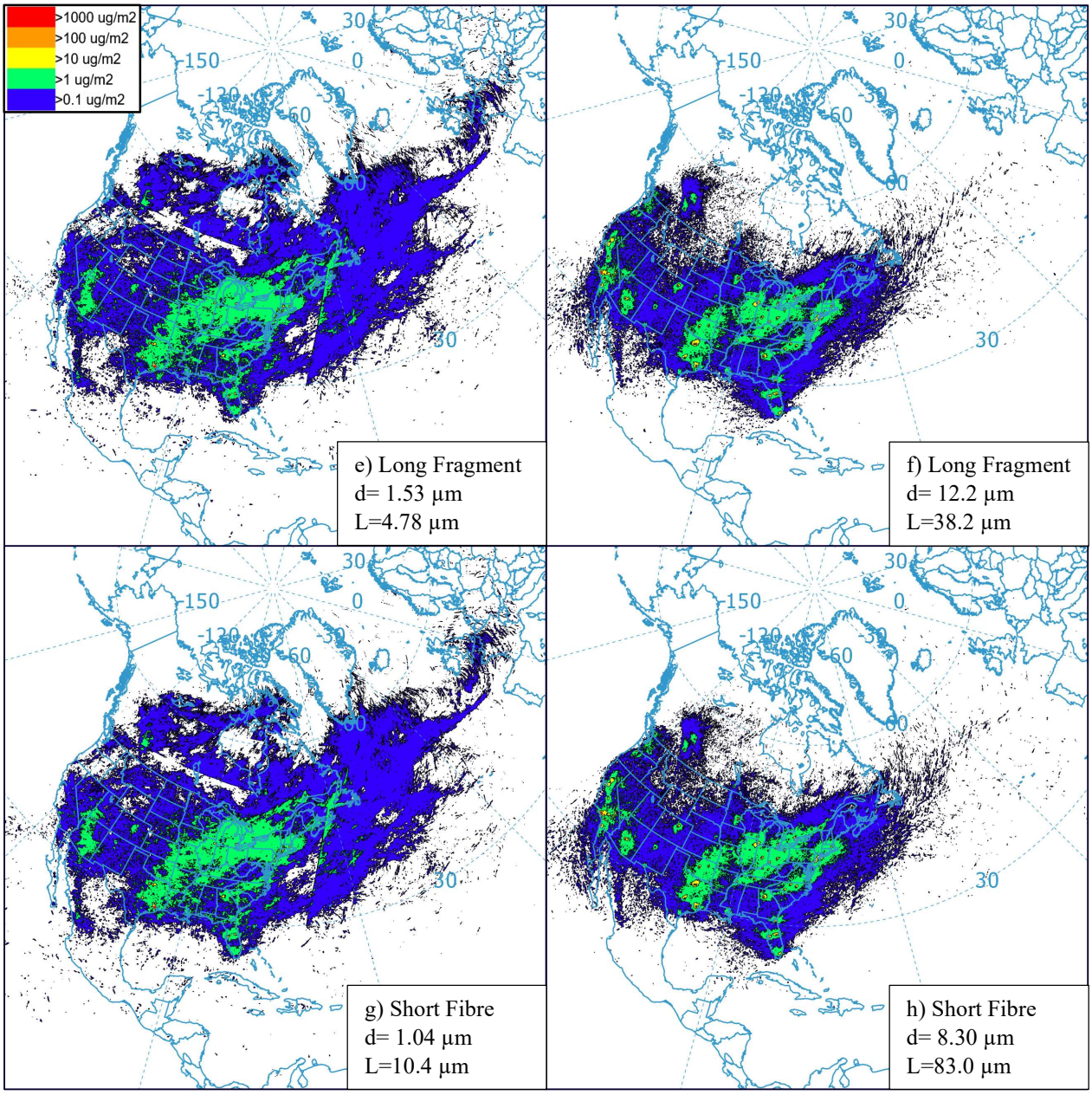

Figure 3.1 continued

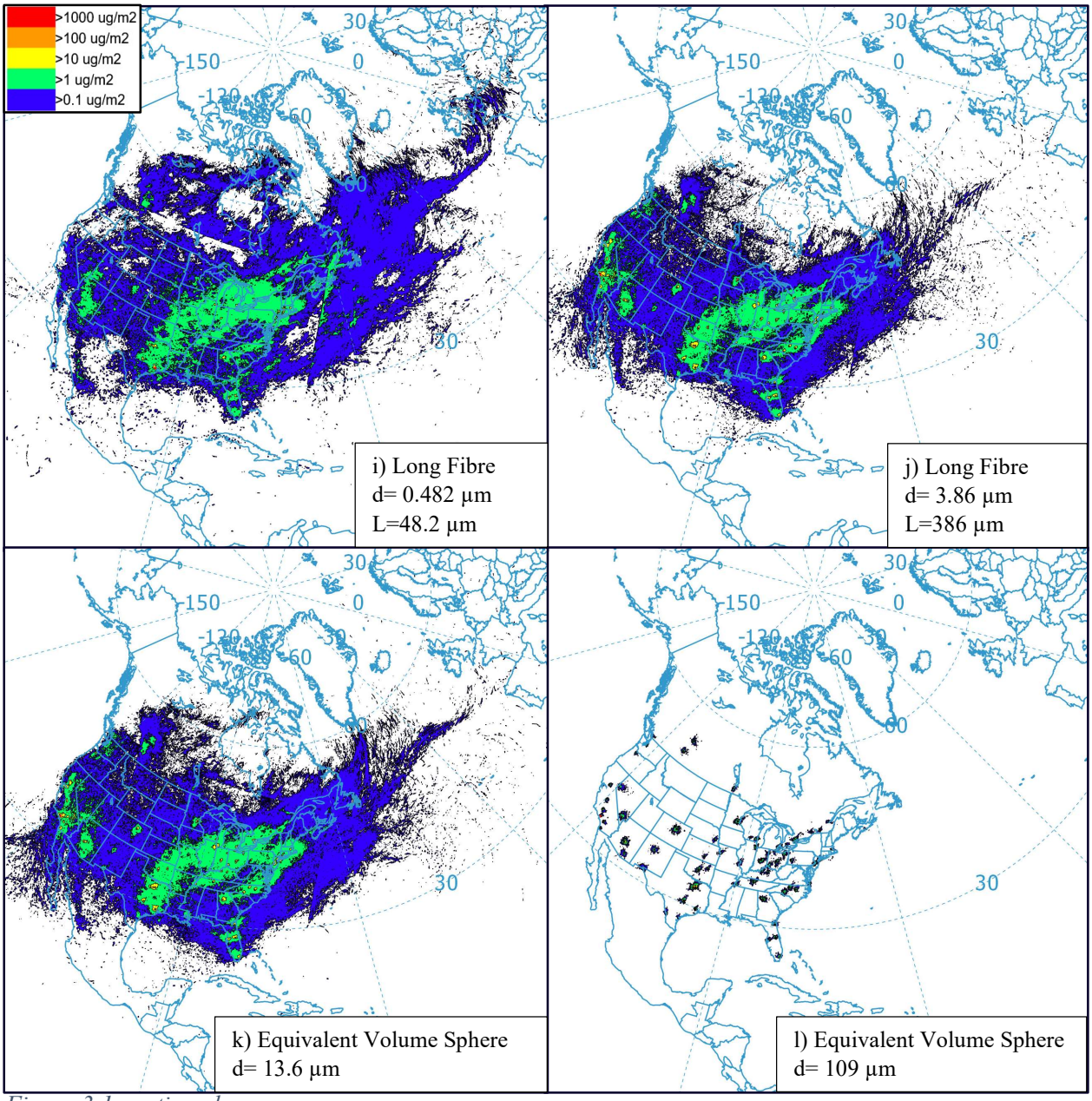

Figure 3.1 continued

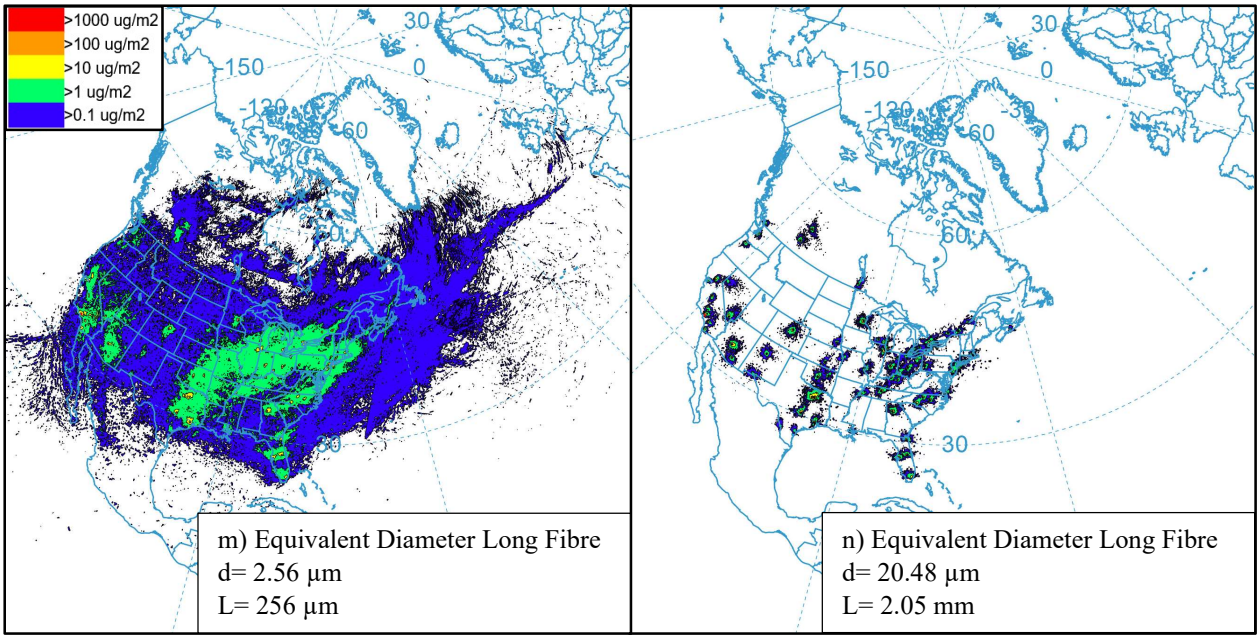

Figure 3.1 continued

The general trend for the deposition of TWP was similar for particles of the same size. Smaller particles were dispersed more widely than larger particles, as seen in the plots above. Particles of 2.56 µm size demonstrated similar deposition patterns regardless of shape, and this was also the case for some PM_{10}-sized particles when analyzed further in the discussions section. For larger particles above 10 µm size, the difference in sphericity had a much larger impact on the deposition area and amount of TWP. These changes can be seen in the 20.48 µm plots, as the longer cylinders increased the total range and area of microplastic transport. The range of microplastic transport depends mainly on the particle diameter and length, with smaller particles in the $PM_{2.5}$ range having significant deposition of greater than 0.1 µg m^{-2} into Northern Europe and remote Arctic regions such as the Canadian Territories and Greenland. The largest sizes modelled had significantly less range and much higher deposition of particles near the source areas and across North America. Amounts greater than 0.1 µg m^{-2} were found in remote regions, however, at the larger sizes, the coverage was significantly reduced compared to the smallest particles. The highest amounts in all plots were found closest to the emission sources and increased with larger sizes. The final plots of the equivalent diameter long fibre and equivalent volume sphere clearly show the location of all sources, as the deposition area was minimal compared to all other plots. Comparing these four plots (Figure 3.1k to 3.1n) still demonstrates

the increased deposition area for the fibrous particles. At the largest size of 109 μm, the overall deposition area is reduced compared to smaller sizes, although the fibres still show deposition over a much larger area than equal-volume spheres. In the plots of particle sizes less than 23.5 μm, other areas of interest include the regions of highest continuous deposition, which in most plots spanned from Texas up through the central and Eastern United States and along the Windsor-Quebec corridor in Canada. The west coast also had areas of high deposition, primarily within California, Nevada, and Arizona. In the two regions mentioned, the deposition amounts were consistently above 1 $\mu g\ m^{-2}$ regardless of the size or shape of the particle modelled. These regions of higher deposition also lined up well with many of the emission source points, which were dispersed and deposited over a shorter timeframe. The lowest particle amounts, between 0.1 and 1 $\mu g\ m^{-2}$, covered a much more extensive area in all plots. Almost all of the continental U.S. had some amount of deposition recorded in the plots shown, with only a few areas along the Rocky Mountains having less than 0.1 $\mu g\ m^{-2}$ microplastic deposition.

3.1.1 Spherical Particles

The spherical particles modelled included two different size ranges. The first range used the same diameters as the size indicated in Table 2.2 from 1.68 to 23.53 μm. The spherical particles here can be considered a control and are used in comparing the results from the study by Evangeliou et al., 2020. The second range of spherical particles had diameters ranging from 8.99 to 125 μm. All particles in this range had the same volume as the equal diameter long fibres, allowing for a direct comparison of transport distance for larger particles. Figures 3.1a and 3.1l demonstrate the two outer particle diameters. The plot of the smallest equivalent volume spherical particles behaves remarkably like all other shapes and covers a similarly large area. The largest diameter is a distinct outlier from all other plots shown in Figures 3.1a to 3.1k, with deposition above 0.1 $\mu g\ m^{-2}$ confined to the immediate areas surrounding the emission points. In addition to the four plots showing spherical particle deposition, Figure 3.2 below shows the deposition for diameters of the two middle bin sizes of the equivalent volume spherical particle of 27.3 μm and 54.6 μm for added detail of transport distance as the particle diameter increases.

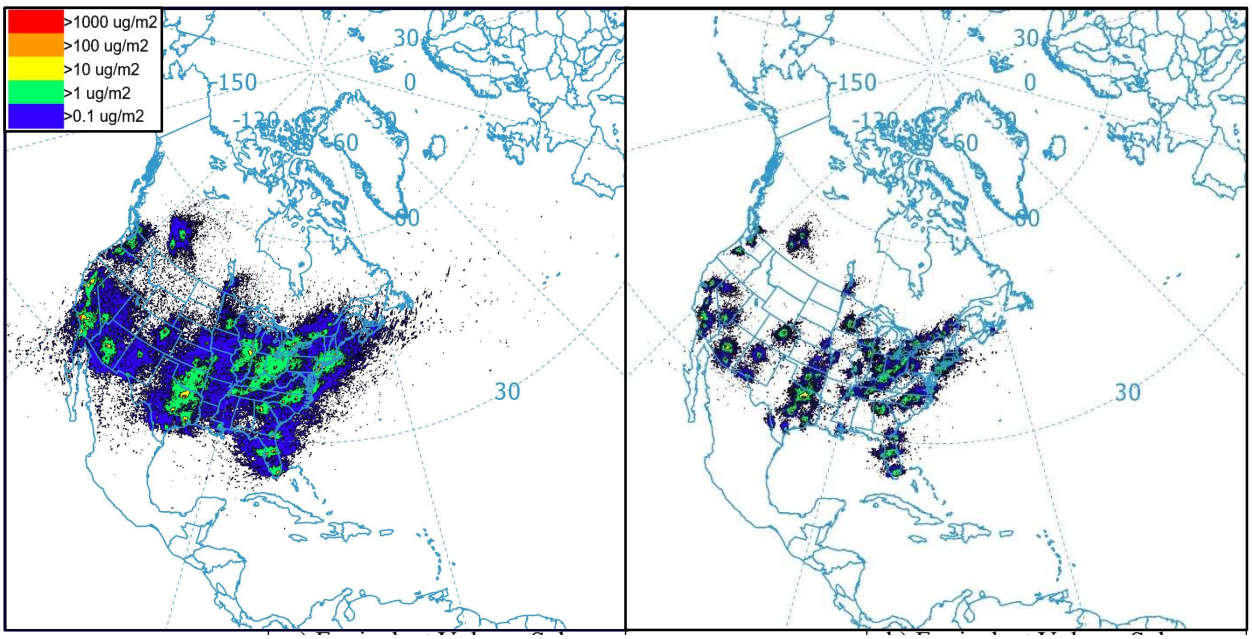

Figure 3.2: a) Deposition map from the long fibre equivalent volume spherical particles with a diameter of 27.3 µm. b) Deposition map from the long fibre equivalent volume spherical particles with a diameter of 54.6 µm.

These plots demonstrate the reduction in transport distance as the diameter of the spheres increases. At 27.3 µm, areas of continuous deposition ≥ 0.1 µg m^{-2} are confined to the land regions of North America and along shorelines in the Gulf of Mexico and the Atlantic Ocean. Areas of deposition above 10 µg m^{-2} can easily be noticed here, a feature not found in the plots from Figure 3.1. At large distances from the source points, visible deposition is scattered, especially in the Atlantic Ocean and towards Europe. Looking next at the 54.6 µm diameter spheres in Figure 3.2b, this plot begins to resemble the largest diameter particles in Figure 3.1l, where deposition areas are limited to the spaces surrounding the emission sources. The main difference between these plots is that the smaller diameter spheres show apparent movement with the wind patterns and have higher deposition values on emission sources' north and east sides. Once the diameter is larger than about 100 µm, as in Figure 3.1l, this characteristic is much less noticeable, as the deposition of particles occurs more quickly. The trend of decreasing deposition area also follows an increase in the maximum deposition output by HYSPLIT. Figure 3.3 shows the maximum local deposition amounts for spherical particles for each diameter modelled.

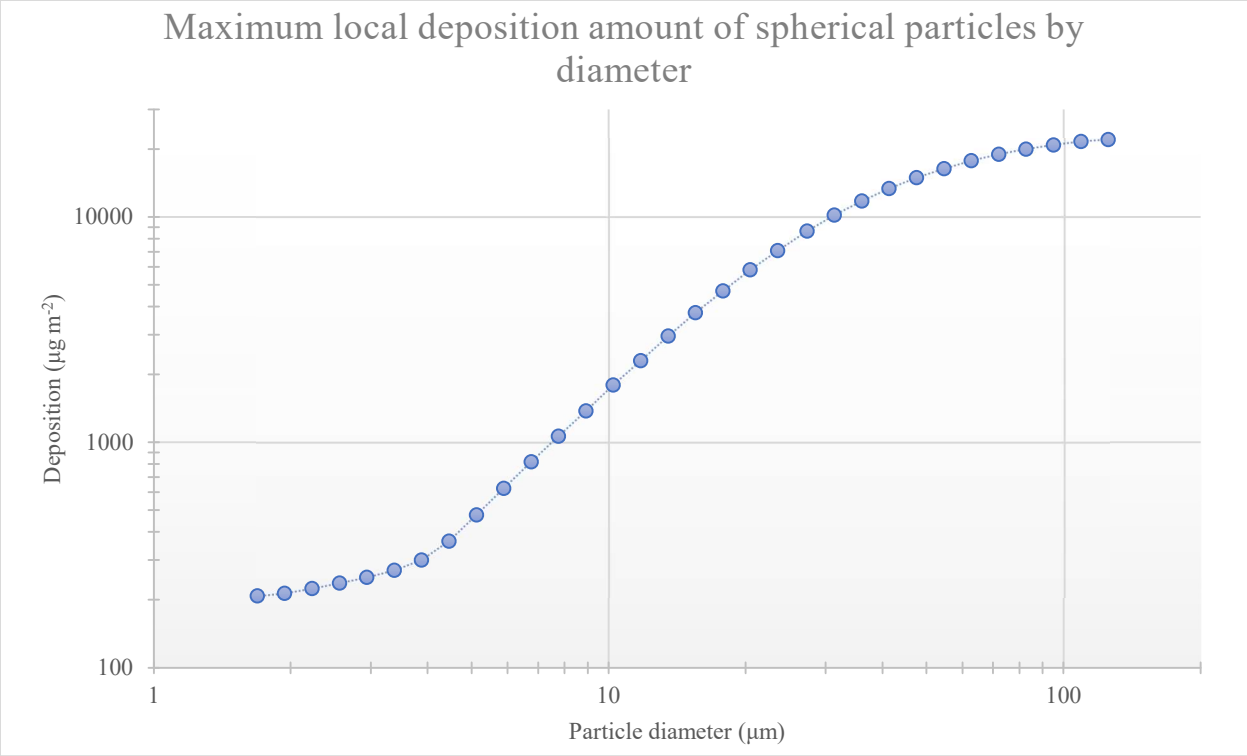

Figure 3.3: A log-log plot displaying the trend in the maximum deposition as the spherical particle diameter increases. The maximum concentration of particles was not in the same grid space for each diameter, instead, it shows the general trend as deposition occurs over a smaller area and at higher rates as the particles increase in size.

The difference in the maximum local deposition between the smallest particles of 1.68 µm and the largest at 125 µm was about 106 times greater, while the difference in particle diameter was only 74 times greater. This result indicates that the increase in maximum deposition is not linear and likely involves other factors besides particle size. The most considerable changes occurred as the particle diameter increased between 5 µm and 50 µm. Above 50 µm, the increase in local deposition was considerably reduced. The likely reasons for this can be seen by looking at the differences in the deposition area from Figures 3.11 and 3.2b. As the particle size increases beyond 50 µm, the transport of particles is already confined to areas near the source, so the maximum amount relies increasingly on the mass of emissions. The maximum deposition amount is beneficial as it provides an idea of the highest contribution of the atmospheric portion of microplastics and how that value changes depending on the size characteristics of the particles.

3.1.2 Fragments and Fibres

The fragments and fibres were modelled as cylindrical particles with the same range of sizes as the spheres from 1.68 to 23.53 μm. The diameters and lengths of the cylinders varied according to the aspect ratio or sphericity, as found in Table 2.2. Figure 3.1c to 3.1j shows the deposition of the four different fragments and fibres at 2.56 μm and 20.48 μm sizes. Plots of 2.56 μm particles show little change in the extent of the deposition area as the length of the particle changes. The main visible differences between these plots are the locations of the small deposition areas away from the larger continuous areas and at the edges of the continuous areas. Figure 3.4 below shows an enhanced view of deposition over the Atlantic Ocean to provide a more detailed look at the extent of change between the shapes. All plots in Figure 3.4 show particles with a size of 2.56 μm.

At 2.56 μm, the plot difference is subtle even when focused on a smaller area. Comparing the short fragment to the long fibre still shows little noticeable difference, with the largest variations being outside the main deposition area along the line of 30° latitude. Along this line of latitude, the deposition varies spatially. Still, visual differences in the amount or total deposition area are challenging to attain, and further numerical analysis of the data are needed. Although the lengths of the particles range from 3.0 μm to 48 μm, the relatively small diameters may be a limiting factor for any substantial changes in the settling velocities between the four shapes. A larger particle size must be used to see a difference in the deposition plots and can be visualized from the plots of 20.48 μm particle size.

Short Fragment

Diameter: 1.93 µm

Length: 3.01 µm

Long Fragment

Diameter: 1.53 µm

Length: 4.78 µm

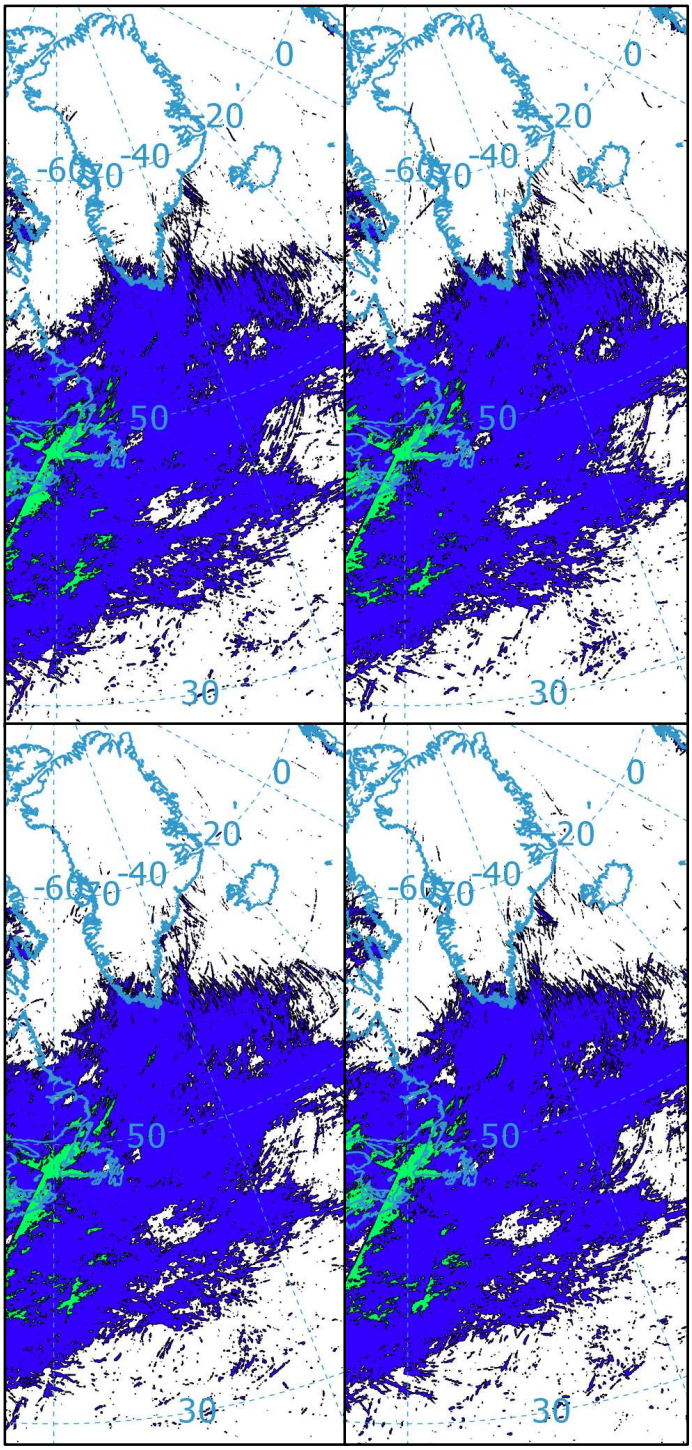

Short Fibre

Diameter: 1.04 µm

Length: 10.38 µm

Long Fibre

Diameter: 0.482 µm

Length: 48.2 µm

Figure 3.4: Deposition plots of the four cylindrical particle shapes focused on the northern Atlantic Ocean and Greenland. All particle sizes are of 2.56 µm. Overall, there is little noticeable variation in the plots despite considerable change in particle shape.

Short Fragment

Diameter: 15.4 µm

Length: 24.1 µm

Long Fragment

Diameter: 12.2 µm

Length: 38.2 µm

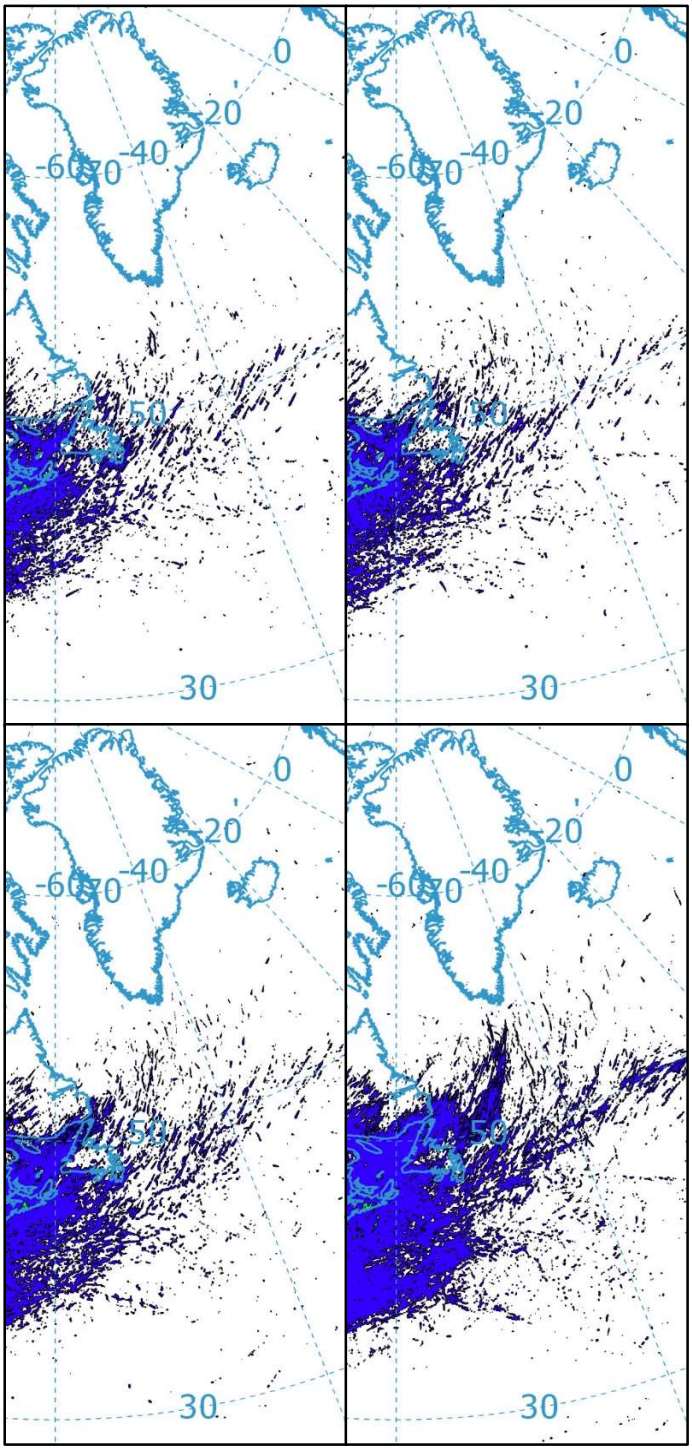

Short Fibre

Diameter: 8.30 µm

Length: 83.0 µm

Long Fibre

Diameter: 3.86 µm

Length: 386 µm

Figure 3.5: Deposition plots of the four cylindrical particle shapes focused on the northern Atlantic Ocean and Greenland. All particle sizes are of 20.48 µm.

At a larger particle size of 20.48 μm, there is a much more noticeable change in the deposition area as the length of the particles varies. The deposition area increases with each subsequent increase in the length of the particle when using the spherical particle plot as a reference. The difference between the two fragments in Figure 3.1d and 3.1f is relatively minor, with the 0.1 μg m^{-2} deposition area extending slightly further out in all directions for the long fragment compared to the short fragment. The most noticeable change is along the east coast, where the long fragment's deposition extends further into the Atlantic Ocean. The difference between the short and long fibres in Figures 3.1h and 3.1j is much more apparent. While the overall shape of the deposition area is larger for the long fibres, the region of the Atlantic Ocean south of Greenland is again a key focus area, as the deposition here is the largest for the long fibres. Figure 3.5 shows the differences in this area in greater detail between the four shapes. From the enhanced view, the short and long fragments show irregular deposition across Newfoundland, with increasing coverage of the Island for the short fibres and, ultimately, the majority coverage for the long fibres. Further east in the Atlantic Ocean, deposition greater than 0.1 μg m^{-2} extends north and south to a greater degree for longer particles than shorter ones. To the northern extent of the plots, the two fibrous shapes have more deposition recorded around Iceland and the Denmark Strait than the fragments. To the south, the two fibrous particles show more deposition, particularly around the line of 30° latitude. This pattern of increasing spread for longer particle lengths and greater volume follows for most regions. Nevertheless, with the prevailing westerly wind patterns present in the mid-latitudes, the pattern is most evident in areas east of emission sources.

The maximum local deposition amount was plotted for the four cylindrical shapes as was done for the spherical particles. Figure 3.6 below shows the maximum deposition amounts output by HYSPLIT for all shapes. Particles smaller than 5 μm have roughly the same maximum regardless of the shape or size. As the particle size increase, the variation in the maximum deposition increases at different rates depending on the shape modelled. The two fragments follow a very similar curve, with the largest difference being 174 μg m^{-2} greater deposition for the short fragment at the largest plotted size. The short and long fibres differ much more than the fragments. The largest difference between fibres was also at the largest size (23.53 μm), however, the short fibre had a maximum deposition amount of 1.21 mg m^{-2} larger than the long fibre. In terms of a percent difference, this resulted in a 2.6% difference for the fragments and a

25% difference for the fibres. When looking at all five shapes, the spherical particles had the highest maximum at all sizes. The difference in amounts between the spherical and short fragment particles at the largest size (23.53 µm) was 292 µg m^{-2} or 4.2%. The equivalent volume sphere and the long fibre had a maximum difference of 2.45 mg m^{-2} at particles of size 125 µm. For greater context in the comparison, the maximum deposition amount for the sphere was 12% larger than the long fibre, despite the particles having equivalent volume. The variations in the maximum between the modelled shapes show how the particles' shape and settling velocity impacts the total deposition over an area. More data analysis is needed to understand the effects on a broader scale across the model domain and will be discussed in the following chapter.

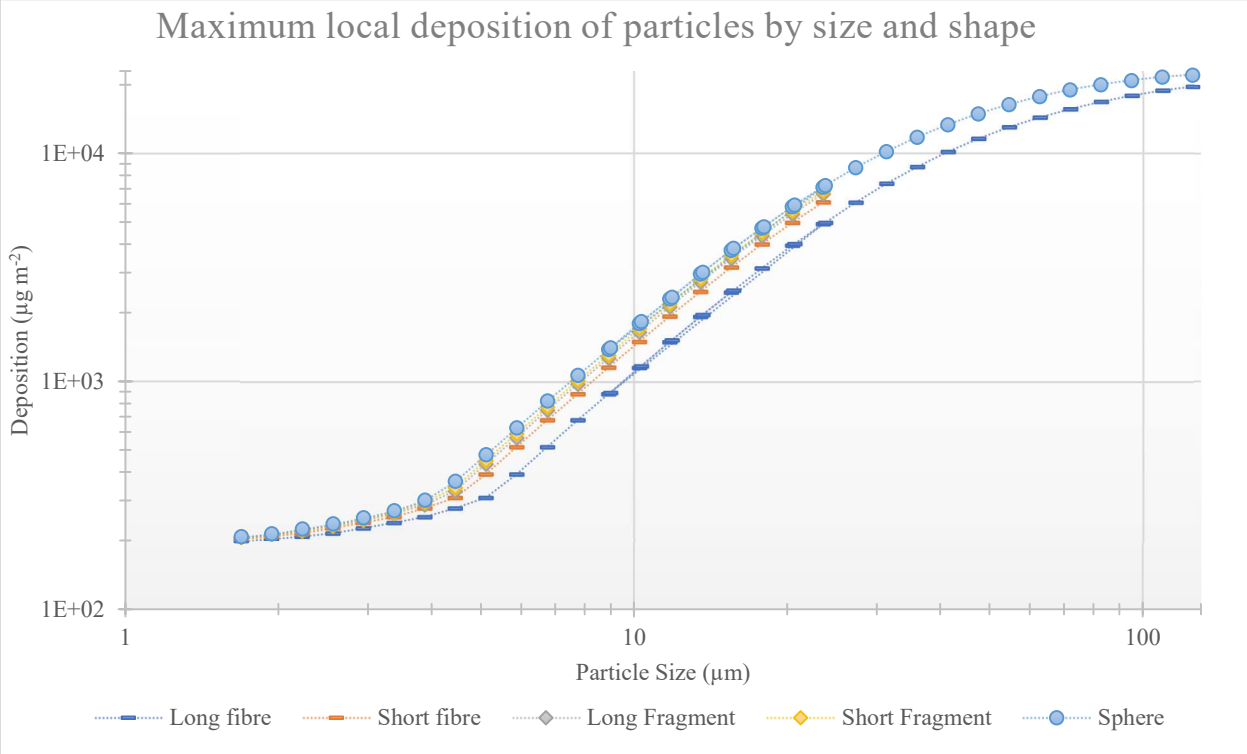

Figure 3.6: A log plot displaying the trend in the maximum deposition amount of all particle shapes. The maximum of particles was not in the same grid space for each shape, rather it shows the general trend as deposition occurs over smaller area and at higher rates as the particles increase in size.

3.2 Particle Distribution

The plots shown in the previous section provide a good idea of how the deposition of microplastics changes based on the shape of the particles modelled. Another tool for viewing the model results was plotting the distribution of airborne particles as a trend. Figure 3.7 below shows the five shapes plotted on trend lines and separated by latitude and longitude. The two sizes plotted were 2.56 μm and 20.48 μm to be consistent with the deposition plots. All plots in Figure 3.7 represent the distribution of airborne particles at the end of the emission time on July 22nd at 00Z. The total number of particles is constant on all graphs, at 113 298 and grouped into bins of one-degree separation. The latitude plots show the distribution between 10º to 90º north, and the longitude plots from 150º west to 30º east with the negative numbers representing longitudes west of the prime meridian.

There is a similar pattern in the airborne particle distribution as in the deposition plots in Figure 3.1 when reviewing the plots showing particles of 2.56 μm size. The number and location of particles at the highest value of the latitude plots across all shapes varied by 0.54º and 50 particles degree^{-1}, while the mean latitude was 36.06° N. At extreme latitudes, the equivalent volume spheres had higher concentrations than other particle shapes. The local peak around 80º was 52% larger for the equivalent volume spheres versus the long fragments, with all other shapes fitting between them. The longitude plot shows a similar distribution, with relatively little spread across the particle shapes. The peak longitude values varied by 2.12º and 171 particles degree^{-1}, with the largest difference between the spheres and short fragments. The average peak longitude was found at -97.76°. In all plots showing the distribution by longitude, there were multiple local maximums, most of which can be attributed to the location of the emissions sources, which fit between -123º and -63º. The two local maximums further east than 63° likely result from particle transport due to weather conditions that lead up to July 22nd. The differences in particle concentration by longitude show little variation when comparing the shapes of the smaller particles. At the furthest east locations plotted, there are roughly the same number of particles between the shapes, with the total number between 20º to 30º being 3007 for long fibres and 3080 for spheres, or a 2.4% difference. All other particles fit between these values like with the latitude plots.

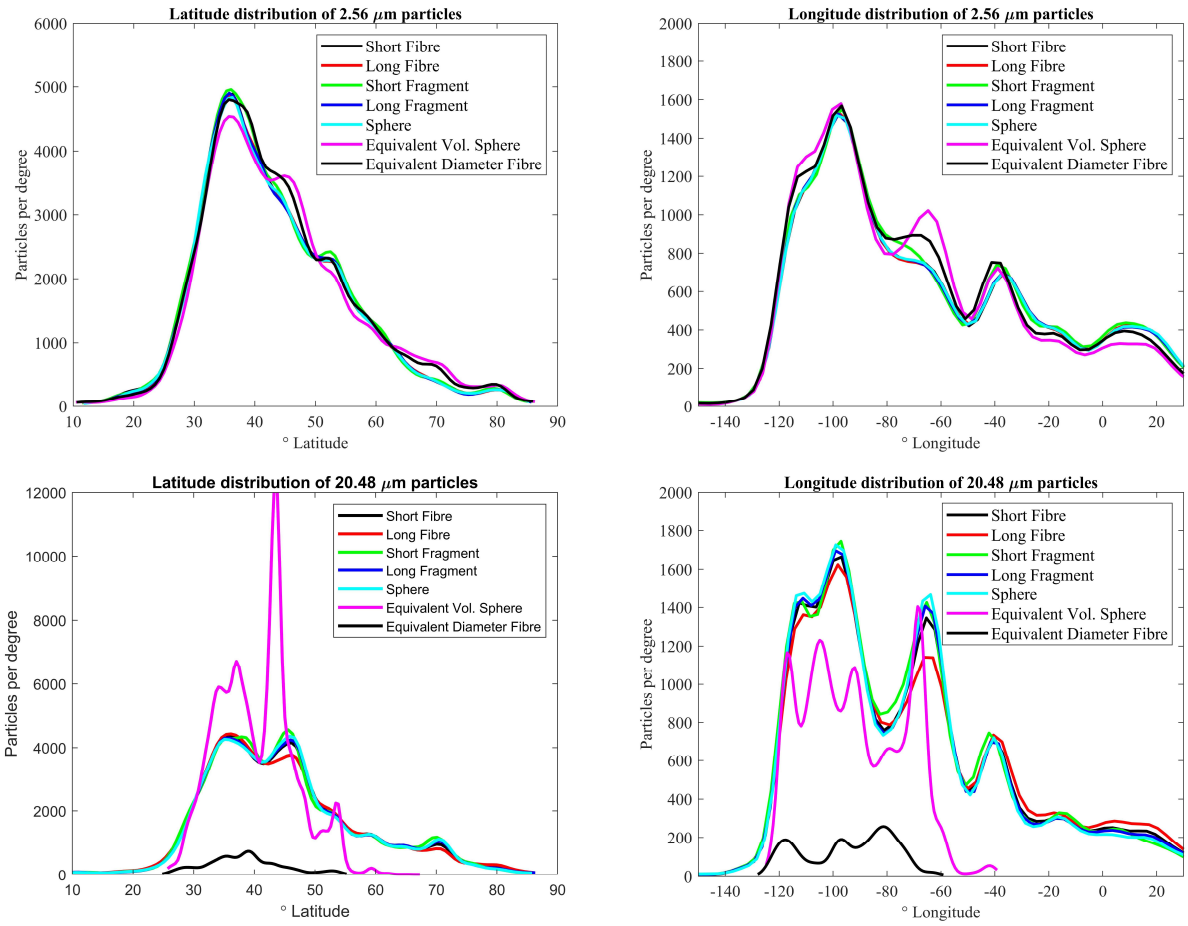

Figure 3.7: Distribution trend plots of particles of 2.56 µm and 20.48 µm size separated by shape. All graphs show the distribution of 113,298 particles on July 22nd, 2021, at 00Z. The plots on the left are of latitude and on the right longitude. Positive latitude indicates north, positive longitude indicates east, and negative longitude indicates west.

The plots displaying particles of 20.48 µm size vary more between the shapes and reflect the deposition plots in Figure 3.1. There are now two primary maximums instead of one in the latitude plots for larger sizes (excluding the equivalent volume sphere and equivalent diameter fibres). The average latitudes for the two peaks are 36.2º N and 45.9º N. The southern maximum varies across the five shapes by 2.8º latitude and 356 particles degree^{-1}. The northern maximum varies by 0.6º latitude and by 791 particles degree^{-1}. Looking at the locations of the emissions, the southern peak is near the weighted emissions average latitude, at 37.4° N. The northern peak is further north than all but four emission points, however, looking at Figure 3.1, there are substantial deposition amounts further north than the emission sources, pointing towards a general northeastern transport of particles. Above 50º N, there is a sharp decline in the airborne particle concentration across all shapes, as the increased settling velocity of the larger particles

reduces the transport distance. One feature not shown on the deposition plots is the maximum local airborne concentration of particles near 70º N. The maximum is most apparent for the spherical particles and smooths out as the particle length increases. The relatively large particle count at higher latitudes and an absence of deposition can suggest a longer atmospheric lifetime of these microplastic particles than was used in this modelling or that a lower deposition amount is needed when plotting to view the most extreme particle deposition.

The 20.48 µm longitude plots are more disorganized, with multiple local maximums and a wider spread of particles than the other plots shown. The maximum concentration average location is at -98.04° and varies the most between the long fragment and short fibre. The peak concentration varies by 220 particles degree^{-1} between short fragments and long fibres. To the east of the emission sources, the local maximums found are much larger than those for 2.56 µm sized particles. The two peak concentrations at longitudes of -65.2º and -41.0º show a significant difference by particle shape, although the difference does not appear to follow in order by particle length on these plots. Table 3.1 below summarizes the data shown in the plots in order of particle size and shape.

There are some distinct differences in the plots when comparing the effect of particle size. The 2.56 µm sized particles all show a single maximum concentration of particles around 36.1º N, while increasing the particle size to 20.48 µm creates two separate maximums at latitudes further north and south around 45.9º N and 36.4º N. The overall spread of particles is more apparent at the smaller sizes as the slope of particle concentration north of the peak is less steep compared to the larger sizes. Taking the mean latitude of particles across all shapes, the 2.56 µm plots are further south at 43.4º versus the 20.48 µm plots at 44.9º. The weighted average latitude of emissions at 37.4º more closely aligns with the smaller particles.

The changes in the longitude plots between particle sizes are even greater than those of latitude. Moving west to east on the plots, the maximum values and location are relatively consistent for both sizes. The primary difference between the sizes is at longitudes further east than -80º. All plots have one or two local maximums east of -80º, however, the average value of the maximums is much larger at 20.48 µm. At the extreme eastern edge of the domain, the average concentration of the smaller particles is significantly larger than the large particles. Table 3.1 also shows the standard deviation of the mean distribution of particles by

*Table 3.1: Further detail from Figure 3.7 of the particle distribution by latitude and longitude. Data includes the peak concentration of particles and location and the mean location with standard deviation. * Plots of EQ d. L. fibre of 20.48 µm had reduced particle count due to HYSPLIT output error*

	Latitude	**Longitude**	**Latitude**	**Longitude**
Size (µm)	2.56		20.48	
	Max particles per degree			
Sphere	5062	1922	4852	1996
S. fragment	5049	2089	5278	2167
L. fragment	5062	1943	4591	1984
S. fibre	5012	1927	4559	1968
L. fibre	5017	1918	4532	1947
EQ vol. sphere	4665	1877	16900	11420
EQ d. L. fibre	4913	2092	582*	946*
	Location of maximum particles (°)			
Sphere	36.28	-98.73	45.83	-99.00
S. fragment	36.07	-96.61	45.55	-97.06
L. fragment	35.78	-98.04	45.95	-99.09
S. fibre	36.32	-98.07	36.12	-96.83
L. fibre	35.83	-98.05	36.15	-98.23
EQ vol. sphere	35.71	-97.06	43.35	-68.60
EQ d. L. fibre	35.70	-96.82	38.94	-81.34
	Mean overall location (standard deviation) (°)			
Sphere	43.37 (12.4)	-56.33 (54.9)	44.96 (12.4)	-70.28 (43.0)
S. fragment	43.26 (12.1)	-56.94 (54.4)	44.88 (12.5)	-69.93 (43.2)
L. fragment	43.36 (12.1)	-56.37 (54.9)	45.02 (12.5)	-69.35 (43.9)
S. fibre	43.36 (12.2)	-56.34 (54.8)	45.00 (12.5)	-68.06 (45.1)
L. fibre	43.42 (12.1)	-56.17 (55.0)	44.79 (12.7)	-65.52 (47.6)
EQ vol. sphere	44.53 (12.7)	-63.05 (49.5)	40.39 (6.40)	-92.03 (18.3)
EQ d. L fibre	44.02(12.5)	-60.55(51.6)	38.24(6.09)	-94.32(16.2)

shape and size. The spread in latitude is generally unchanged using the standard deviation in all shapes and sizes except for the equivalent volume spheres, which show a considerably reduced deviation at 20.48 µm. The standard deviation in longitude increases with particle shape if the size is kept constant, however, it is greatly reduced for larger particles when comparing the 2.56 µm particles to the 20.48 µm. The values found in Table 3.1 highlight how the shape and size of particles contribute to the spatial distribution and subsequent deposition of airborne microplastics.

Finally, the larger equivalent volume spheres and the long fibres are compared. The plots of the equivalent volume spheres show the same diameters used in the deposition plots at 13.6 μm and 109 μm. Looking at the 2.56 μm diameter long fibre and the equivalent sphere (with a volume of 1317 μm^3), the differences in the distributions are noticeable, however, they still maintain similar features. From Table 3.1, the maximum concentrations vary by 248 particles $degree^{-1}$ and 0.01º by latitude, while the maximum longitude varies by 215 particles $degree^{-1}$ and 0.24º. At locations east of 0º longitude, the fibres have a higher average concentration than the spherical particles. The major difference in the distributions occurs at the larger diameters. The equivalent volume spheres of 20.48 μm diameter fibres are confined to latitudes from 25º to 73º N and have an extreme maximum of 16900 particles $degree^{-1}$ at 43º N. The distribution by longitude shows a similar idea, with all particles confined between -125° and -39º with a peak of 11420 particles $degree^{-1}$ at -68º. The long fibres of equivalent diameter are also averaged further east from the source locations compared to the spheres. Exact comparisons between the particle shapes at larger sizes are limited by an error in extracting particle location data. The differences between the particle distributions, despite having the same volume and mass, demonstrate the impact particle shape has on the overall transport of microplastics and will be further discussed in the following chapter.

4 -Discussions

This thesis evaluates how the transport of microplastic particles changes based on the shape of the particles. From the previous chapter, the modelling results demonstrated considerable changes in the deposition area, total deposition amount, and overall particle distribution for some sizes and shapes but less so for others. Statistical analysis and discussion of the numerical results will provide more details of the differences in the transport by shape and allow for more discussion of future work. The data analysis methods include comparisons to previous work, tables and figures to demonstrate the key differences of deposition by size and shape, discussions on the limitations and other restricting factors on the data presented, and a review of the critical dynamic processes involved in atmospheric transport of microplastics.

4.1 Study Comparison

Before further data analysis, other studies' results were gathered to determine how this work compares to other published research. The comparisons included results from other model work and in-situ collection of microplastics like those found in Table 1.1. Comparing the results from this thesis to previous studies helps to understand the results' validity and to provide further evidence suggesting the atmosphere is a major contributor to global microplastic transport.

4.1.1 Model Comparison

Here the simulated transport and deposition of TWP were compared to Evangeliou et al., 2020. Figure 4.1 is reproduced using the FLEXPART model results from Evangeliou et al., 2020 as a visual comparison to the deposition plots for the work in this thesis using particle sizes within the $PM_{2.5}$ and PM_{10} range. Two new deposition plots were created from the HYSPLIT results with nearly equivalent particle sizes and are shown below in Figure 4.2. All compared results are from spherical particles, as Evangeliou et al., 2020 did not include other shapes in their modelling.

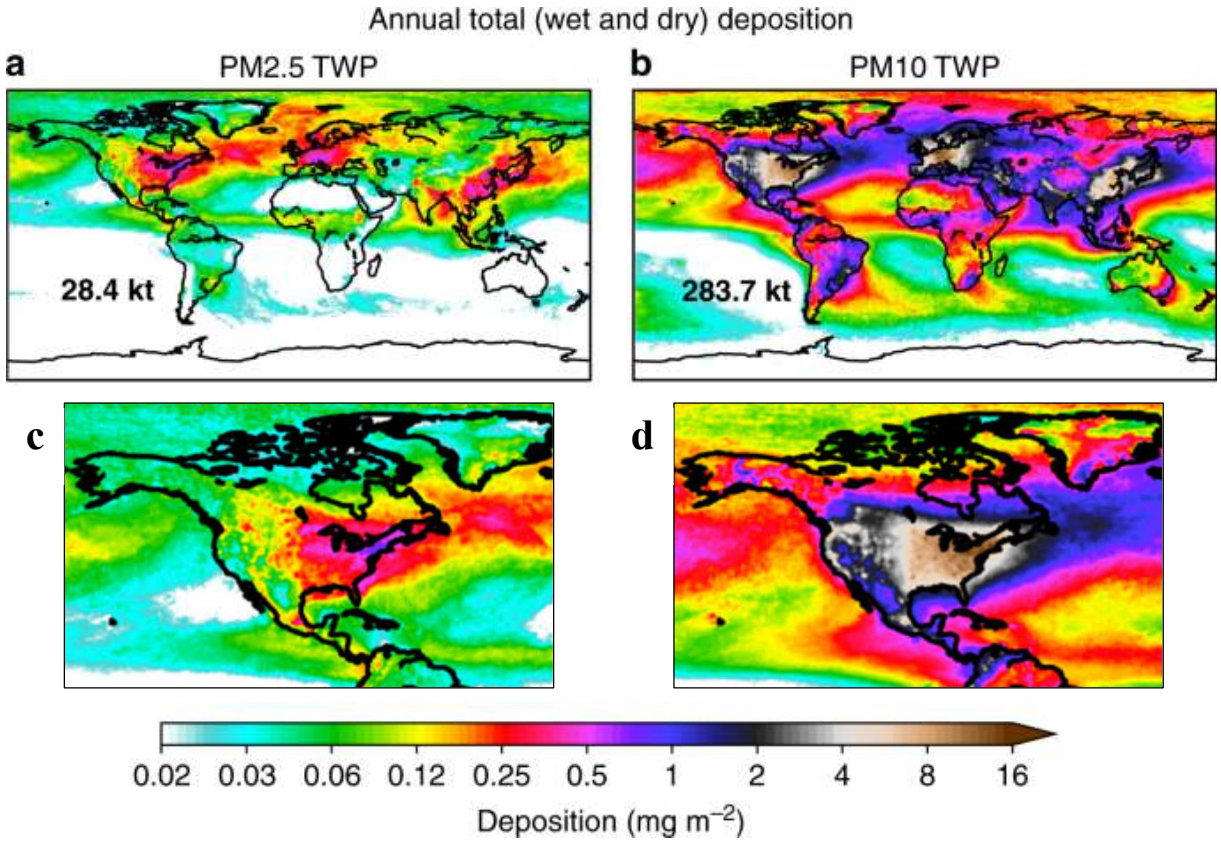

Figure 4.1: The annual total depositions of TWP as found in Figure 2 in Evangeliou et al., 2020. The total mass and comparative concentrations are significantly higher than the HYSPLIT results, as emissions were set globally and occurred over a full year. The largest deposition in North America were found along the East coast in both the $PM_{2.5}$ and PM_{10} plots. Plots (c) and (d) are identical to (a) and (b), focused in on the relevant location over North America to give more visual detail for comparison to the relevant domain in HYSPLIT.

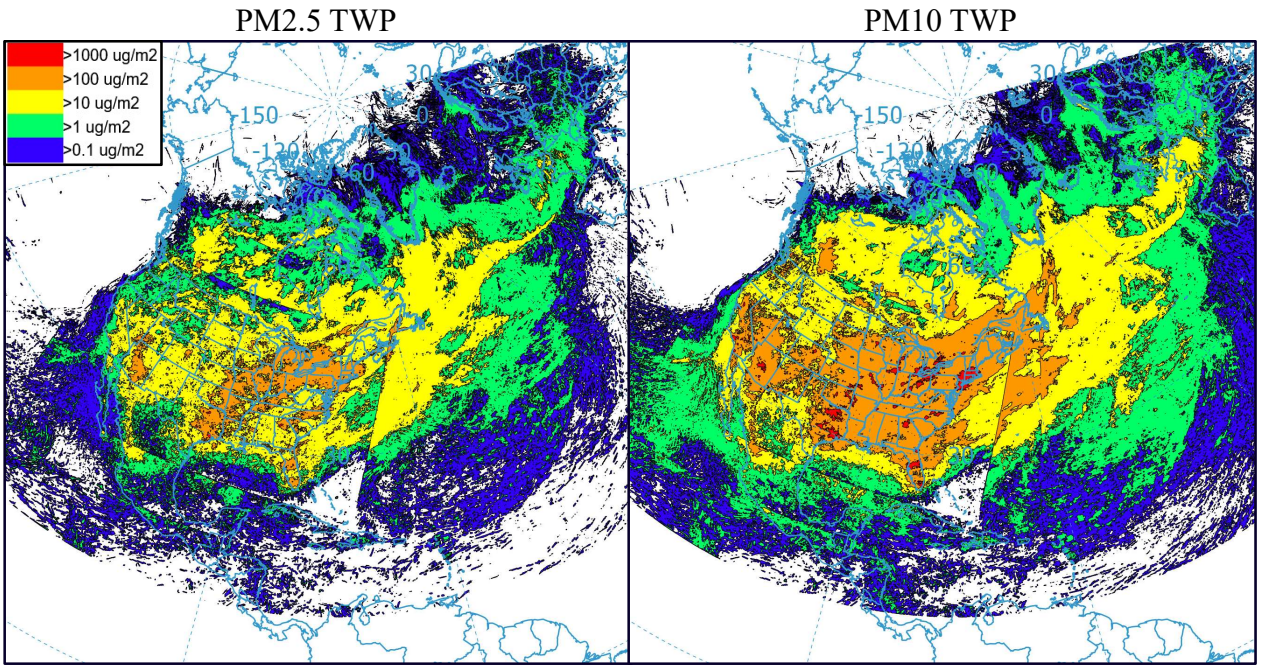

Figure 4.2: Total yearly deposition of TWP modelled by HYSPLIT in $PM_{2.5}$ and PM_{10} size range. Deposition is much more widespread than in previous HYSPLIT plots due to the increase in the total mass of particles and the multiple particle sizes shown. Both plots show the deposition for the spherical particles and where $PM_{2.5}$ ranges from 1.68 - 2.56 µm and PM_{10} ranges from 1.68 – 10.24 µm diameter.

These plots display the total deposition amount for particles in the $PM_{2.5}$ and PM_{10} size ranges, being 1.68 to 2.56 µm and 1.68 to 10.24 µm, respectively. In Figure 4.2, the plotted deposition is extrapolated from the original time of 21 days of emission up to a full year to match the model time from Evangeliou et al., 2020 This was done by applying a deposition multiplier of 17.38 (365/21) to the HYSPLIT model output. Looking at the $PM_{2.5}$ plots from Figures 4.1 and 4.2, the general trend of increased deposition amounts follows in both results from Evangeliou et al., 2020 and this study. The highest deposition within the continental region extends through roughly the same areas along the east coast of North America. As Evangeliou et al., 2020 modelled deposition through an entire year and used VKT and CO_2 emissions as a proxy for TWP emission, the amounts and total area are much larger than those from this study when looking at a direct comparison. The PM_{10} plots show a similar result, with the highest amounts in the same geographical area on both plots and an overall increase in the total relative deposition compared to the $PM_{2.5}$ plots. Over the Atlantic Ocean, the highest amounts were found along similar latitudes in both studies, ranging from 40 °N to 60 °N. Although the general trends in the deposition location between the studies follow when looking at the plots, specific deposition values taken at locations allowed for a direct numerical comparison. Table 4.1 shows

the deposition from both models at three locations: Toronto, a point within The Atlantic Ocean, and Iqaluit. Toronto was chosen as the urban site, as emission sources were present in both models' sample locations. The points within the Atlantic Ocean and Iqaluit were chosen to represent the deposition from long-range atmospheric transport over water and an area that is remote from the nearest emission sources.

Table 4.1: Deposition values gathered for three locations from Evangeliou et al., 2020 and HYSPLIT in units of μg m^{-2} yr^{-1}. Locations were chosen to examine changes in deposition between large urban areas and remote water and land areas. Data from this study are extrapolated from the July results to estimate the yearly deposition.

		Evangeliou et al., 2020		*This study*		*The ratio of deposition (Evangeliou. et al./ this study)*	
City	Coordinates	2.1 μm	9.5 μm	2.29 μm	8.9 μm	ratio	ratio
Toronto	43.75°N, 79.75°W	**457**	**1324**	**186**	**211**	**2.45**	**6.27**
Ocean	50°N, 40°W	**243**	**71.1**	**3.23**	**7.98**	**75.2**	**8.91**
Iqaluit	63.75°N, 68.5°W	**58.4**	**11.7**	**1.79**	**0.834**	**32.6**	**14.0**

Data from Evangeliou et al., 2020 were taken for particles of 2.1 μm and 9.5 μm diameter, and data from this study were taken for particle sizes of 2.29 μm and 8.9 μm diameters. Only the spherical particles were used from this work in the comparison to keep the shape consistent. Deposition values were extracted using a bilinear interpolation method which averaged the deposition in grids adjacent to the three coordinates. Before any modifications were made to the data, the deposition values between the models varied significantly. For Toronto, at 2.1 and 2.29 μm diameter, the results from this study predicted an annual deposition of 186 μg m^{-2}, while Evangeliou et al., 2020 had a 2.45 times higher level at 457 μg m^{-2}. At 8.9 and 9.5 μm diameter, the annual depositions were 211 μg m^{-2} and 1324 μg $m^{-2,}$ respectively or 6.27 times higher in Evangeliou et al., 2020. The differences at the two remote locations were substantially larger than those in Toronto, with the smallest difference being 8.9 times higher deposition and the most significant difference being 75.2 times higher deposition in the study by Evangeliou et al., 2020 compared to this thesis.

As discussed previously, there were many differences in how the studies were conducted, resulting in large differences between the values presented. Isolating for each difference would be extremely difficult, so several variables were calculated. The factors assessed quantitatively are the emission rates and locations, model run time, and the ratio of TWP emitted. The emission rates in HYSPLIT were kept at a constant value as calculated from the VKT, which was 40.5 kg hr^{-1} for each of the twenty particle diameters. The hourly emissions in the $PM_{2.5}$ and PM_{10} range were 162 and 567 kg hr^{-1}, respectively. With 21 days of emissions, the total mass of particles modelled was 0.082 kT and 0.286 kT in $PM_{2.5}$ and PM_{10}. For continuous emission over an entire year, the particle mass would increase to 1.42 kT and 4.97 kT for $PM_{2.5}$ and PM_{10}, respectively. By comparison, the total yearly emissions modelled by Evangeliou et al., 2020 within North America ranged from 2.6 to 16 kT for $PM_{2.5}$ and 46 to 90 kT for PM_{10}. The emission amounts differed from the methods applied in each study. Evangeliou et al., 2020 had higher total emissions due to using a continuous emission domain across North America rather than using points of select major cities, as was done here. Additionally, Evangeliou et al., 2020 utilized a constant TWP/CO_2 emission ratio for the transport sector to determine the total TWP emissions alongside VKT data. In this thesis, TWP emissions were solely estimated using VKT data and a ratio of TWP released per VKT total, as outlined in section 2.1.3. The deposited mass of particles was more challenging to identify and isolate from North American emissions, as Evangeliou et al., 2020 modelled global emissions. The total North American deposition was estimated using a ratio of the total emissions throughout the model run to the total deposition mass at the end of the run time, which was 0.966 and 0.986 for $PM_{2.5}$ and $PM_{10,}$ respectively, in the study by Evangeliou et al., 2020. In this thesis, the shorter model time and differences in meteorological data gave emission-to-deposition mass ratios of 0.810 and 0.853 for the same size ranges. Changes in the mass emitted in each particle size range further added to the differences between studies. The mass distribution of TWP emitted by particle diameter from the ensemble results ranged from 5 to 30% ($PM_{2.5}$) and 10 to 40% (PM_{10}) in Evangeliou et al., 2020, while in HYSPLIT, a constant mass fraction of 5% mass by diameter was applied. Using the ratios found from the differences in deposition to emission and the total emission range, Table 4.2 presents the data discussed to get a final emission difference ratio under this study following

$$\frac{E_{ev}}{E_T}\frac{M_{ev}}{M_T}\frac{r_{ev}}{r_T} = P \tag{4.1}$$

where E represents the yearly North American emissions (with $*_{ev}$ being Evangeliou et al., 2020 and $*_T$ being this thesis), M is the mass distribution by particle size, and r is the ratio of mass emitted to mass deposited for each study as indicated by the corresponding subscript. Table 4.3 then presents the estimated deposition ranges using P in Equation 4.1 to find

$$\frac{dC}{dt}_1 = P\frac{dC}{dt}_0 \tag{4.2}$$

where $\frac{dC}{dt}$ is the total yearly deposition mass.

The estimated range of deposition fits with some particle sizes and areas, however, there are still values outside the calculated range. In Toronto, deposition of the smaller particles in the $PM_{2.5}$ range correlates between studies, but the larger particles in the PM_{10} range show a higher amount in this study compared to the modified values from Evangeliou et al., 2020. The only values that did not align in the two remote locations were the PM_{10}-sized particles. While this comparison shows that most deposition amounts can align between the studies, many other variables were involved, preventing a proper comparison. The most significant variables included the different models used and the parameterizations of the models, the meteorological conditions, grid sizing, model run time, and the particle mass, size, and distribution of source locations. In this study, there is a greater potential for overestimation of deposition near source points and underestimation at large distances compared to Evangeliou et al., 2020. Comparing the results in this thesis to other modelling work provides an idea of how well the output of the HYSPLIT model fits with previous research and what to expect from further data analysis.

*Table 4.2: A list showing the major differences in emissions between Evangeliou et al., 2020 and this study. Data from Evangeliou et al., 2020 were separated into individual particle sizes. Values with * represent the specific particle diameter, while all others fit in the particulate matter categories. The final row shows the two studies' minimum and maximum ratios between emissions.*

	Evangeliou et al., 2020		*This study*	
Diameter(μm)	PM2.5/ 2.1*	PM10/ 9.5*	PM2.5/ 2.29*	PM10/ 8.9*
***(E)** North America Emission (kT/yr)*	2.6-16	46-90	1.42	4.97
***(r)** The ratio of mass emit:deposit*	0.966	0.986	0.810	0.853
***(dC/dt$_0$)** North America deposition (kT/yr)*	2.51-15.45	44.41-86.90	1.15	4.24
***(M)** Mass size distribution**	5-30%	10-40%	5%	5%
***(P)** Emission difference ratio*	**0.012-0.46**	**0.0059-0.047**	**2.18-80.6**	**21.4-167**

Table 4.3: The emissions difference ratio from Table 4.2 applied to the results from Evangeliou et al., 2020 in Table 4.1. Green text indicates that the range fits within the values found in the results from this thesis.

Location	*Coordinates*		*Evangeliou et al., 2020*		*This study*	
		Particle Diameter(μm)	2.1	9.5	2.29	8.9
Toronto	43.75N, 79.75W	*Dep(μg/m^2/yr)*	**5.5-210**	**7.8-62**	**186**	**211**
		Dist. from nearest source (km)	0	0	0	0
Atlantic Ocean	50.0N, 40.0W	*Dep(μg/m^2/yr)*	**2.9-110**	**0.42-3.3**	**3.23**	**7.98**
		Dist. from nearest source (km)	1000	1000	2300	2300
Iqaluit	63.75N, 68.5W	*Dep(μg/m^2/yr)*	**0.70-27**	**0.069-0.55**	**1.79**	**0.834**
		Dist. from nearest source (km)	1100	1100	1900	1900

4.1.2 In-situ Study Comparison

Comparing the HYSPLIT model output with results from in-situ studies allowed further evaluations of the transport areas and deposition. The primary limitation of the results from the in-situ collection of microplastics was the lack of data on particles smaller than 11 µm. There were no reliable counting methods for the smallest particles, and the units used to report the deposition were in number rather than mass density. Deposition amounts from this study were found for thirteen in-situ collection sites (9 distinct sample sites from Bergmann et al., 2019, 1 from Allen et al., 2019, and 3 from Granados-Galván et al., 2022) and accounted for all particle sizes separated by the five shapes listed. The results from the in-situ studies were reported mainly in units of # L^{-1}, representing the number of microplastic particles per litre of meltwater, L. The meltwater in the studies is from the snowpack sampling collected. The amount of snow taken per sample varied, although it generally consisted of a small volume of snow. Supplementary data from Bergmann et al., 2019 included the area and depth of some samples, with a depth of 5 cm and an area of 2500 cm^2 (50 cm × 50 cm) being the largest recorded. Converting the data output by HYSPLIT into a number amount involved taking the mass per particle from the smallest to the largest sizes and multiplying by the mass amount reported. In

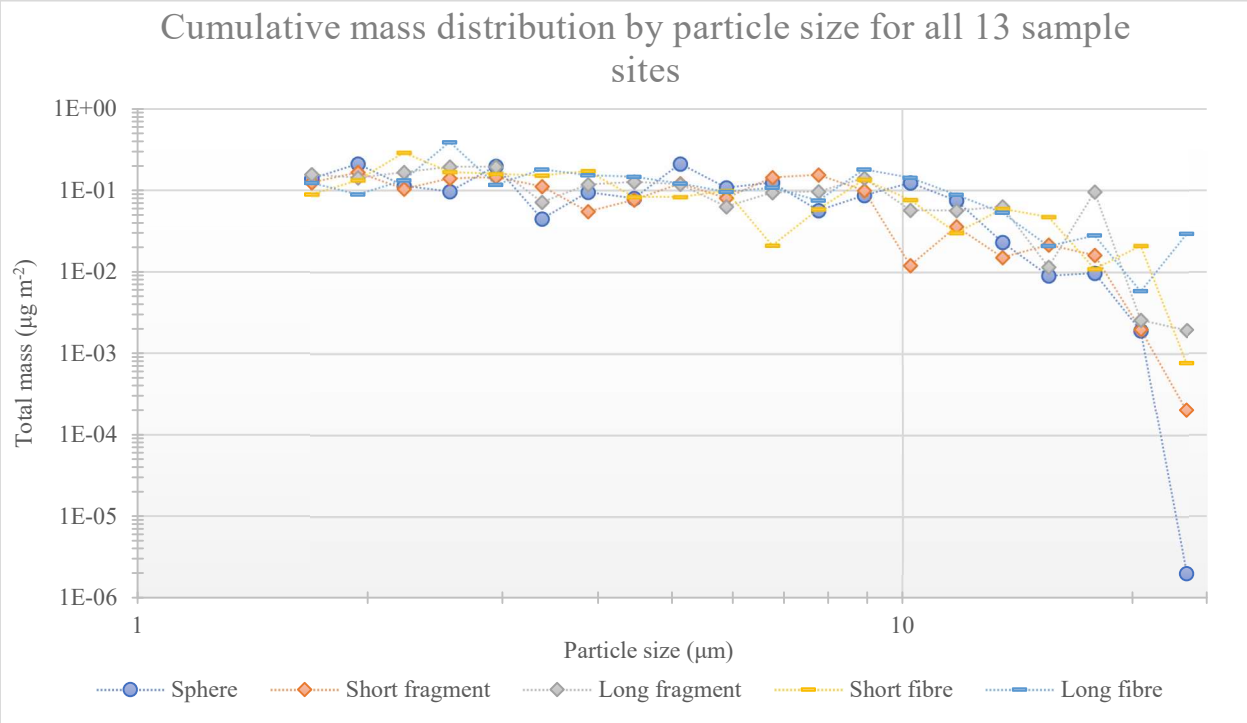

Figure 4.3: Cumulative mass of particles deposited across the 13 in-situ sites separated by particle shape and size. Each site took data from one grid space retrieved from the HYSPLIT results.

the remote locations, most of the deposited mass resulted from the low and mid-sized particles, as the deposition from this study peaked at 11.76 µm when accounting for all shapes and sizes of particles modelled. Figure 4.3 shows the total mass distribution for the five shapes summed across the thirteen in-situ study locations.

Figure 4.4: Map containing all point locations of the sample sites for microplastic collection. The three North American sites were collected and analyzed by Granados-Galván et al., 2022 The Pyrenees Mountain site was maintained by Allen et al., 2019 and was a static station for collection of direct deposition of microplastics. The two European Arctic points contained 9 sample sites analyzed by Bergmann et al., 2019

The general trend across the thirteen remote sites was a decreased relative deposition as particle size increased. The total mass by shape was comparable at smaller particle sizes and began to noticeably diverge as the particles increased in size above 10 μm. At the largest size of 23.53 μm, the difference between shapes is apparent with the spherical particle deposition 1.48×10^{3} times less than the long fibre. For almost all other particle sizes, no distinctive pattern exists between the five shapes, possibly due to the small sample size of thirteen remote grid points. While these data provide detail on the sizes of microplastics found in numerous remote Arctic regions, comparison to other work is focused only on the total deposition as particles less than 25 μm in size have yet to be extensively studied. The location of all in-situ studies is shown in Figure 4.4, with each location colour coded based on the study. For the study by Bergmann et al., 2019, two single-centred points were placed to represent the nine samples taken from the ice floes and the five samples from Svalbard, as described in Chapter 1.

Since emissions in this study were only located in North America, the deposition found from the in-situ studies within Europe was expectedly larger than those shown in this thesis, however, there was deposition reported across all locations, suggesting the extent of atmospheric transport of microplastics. The early results from Granados-Galván et al., 2022 in the Canadian Arctic remain the focus for comparison to this thesis, as microplastics were discovered at all sample sites with varying amounts. All data from this thesis and the in-situ studies are plotted in Figure 4.5 and Figure 4.6 below.

The number of microplastics reported from in-situ studies varied considerably between locations. Bergmann et al., 2019 found microplastics in the Arctic regions of Europe at almost all locations except on the second ice floe, where none were recorded. At all other sample sites, the number amount ranged from 122 to 14400 microplastics per litre of meltwater (# L^{-1}). Although the result from ice floe 9 was significantly larger than all others, Bergmann et al., 2019 stated the results were probably not due to contamination as the polymer found was unlike any used in collecting the sample. Results in this thesis found values in these locations ranging from 8.58×10^{-7} μg m^{-2} to 4.03×10^{-2} μg m^{-2}. In the Pyrenees Mountains, Allen et al., 2019 found an average microplastic deposition of 365 particles per metre squared per day (# m^{-2} d^{-1}), with the study occurring from November 2017 to March 2018. Here, deposition amounts in this thesis were less varied, ranging from 0.0496 μg m^{-2} to 0.169 μg m^{-2}. In the Canadian Arctic,

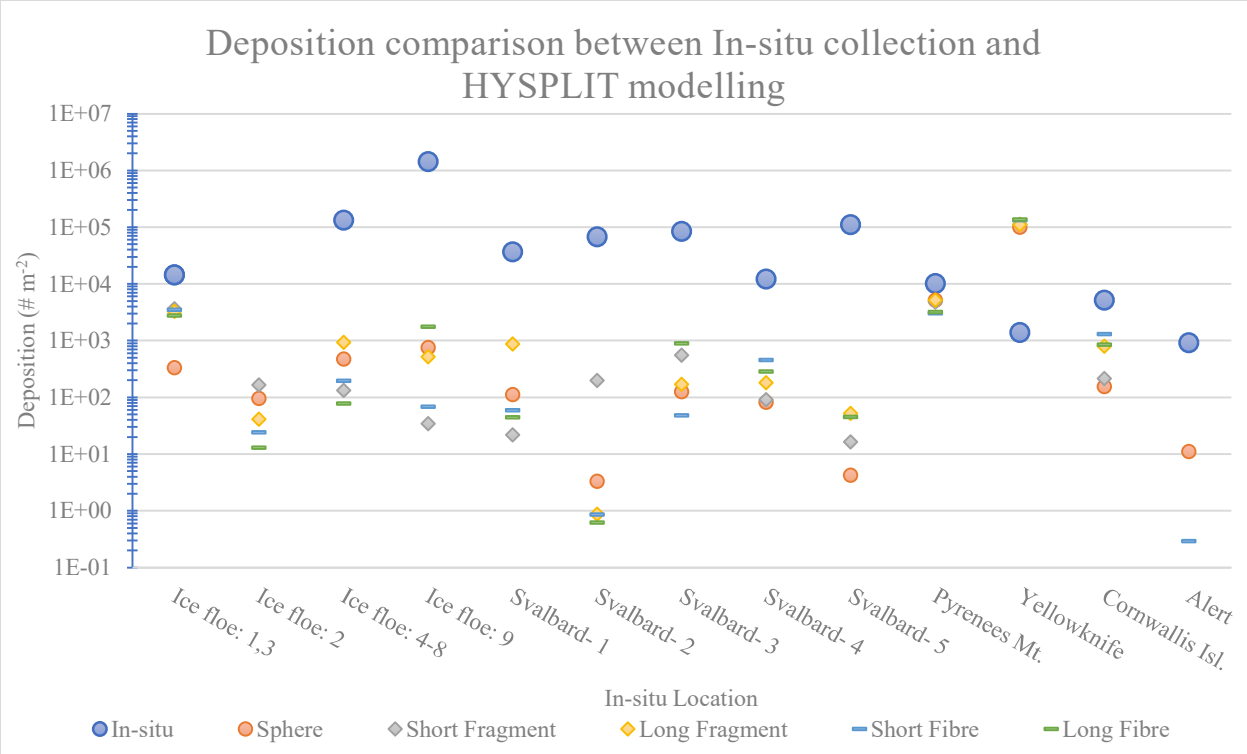

Figure 4.5: Comparison of the deposition of microplastics found from in-situ sampling across thirteen different locations. HYSPLIT deposition is separated by particle shape, while the in-situ results include all analyzed particles in units of number of particles per area (# m^{-2}).

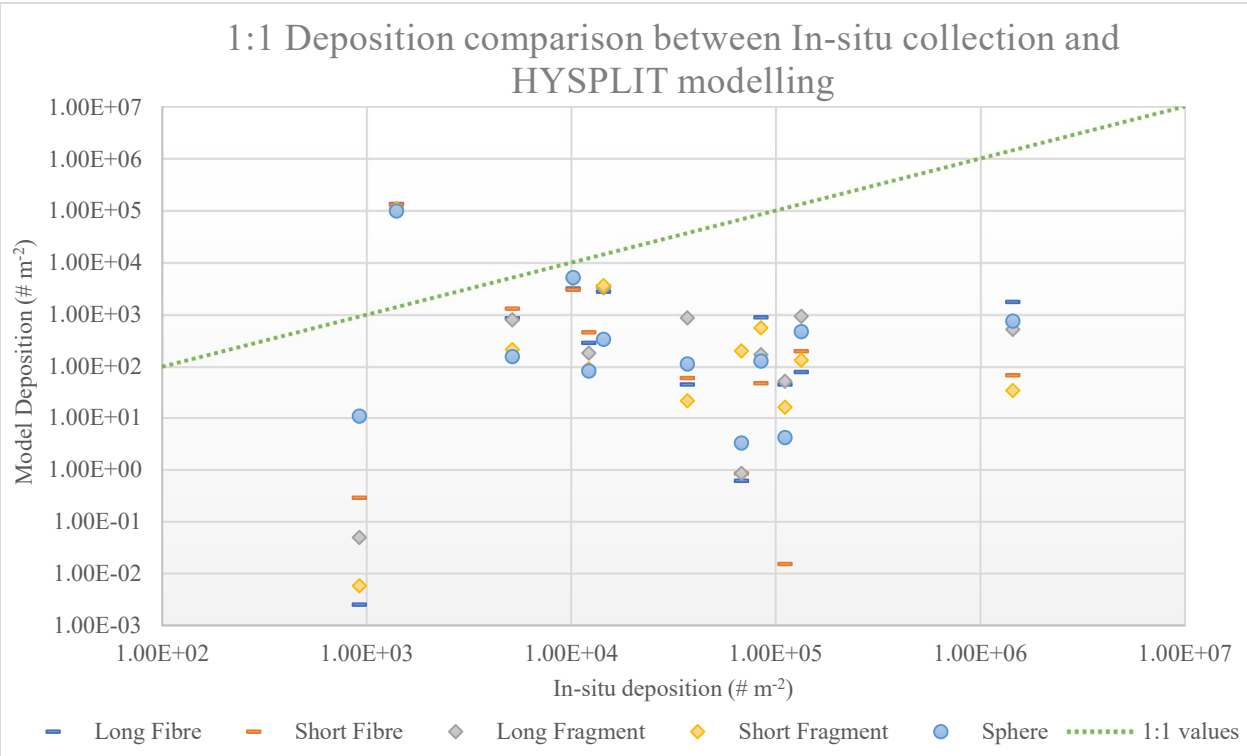

Figure 4.6: Comparison between the in-situ sampling and model deposition counts. Points below the 1:1 line indicate more in-situ deposition and points above the 1:1 line indicate more model deposition.

preliminary results from Granados-Galván et al., 2022 found microplastics in an abundance of 9.2 to 51.4 particles per litre of meltwater (# L^{-1}). The mass amount in HYSPLIT reported the highest values in the Canadian Arctic compared to the other locations, ranging from 1.29×10^{-10} µg m^{-2} in Alert to 2.01 µg m^{-2} in Yellowknife. The trend in Yellowknife was also notable in that the mass was similar for each shape modelled. Converting the results from here and the in-situ studies into number per area was required to compare the data effectively.

An assumption was made that each litre of meltwater corresponds to particle deposition on 0.01 m^2 of snow (assuming a meltwater density of 1 kg L^{-1}) to convert the results from the in-situ studies by Bergmann et al., 2019 and Granados-Galván et al., 2022. The results from Allen et al., 2019 were kept in their original units of particles per metre squared per day (# m^{-2} d^{-1}) and extrapolated to find the deposition over the same period as used in this thesis (28 days). The results from work here required a more in-depth analysis of the particle sizes deposited onto each location. Each of the five shapes was converted from the mass to the number of particles per metre squared. The density used in the conversion was kept the same as previously discussed at 1.26 g cm^{-3}. The deposition for all particle sizes was analyzed to determine the total number deposition at each in-situ collection site. All values were converted into the number of particles per metre squared (# m^{-2}) and displayed in Figures 4.5 and 4.6. Since the deposition was initially reported in mass units, some locations had number deposition amounts of less than one particle per metre squared. These data were still included in Figures 4.5 and 4.6 as the total number of particles per area depends on the time analyzed, which was only reported by Allen et al., 2019, as they utilized passive samplers for microplastic collection.

Comparing the studies demonstrates the differences in deposition between locations. The values gathered from Bergmann et al., 2019 in the European Arctic region were much higher than those from the HYSPIT model across all locations, shapes, and sizes, except at Ice Floe 2, where no in-situ plastics were found. The absence of deposition can be seen in Figure 3.1, as very few areas of the European Arctic recorded deposition nearby. In the Pyrenees Mountains, the results gathered by Allen et al., 2019 were still larger than those reported by HYSPLIT (minimum 2.0 times larger), although the magnitude difference was less than Bergmann et al., 2019 in the European Arctic (minimum 4.0 times larger). The values found by Granados-Galván et al., 2022 were closer to those reported by HYSPLIT, with the range of number deposition

overlapping the number of microplastics found from the in-situ collection. This result could be expected since the emission sources, and the in-situ locations were in North America rather than across the Atlantic Ocean, as were the studies by Allen et al., 2019 and Bergmann et al., 2019. The modelled values reported in Yellowknife ranged from 71.5 to 97.8 times the number found by Granados-Galván et al., 2022 depending on the particle shape. The results from Cornwallis Island and Alert found more plastics in the in-situ collection than from HYSPLIT. On Cornwallis Island, the highest number found was for the short fibres, although the maximum value was still only 25% of the total particle number found by Granados-Galván et al., 2022. While a nonzero mass was reported for each shape in Alert when converted into a number amount, most shapes had much less than one particle per metre squared of deposition. The largest number of particles recorded in Alert was 11 m^{-2} for spherical particles. The larger number of spherical particles compared to other shapes is likely due to differences in transport to such extreme latitudes and the small sample area used.

The model setup can explain the reasons for the low count of particles in Alert. The modelling time of one month, along with the choice to use July for meteorological data, may have contributed to limiting the overall transport of particles to the extreme northern regions. The mean northern hemisphere jet stream speed and position is typically further north and weaker over the summer months compared to winter. The average jet latitude range over North America in summer and winter is approximately 50°N to 54°N and 38°N to 41°N, respectively [Hallam et al., 2022]. Wind speeds follow for summer and winter around 38 m s^{-1} to 41 m s^{-1} and 57 m s^{-1} to 59 m s^{-1}, respectively [Hallam et al., 2022]. A longer model runtime that includes multiple seasons should be used to find more accurate results at specific locations and account for changes in particle transport due to seasonal variability in synoptic and global scale winds. Future studies of particle transport should include seasonal aspects as a primary focus to better understand the degree of variability due to seasonal changes in meteorological conditions. Furthermore, a true conversion of the model results to a number deposition would require emissions based on number amount rather than mass.

The comparison between the three in-situ studies and this thesis work shows large differences in the number of deposited microplastics. The biggest limiting factor in comparing the studies by Bergmann et al., 2019 and Allen et al., 2019 was the considerable distance

between the study sites and the closest emission point set in HYSPLIT. As such, the range of number amounts from the HYSPLIT model can be considered the potential contributions of microplastic pollution from North America rather than the expected total. Furthermore, the relative contribution by the shape of particles is a more relevant factor in the review of studies than the overall amount. Some limitations of the comparison that applied to all three in-situ studies included the time of the study, the depth of collection in snow, the unknown age of microplastics in the snow, the method used to convert litres of meltwater to the area, and the method used to analyze the samples in each study. The primary factors involved in the HYSPLIT results include the model run time, meteorological conditions, and the grid resolution, as each value was reported as an average of the total deposition within a grid space. Considering the factors involved, Figure 4.5 should be used as a trend analysis and be viewed cautiously as a definite result of expected deposition values.

4.2 Size and Shape Factor

From the multiple deposition and particle distribution plots in the previous results section, the size and shape of particles have a reasonable effect in modifying the atmospheric transport of microplastics when analyzed from a visual perspective. This section focuses on the numerical data from the HYSPLIT model to get more concise details on the exact differences and the implications of the results found.

4.2.1 Deposition Area, Sum and Extent

The primary method to determine precise differences between the 140 sizes and shapes was to separate the deposition amounts into plots by the total deposition area. Figure 4.7 shows the total deposition area by particle size and shape. The minimum deposition amounts were kept the same as in the results section, representing the total area with deposition greater than 0.1 μg m^{-2} for the model runtime. Figure 4.8 shows the total deposition area of the particles again, although the particles are displayed by volume to account for differences in particle mass.

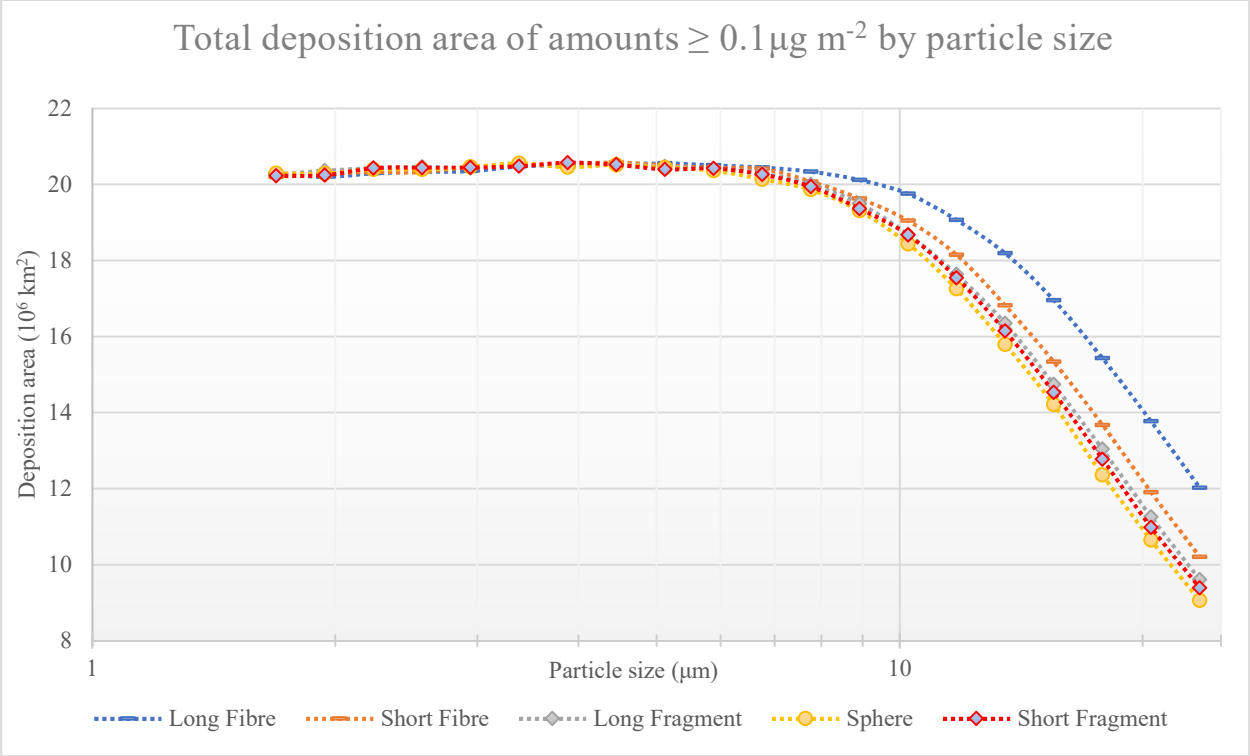

Figure 4.7: Lined Scatterplot of the total deposition of the five different shapes according to the size of the particles up to 23.5 µm. The deposition area is labelled in millions of square kilometres.

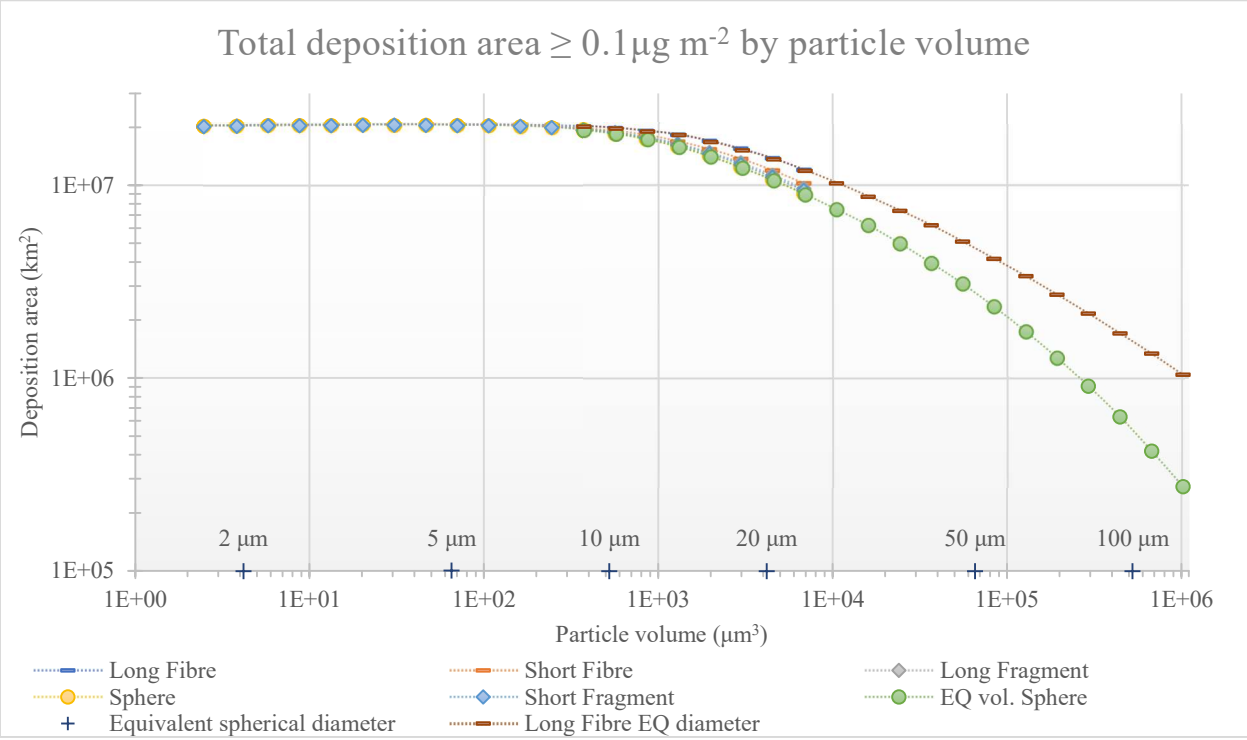

Figure 4.8: Logarithmic scatterplot comparing the total deposition area between shapes according to the volume of each shape. In this plot the sphere of equivalent volume is included to give comparison to the long fibre particles.

In Figure 4.7, there is a significant difference in the total deposition area by shape as the particle size increases. A divergence in deposition area by shape occurs for particles larger than ~6 μm. For particles between 1.68 μm and 5.88 μm, the difference between the largest and smallest deposition areas of all shapes is only 0.8%. All shapes had the largest deposition area at a size of 4.5 μm, with the short fibres having the largest area of 2.06×10^{7} km^2; however, the difference in the area between all five shapes varied by only 0.30%, or 6.1×10^{4} km^2. At particles greater than 6 μm, the difference between shapes becomes very apparent. At all sizes from greater than 5.88 μm to 23.53 μm, the extent of deposition area is correlated with the length of the particle. The spherical particles had the lowest deposition area, followed by the short and long fragments and short and long fibres. At the largest particle size of 23.53 μm, the long fibre appears to be an outlier compared to the other four shapes. Numerically, the difference in area between the sphere and the short fibre is 12.7%. In contrast, the difference between the short and long fibre is greater at 17.8%. Using the spherical particle as a control, Figure 4.9 shows the percent difference in deposition area for each shape at all particle sizes. Combined with Figures 4.7 and 4.8, Figure 4.9 shows how the shape affects the deposition area much more at larger particle sizes. Particles less than 5.88 μm show no distinguishable trend in the deposition area by particle shape. The fragments vary slightly by deposition area with increasing size, and at most, the long fragments cover 6.1% more area than the spherical particles at the largest size of 23.53 μm. From the figures shown, the shape is an essential factor in modelling the deposition area of atmospheric microplastic transport for larger size particles from 6.76 μm to 23.53 μm, with longer fibrous particles showing the greatest change in deposition area compared to spherical particles.

Figure 4.8 shows the deposition area compared to the particle shape and volume. At all comparable volumes plotted, the spherical particles deposited over a smaller area than the longer fragments and fibres. As the volume increases, the rate at which the particles diverge in area also increases. At the smallest particle volume modelled (2.84 μm^3), the area covered by a spherical particle is 100.1% of that of the long fibres, while at the largest particle volume (1.03×10^{6} μm^3), the deposition area of the spheres is only 26% of the total area of the long fibres despite having the same volume. This extreme disparity between the two shapes raises further questions on the processes involved in how shape affects the transport of microplastics. The results in Figure 4.8 also demonstrate further reasoning as to why there were very few, if any, spherical particles

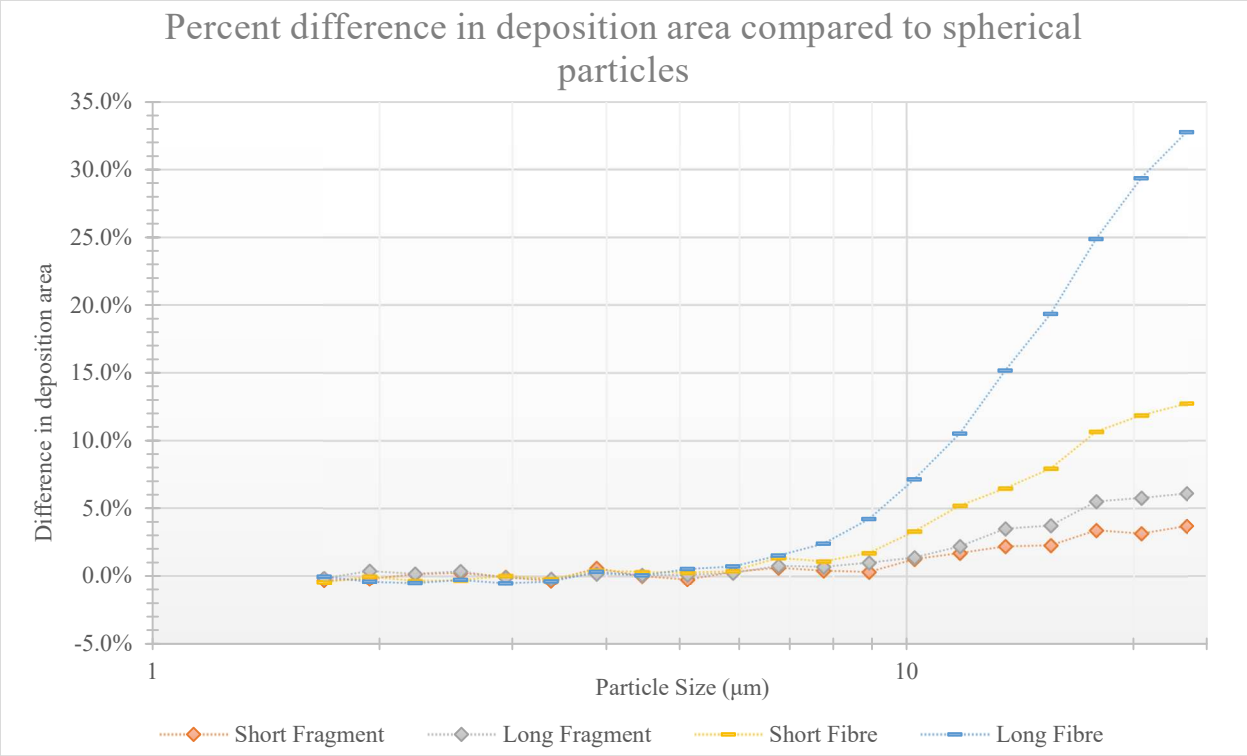

Figure 4.9: Relative difference in the deposition area for cylindrical shaped particles compared to the spherical particles. A value less than 0% indicates less area covered compared to a spherical particle, while greater than 0% indicates a larger area.

found in the studies of remote microplastics by Bergmann et al., 2019, Allen et al., 2019, and Granados-Galván et al. All three studies found fragmented and fibrous particles, however, with the minimum detectable size of 11 µm, no collected plastics were in the PM_{10} size range. When considering that microplastics are produced by mechanical abrasion or chemical breakdown of larger plastics, perfectly spherical particles should be rare, especially for particles greater than PM_{10} in size. The rarity of such perfect shapes and the decreased transport area compared to more fragmented and fibrous shapes follow the findings from the remote in-situ studies. The remaining short fibre and fragments follow a similar trend when analyzing the particles according to volume. The total deposition area differs between shapes as the particle volume exceeds roughly 200 μm^3, although the relative changes by volume depend on the shapes included in the comparison. The more similar the shape, the larger the particles can be before a significant difference in the deposition area occurs. When comparing spherical particles to long fibres, the volume of 200 μm^3 shows the smallest possible volume where differences in deposition amount are apparent. Using the particle volume to compare the deposition shows the difference in area between shapes while accounting for the different masses of the particles and

reinforces the results found that the shape of a particle impacts the total transport distance and area. The maximum transport distance of particles by shape and size is slightly more complex to identify due to the use of multiple emission points. Figure 4.10 shows the maximum transport distance of particles at a fixed deposition amount to identify differences in travel distance by particle shape and size.

Figure 4.10 shows the maximum latitudes and longitudes with deposition greater than 0.1 μg m^{-2} recorded for all particle shapes and sizes. Overall, there is a slightly positive trend of increasing maximum latitude as the particle size increases. The average maximum latitude of deposition for all shapes at the smallest particle size (1.68 μm) is 81.3° N, moving further north to 83.2° N at the largest particle size (23.53 μm). The spread of the maximum latitudes ranges from 74.6° N to the domain limit at 90° N, for a spread of 15.4°. Unlike the plots of total deposition area in Figures 4.6 and 4.7, there is no identifiable pattern to find which latitude each subsequent size or shape of a particle will reach. The mean particle latitude shows a slight increase as the particles become more fibrous, with the spheres having the southernmost average maximum and the short and long fibres having the northernmost. Table 4.4 below shows key statistics for maximum latitude and longitude from all particle shapes. The ability to use the particle shape and size to predict the furthest latitude is generally unreliable here, as statistical data analysis shows a coefficient of determination (R^2) ≤ 0.5 for all shapes.

There is considerable variability in the maximum latitude when reviewing the data. The short fibre at 2.56 μm size and the long fibre at 2.94 μm size recorded deposition up to the domain border at 90° N, while the extent of particles at sizes both smaller and larger followed by the tighter latitude spread of the other particle shapes. The data presented indicates an increase in total distance travelled as the particles become more fibrous, looking at the minimum and maximum latitudes by shape. The outliers and the variability associated with the points of maximum latitude suggest that other factors play a more significant role in determining the extent of microplastic transport by latitude and make determining the location of maximum transport extremely difficult. Such factors could include the local meteorological conditions, emission locations, and the time of emissions, impacting the furthest latitude of deposition from a given set of emitted particles.

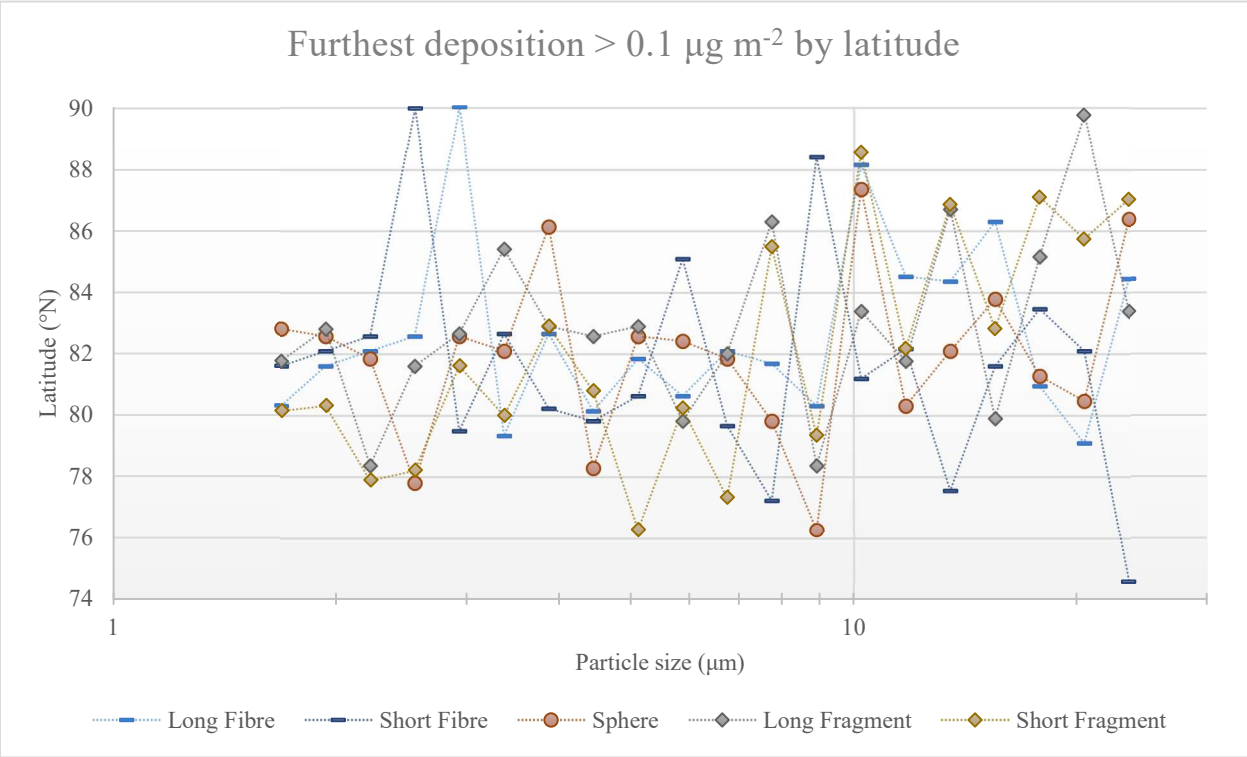

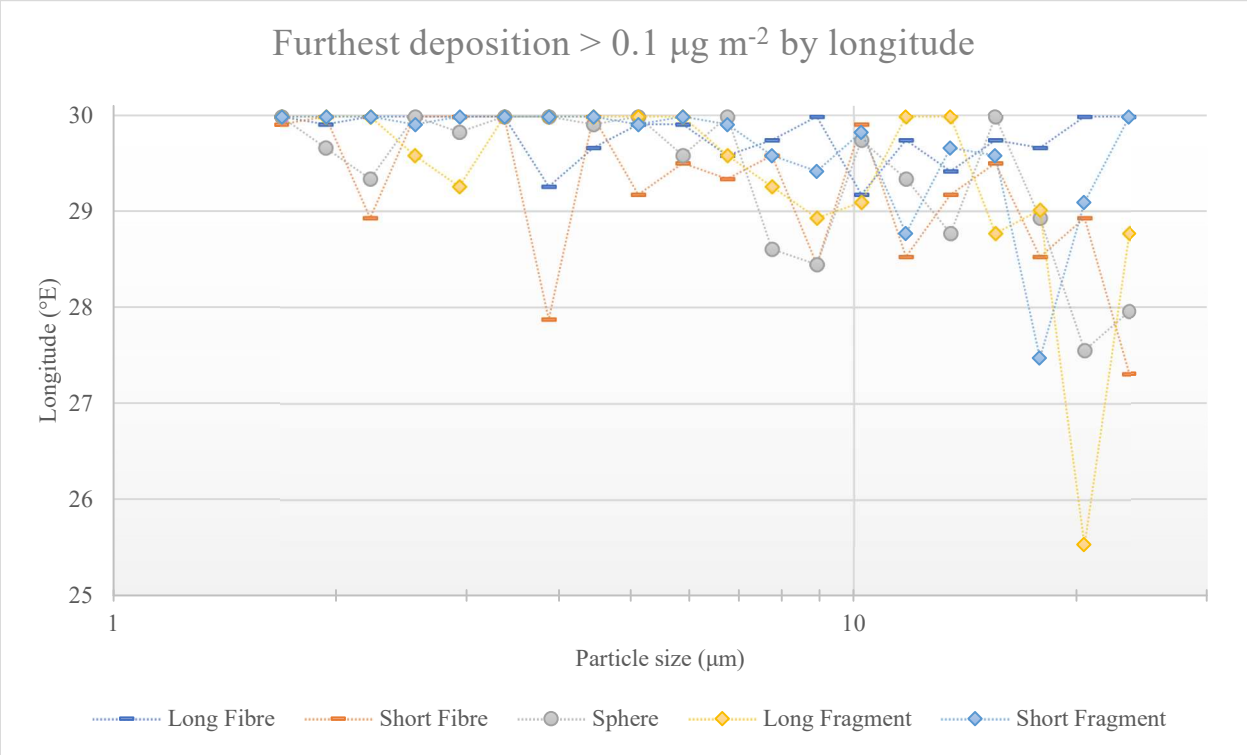

Figure 4.10: a) The most northern point of deposition recorded with amounts ≥ 0.1 µg m^{-2} for each particle size and shape. b) The most eastern point of deposition recorded with amounts ≥ 0.1 µg m^{-2} for each particle size and shape.

Table 4.4: Statistics calculated from the maximum latitude and longitude data as presented in Figure 4.10. The values are calculated using all twenty particle sizes per shape.

Latitude	***Sphere***	***Short Fragment***	***Long Fragment***	***Short Fibre***	***Long Fibre***
Mean (° N)	81.9	82.0	82.9	81.6	82.7
Standard Deviation (°)	2.76	3.66	2.81	3.52	2.89
Range (°)	11.1	12.3	11.4	15.4	10.9
Minimum (° N)	76.3	76.3	78.4	74.6	79.1
Maximum (° N)	87.4	88.6	89.8	90.0	90.0

Longitude	***Sphere***	***Short Fragment***	***Long Fragment***	***Short Fibre***	***Long Fibre***
Mean (° E)	29.4	29.6	29.4	29.2	29.8
Standard Deviation (°)	0.75	0.61	1.02	0.77	0.25
Range (°)	2.43	2.51	4.46	2.67	0.81
Minimum (° E)	27.6	27.5	25.5	27.3	29.2
Maximum (° E)	30.0	30.0	30.0	30.0	30.0

The longitude plot shows far less spread in the maximum deposition location than the latitude plot. The average longitude for all shapes at 1.68 μm is 29.9° E, and at 23.53 μm moves slightly west to 28.2° E. The furthest spread between longitudes is from 25.5° E to 30° E, for a spread of 4.5°. One major limiting factor in the analysis of the maximum deposition by longitude is that 39 of the 100 points are located at the edge of the model domain at 30° E. By comparison, the latitude plot has only two points reaching the northernmost limit of 90° N. Many points at the domain edge indicate particles are transported much further longitudinally, which can be expected as the prevailing winds are more zonal when taken over a long period. The domain also limits a complete analysis of the potential transport distance, as particles would likely travel further east if the domain were extended. The available data shows a noticeable decrease in the maximum longitude for particles as the size increases between 15 μm and 23 μm for all shapes, excluding the long fibres and short fragments. The long fibres remain with maximums consistently east of 29.2° E, while the deposition of short fragments varies at larger particle sizes. The remaining three shapes show a general trend of decreasing maximum distance with a larger size. The use of particle size to predict the maximum extent of travel longitudinally is slightly more reliable than latitudinally, however, this may result from many data points reaching the domain limit. The highest longitudinal R^2 value of 0.73 is found with the average values of all

particle shapes and sizes. Each shape had a significantly lower coefficient than the average combined value, again indicating the difficulty and uncertainty in predicting the extent of maximum deposition based solely on the particle shape. Improvement in predicting the furthest transport distance can be made in a future study by restricting emissions to a single location and tracking particle transport over a longer period.

The analysis of maximum transport distance is helpful as it provides more details on deposition variability by particle shape. It can be used to compare to in-situ studies and as a reference to guide further modelling of microplastics. Longer fibrous particles tend to travel further latitudinally and longitudinally from the emission source points than shorter, more spherical particles. Thus, remote locations would likely find more fibres when collecting and analyzing microplastic samples, especially for particles larger than PM_{10}.

4.2.2 Atmospheric Lifetime

Another difference in the transport by shape is the microplastic particles' atmospheric lifetime. The model was separated into three starting emission times throughout July 2021 to analyze the atmospheric lifetime of particles and attempt to average extreme meteorological factors from the results. The particle sizes of 2.56 μm and 20.48 μm were selected as the sizes used in the analysis. Figure 4.11 below shows the percent of mass deposited as a time series over several days. The results from the three different model times were averaged together to reduce meteorological factors and other errors in the total deposition. The error bars plotted in Figure 4.11 represent the standard error for each day.

Reviewing Figure 4.11, there are apparent differences in the deposition ratios by the total atmospheric lifetime and particle shape. The smaller particles show minimal variation by shape, with 0.93% being the most significant difference in the daily deposition ratio. By contrast, the larger particles have significantly more variation between shapes in the first few days of the time series plot. Day one shows the largest difference of 10% by mass between shapes and follows in order, with the long fibres depositing the least and spheres depositing the most. The trend in Figure 4.11 follows those previously found and further highlights how shape can affect the transport of the particles. At larger sizes, more fibrous particles have longer atmospheric

lifetimes than spherical particles and can be transported to a greater distance over a longer time, given the same meteorological conditions. The analysis of particle deposition over time also shows how a portion of smaller particles can remain entrained in the air for a much longer time than the larger particles, allowing for further reach into remote locations as carried by winds.

For numerical data of the atmospheric lifetime of particles by shape and size, a half-life of the particles was found based on the points from Figure 4.11. A modified formula for half-life was utilized, as the deposition of particles does not follow the conventional formula for finding half-life and follows in Equations 4.3 and 4.4 as

$$N(t) = N(0)e^{-\lambda t} + c \tag{4.3}$$

$$t_{1/2} = \frac{\ln\left(\frac{0.5 - c}{N(0)}\right)}{\lambda} \tag{4.4}$$

where $N(t)$ is the remaining airborne mass ratio after t days, $N(0)$ being the initial airborne mass ratio, λ being a decay constant for deposition, $t_{1/2}$ being the time for half of the mass to deposit in days, and c being an additional factor for correcting the ratio of airborne to deposited mass such that $N(t = 0) = 1$. Utilizing the data in Figure 4.11, the half-life for the two-particle sizes was found for all shapes (using a least-squares fit) and presented in Table 4.5.

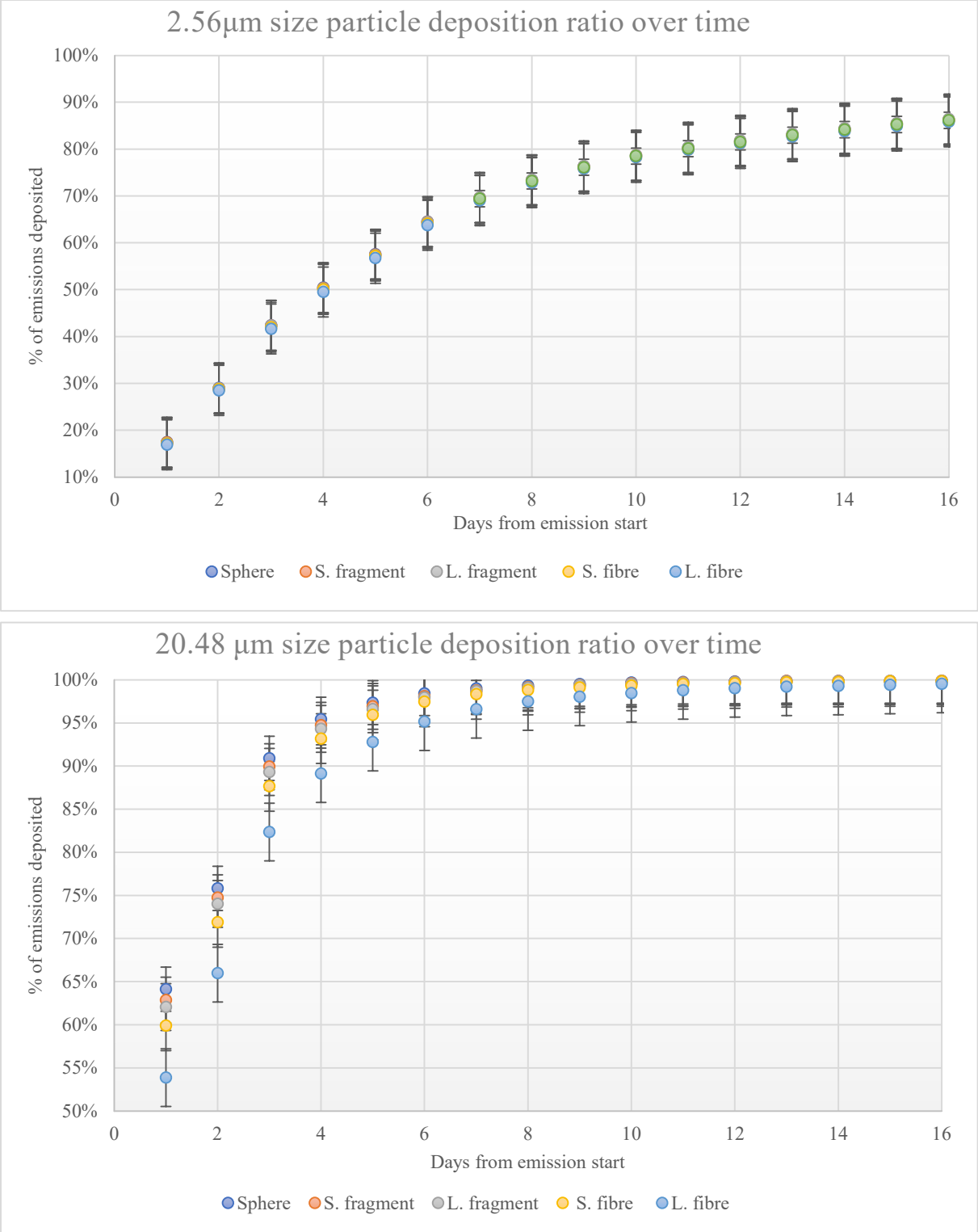

Figure 4.11: Plotted average values for each particle shape as a timeseries to identify atmospheric lifetime of particle by shape. Particle emissions occurred on days 1 and 2 for all instances. a) Particles of 2.56 µm size for days 1 to 16 including all five shapes. b) Particles of 20.48 µm size for days 1 to 16 including all five shapes.

Table 4.5: Time for 50% of particles to deposit after emission starts using Equations 4.1 and 4.2. The effective half-life of particles.

2.56 µm size	***Sphere***	***Short fragment***	***Long fragment***	***Short fibre***	***Long fibre***
$t_{1/2}$ ***(days)***	3.89	3.89	3.91	3.94	3.98
20.48 µm size	***Sphere***	***Short fragment***	***Long fragment***	***Short fibre***	***Long fibre***
$t_{1/2}$ ***(days)***	0.794	0.828	0.850	0.911	1.11

The values found here for the atmospheric half-life of microplastics represent an estimate from the model results. They demonstrate the half-life difference between the particle shapes at specified particle sizes. The main conclusion from the analysis remains in line with the results found in previous sections. Smaller-sized particles show slight variation in the half-life by shape. In comparison, larger particles show a clear pattern that longer, more fibrous particle shapes remain within atmospheric circulation for longer than shorter, more spherical particles. The difference in half-life between shapes at 2.56 µm particle size is 0.09 days (approximately 2 hours), for a relative change of 2.3% longer half-life for long fibres compared to spheres. The difference between shapes at 20.48 µm particle size is much larger at 0.364 days (approximately 8.7 hours), for a relative change of 72% longer half-life for the long fibres than the spherical particles. An increase in the atmospheric half-life of 72% by shape would allow fibrous particles to travel and deposit over a much wider area than more spherical particles, as seen in Figure 4.8. Increasing the number of model runs and the time period would give greater confidence in the accuracy of the results and reduce the impact of varying meteorological conditions and associated confounding variables. The modelling study by Evangeliou et al., 2020 gives more definitive atmospheric lifetime values for TWP, with $PM_{2.5}$ and PM_{10}-sized particles having an atmospheric lifetime of 28 ± 2.7 days and 8.3 ± 1.0 days, respectively. The method of calculating atmospheric lifetime differs between this thesis and the study by Evangeliou et al., 2020, as they base calculations on steady-state conditions for atmospheric particle concentrations. Estimating steady-state conditions can be made from the same data used to find the half-lives for the particles in this thesis for a constant emission rate. The half-life was used to find steady-state conditions by applying a constant daily emission rate and associated deposition rate until the daily change in the mass of airborne particles was less than 1%. The time required for steady-state conditions for spherical particles of 2.56 µm and 20.48 µm diameter is around 22 days and 4.5 days, respectively. In this thesis, $PM_{2.5}$-sized particles are represented by a single particle

diameter of 2.56 μm for the atmospheric lifetime, so a shorter lifetime is expected than found by Evangeliou et al., 2020 as they utilized a range of particle sizes. There is no direct comparison for larger particles at 20.48 μm diameter, though the shorter lifetime and a half-life of ~0.8 days are lower than the lifetime of PM_{10}-sized TWP, as can be expected from the increase in settling velocity.

4.3 Fluid Dynamics

A key difference between particle shapes not yet mentioned is their behaviour as they are transported through the atmosphere. The dynamic processes investigated for discussion include the settling velocity, flow scales, and turbulent effects on the particles. More detail from Figure 2.6 is given on the settling velocity of particles, and the relevant fluid dynamics and choice of turbulent parameterization within the model are provided. The analysis of particle fluid dynamics provides details connecting the results found and how they can be used to further microplastic research.

4.3.1 Settling Velocity

Investigating the relationship between the settling velocity of a particle (Figure 2.6) and the deposition area (Figure 4.7) gives a new perspective on the reach of microplastics without directly showing their size. Figure 4.12 displays the settling velocity of all 140 particle sizes (found with Equations 2.4 to 2.7) against the deposition area.

The relationship between the settling velocity of a particle and the deposition area appears to be correlated, although the type of relationship changes depending on the velocity and suggests many factors are involved. The five shapes with sizes between 1.68 μm and 23.53 μm have a minimum and maximum settling velocity of 6.93×10^{-3} cm s^{-1} and 1.27 cm s^{-1}, respectively. The maximum deposition area occurs for all particle shapes with a settling velocity between 0.0177 cm s^{-1} and 0.144 cm s^{-1}. Particles with a settling velocity less than 0.0177 cm s^{-1} had slightly less deposition area, however, at most, this resulted in 1.9% less area at a settling velocity of 9.51×10^{-3} cm s^{-1}. The sphere of equivalent volume had a much greater settling

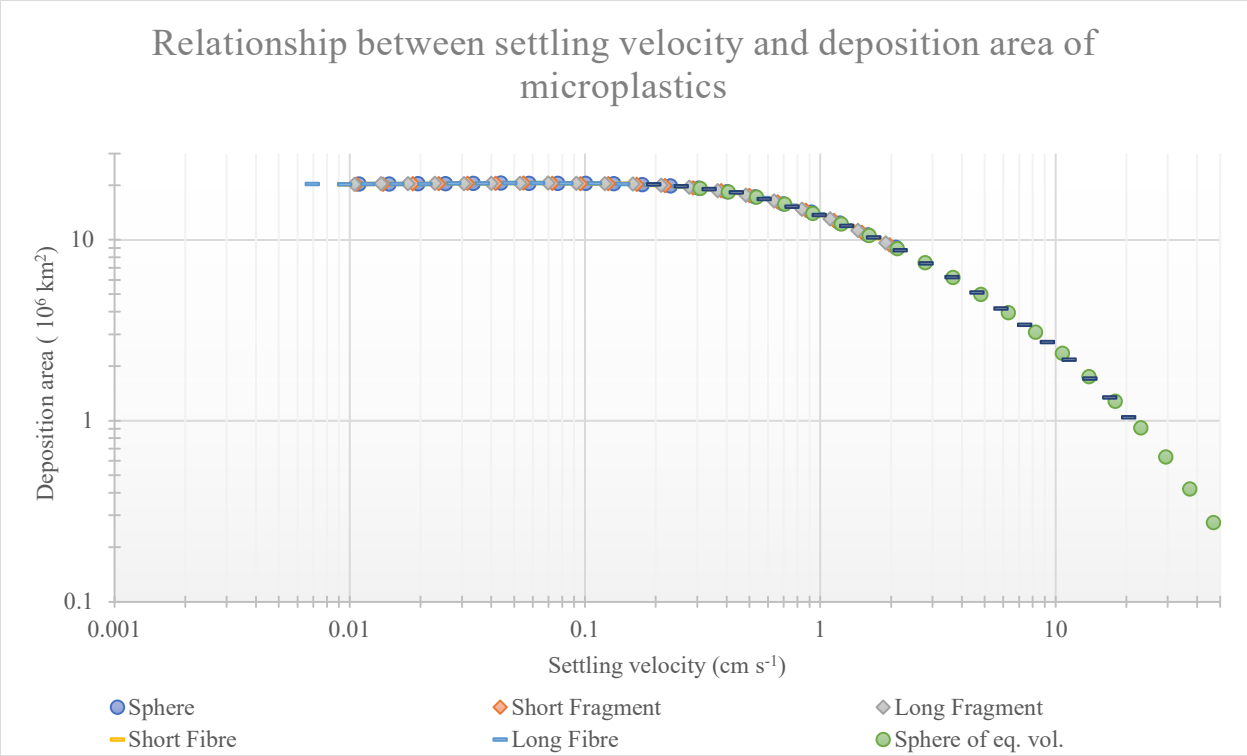

Figure 4.12: Scatterplot of all 140 particles' deposition area against the respective settling velocity. The deposition area is in units of million kilometres squared. Settling velocity of the particles is found using Equations 2.4 to 2.7.

velocity than all other particles and ranged from 0.310 cm s^{-1} to 46.8cm s^{-1}. A fibre of the same size had settling velocities ranging from 0.20 cm s^{-1} to 20.4 cm s^{-1}. The equivalent volume sphere's deposition area fits with the trend of other particle shapes as the settling velocity increases. As the particles' velocity exceeds 0.25 cm s^{-1}, the deposition area decreases rapidly and at a similar rate for all particle shapes. Due to the many factors involved in particle transport and the relative complexity of the dynamics involved, it is challenging to assign equations in finding the deposition area based on settling velocity alone. Further influences on deposition area include the chosen minimum mass amount of 0.1 µg m^{-2}, the turbulence parameterizations in Equations 1.11 to 1.20, the boundary layer's stability, and the deposition in Equations 2.1, 2.2, 2.8, and 2.9.

4.3.2 Deposition by Type

The figures and equations mentioned in this section thus far only include the dry deposition component and ignore any influence of the wet deposition. The wet deposition of

particles depends entirely on changing meteorological conditions as particles are transported through cloud layers and precipitation regions, adding further complexity to deposition analysis. Altogether, these factors and associated equations affect the total deposition area, making a single equation estimating deposition area by particle settling velocity impractical. The conclusion from these data suggests that particles with a settling velocity between 0.01 cm s^{-1} and 0.25 cm s^{-1} deposit over the largest area regardless of particle shape. The particles within this range should be investigated further to provide more details on the deposition area and transport extent.

Comparison of the deposition of microplastics separated into dry and wet adds greater detail to the results and provides possible reasoning for differences in the deposition by particle size. Spherical particles with diameters of 2.56 μm and 20.48 μm were utilized for this comparison, and four model runs with different types of deposition are shown below in Figure 4.13. The primary focus of these data was located over the continental United States and compared the dry deposition of particles to the combined wet and dry deposition. At 2.56 μm diameter, there is a significant increase in deposition amount when wet and dry deposition are included in the model parameterization. Dry deposition alone shows sparse pockets mostly confined to areas near emission sources. These results indicate that small particles in the $PM_{2.5}$ range highly depend on wet deposition to deposit high amounts at locations away from their sources. Larger particles of 20.48 μm diameter deposit at a comparable rate for both dry and combined wet and dry deposition. Visual differences in the plots are challenging to identify and suggest that dry deposition accounts for most of the total deposition for particles greater than PM_{10} in size.

Numerically, particle size heavily influences the deposition by type. For particles of 2.56 μm diameter, the total dry deposition by mass was 10.1% of the combined wet and dry deposition. By comparison, dry deposition of the larger 20.48 μm diameter particles accounted for 93.7% of the total deposition by mass. A third size of 10.24 μm diameter was assessed to provide data between the two extremes. Dry deposition at 10.24 μm diameter accounted for 67.1% of the total combined deposition. From these data, it is possible to distinguish how the deposition is related by type and particle size. Particles larger than PM_{10} mainly deposit due to dry deposition, while particles in the $PM_{2.5}$ size range deposit primarily by wet deposition.

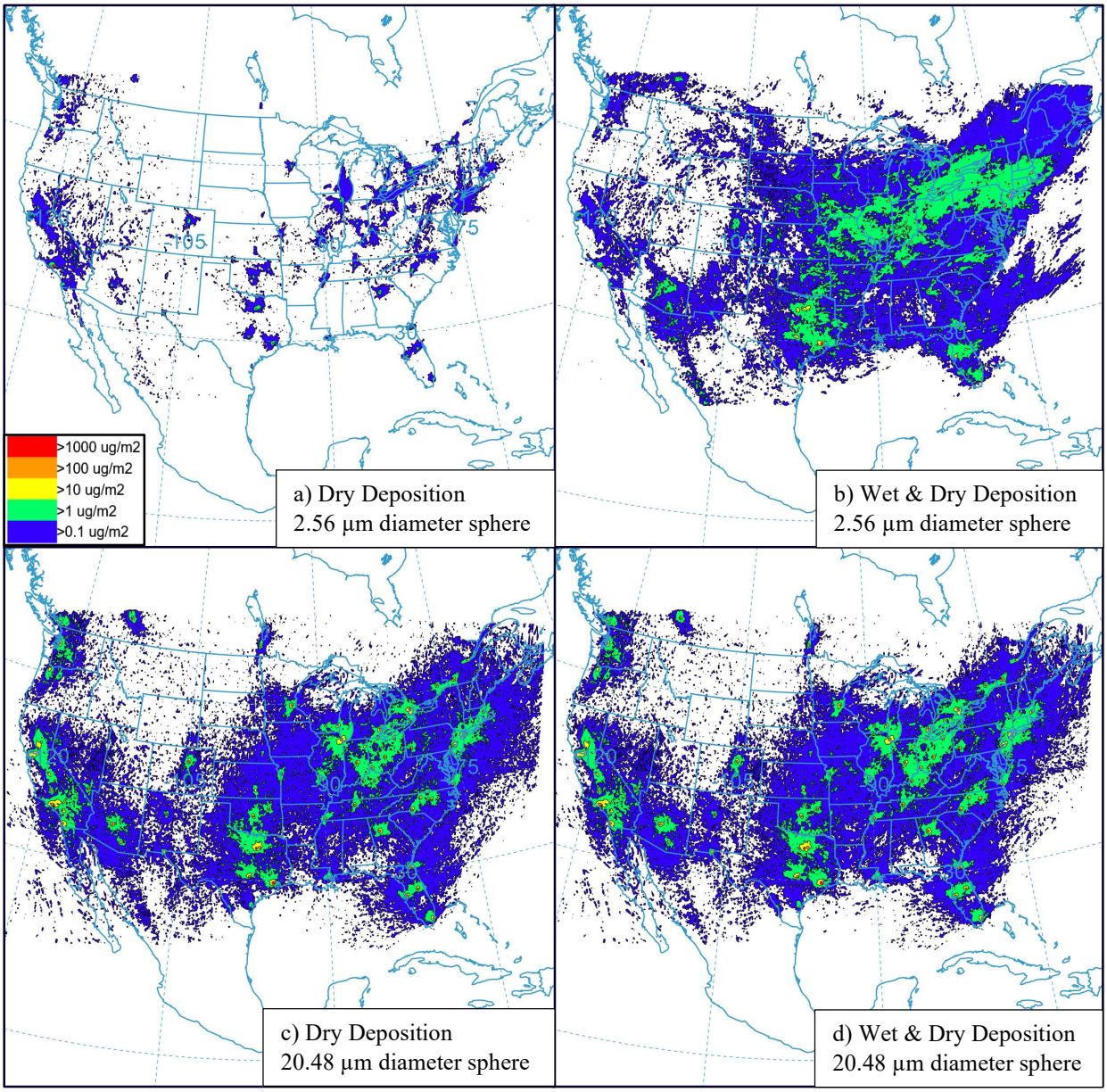

Figure 4.13: Deposition amounts over continental North America examining the differences between deposition by type.

Particles larger than $PM_{2.5}$ but within the PM_{10} size range vary significantly in proportion of deposition by type and are likely highly dependent on all meteorological conditions for transport range and area.

Comparing the deposition by type demonstrates the dependence of precipitation for particles of various sizes to deposit. Wet scavenging is the primary driver of microplastic deposition in the $PM_{2.5}$ size range. The total transport distance and deposition area for the smallest particles likely rely more on precipitation than the shape of the particle transported. In

regions with little precipitation, such as the Arctic, $PM_{2.5}$-sized microplastics could travel greater distances and deposit higher amounts when precipitation occurs. The dry deposition has a greater effect on larger particles, likely due to their higher settling velocity. Comparing the change in deposition area by particle size and shape in Figure 4.8, differences by shape primarily show at particle diameters greater than 6 μm. Possible reasoning for this could involve the type of deposition, as the proportion of dry deposition increases with larger particle diameters, and thus the settling velocity becomes an increasing factor in the extent of microplastic transport. Further study involving dispersion models and in-situ collection of microplastics will provide greater evidence for the hypothesized effects of dry deposition and precipitation on remote microplastic deposition.

4.3.3 Flow Scales and Turbulence

The settling velocity is only one of many aspects involved in the dynamics of atmospheric microplastic transport. The flow scales and turbulence modify the settling velocity (Figure 2.6) and factor into the final deposition velocity of particles. The particle Reynolds number found using Equation 2.6 largely determines the flow type around the particles. Finding the particle Reynolds number helps to give further insight into how the particles behave as they are transported through the atmosphere. Figure 4.14 displays the particle Reynolds number for the five modelled shapes and is labelled with the different flow regimes following Bagheri and Bonadonna, 2016. Stokes regime is applicable for Reynolds numbers ≤ 0.1, and an intermediate regime exists for Reynolds numbers > 0.1. Examining the plotted data, the relation between the Reynolds number and the particle diameter is the same as the settling velocity in Figure 2.6. For particles larger than ~30 μm in size, the flow begins to change into an intermediate regime. The primary difference between the two flow regimes that are of concern here is the change in the drag coefficient (C_D) derived by Stokes law. Fortunately, the shape factors applied through Equations 2.4 and 2.5 by Ganser, 1993, correct the numerical solutions for non-spherical particles through the two flow regimes. Figure 4.15 shows the relation between Stokes' law and the modified equations used in this thesis by comparing Reynolds number to the drag coefficient.

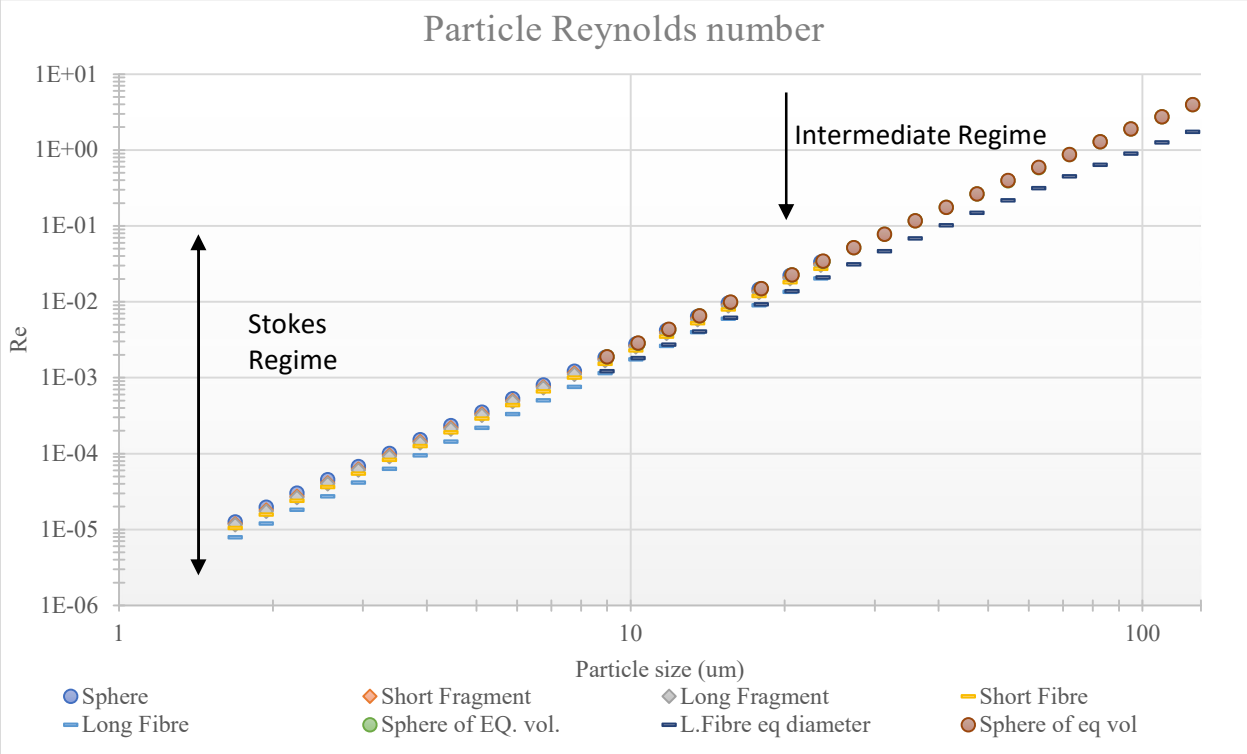

Figure 4.14: The particle Reynolds number for each shape of microplastic modelled. The Stokes and Intermediate regime labelled indicate the type of flow around the particle. Re < 0.1 follows well for Stokes' law when calculating the coefficient of drag on a particle.

Stokes' law fits well for spherical particles at Reynolds number ≤ 0.1 and begins to underestimate the value as the particle size increases. The base Stokes' law underestimates the Reynolds number for all other particle shapes compared to the corrected values using Equations 2.4 to 2.7. The difference in drag coefficient for spherical particles between Stokes' law and Equation 2.5 used in this thesis is below 1% for diameters less than 15 µm and increases significantly above 5% for spherical particles larger than 35 µm. Fibrous particles have the largest difference at all sizes, with the drag coefficient of the long fibres being around 2 to 4.5 times greater when using Equation 2.5. From the equations and plots of settling velocity (Figure 2.6) and Reynolds number and drag coefficient (Figure 4.15), more detail is shown on how particles behave based on their shape. The most pronounced difference is between the long fibres and the spheres. Despite having the same volume and mass, the fibres' larger surface area dramatically increases the particles' drag, thus lowering the settling velocity compared to a spherical particle shape. Since the shape factors in Equation 2.4 alter the settling velocity at a different rate for non-spherical shapes, the magnitude difference between the shapes changes with increasing particle size. At the smallest size of 1.68 µm, a sphere has 1.6 times higher

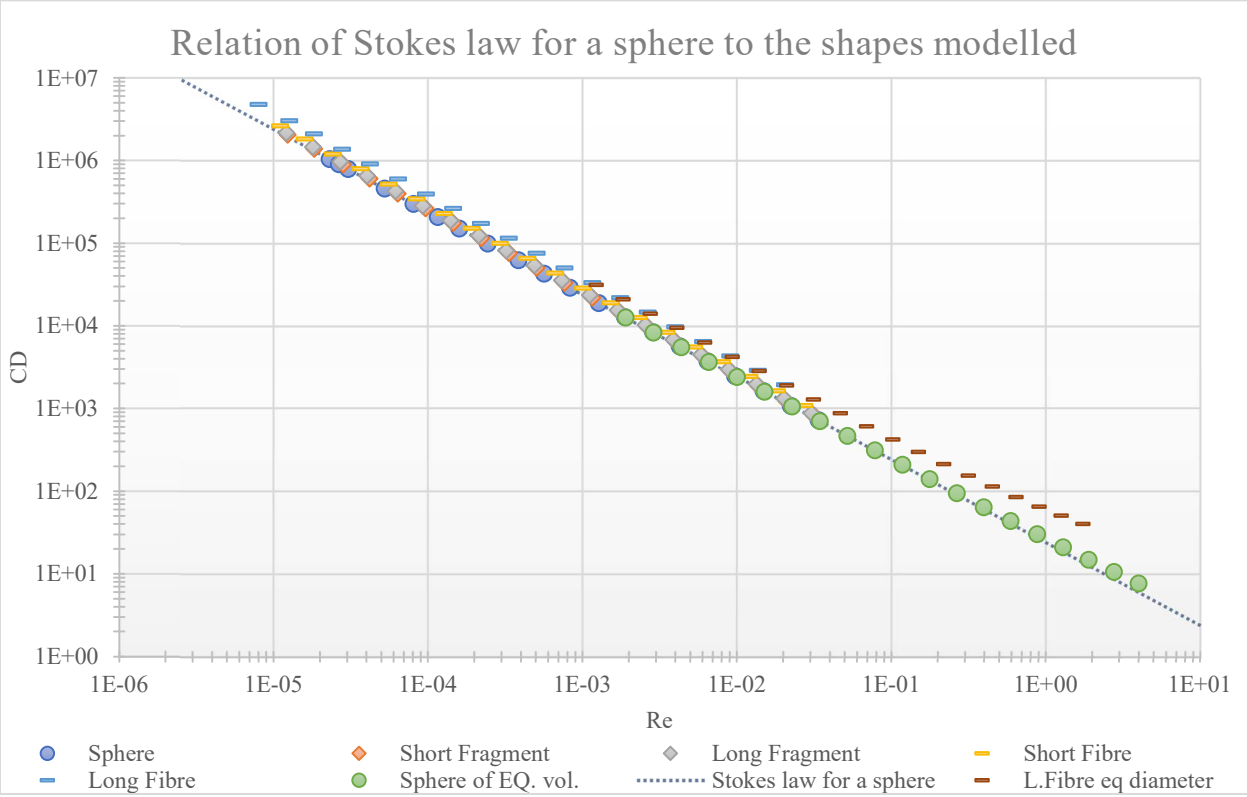

Figure 4.15: Relation between the particle Reynolds number and the drag coefficient for all 140 particle sizes and shapes. All particles have a corrected Reynolds number larger than Stokes law for a sphere, with the magnitude difference increasing as the particle size increases.

settling velocity than the long fibre (at SATP). The difference increases to 2.3 times higher velocity at 125 µm. The variation in settling velocity, Reynolds number, and drag coefficient between the two particle shapes give insight into how these particles' transport occurs and, ultimately, the extent of the deposition area, as shown in Figure 3.1.

Atmospheric turbulence affects all modelled microplastic particles as they travel, although finding the exact effects on the deposition is challenging. Equations 1.11 to 1.20 parameterize the boundary layer turbulence according to the atmospheric stability given by the stability parameter in Equation 1.10. The effect turbulence has on a particle is primarily determined by its size and shape, with smaller particles being influenced by turbulent motion more than larger particles concerning particle deposition velocity. The particle relaxation time measures how easily turbulent motion can affect a particle's trajectory. Even small atmospheric eddies can influence the settling velocity for particles on the microscale. The particle relaxation time can be used with the Kolmogorov time scale for the dissipation of the smallest turbulent

flow in the atmosphere. The equation for the particle relaxation time follows from Brennen, 2005 as

$$\tau_p = \frac{\rho_p D_{eq}^2}{18\mu}. \tag{4.4}$$

The ratio of the particle relaxation time to the Kolmogorov time scale (τ_p/τ_k) called the Stokes' number changes the velocity of a particle at a maximum when $\tau_p/\tau_k \approx 1$ [Yang and Lei, 1998]. Values less than one indicate that the particles generally follow the fluid flow, and values greater than one indicate that turbulent motion has little effect on the particles due to greater inertia. Figure 4.16 shows the Stokes' number compared to the particle size for all shapes.

All of the microplastics modelled have a Stokes' number of less than one when analyzed against a Kolmogorov time scale of small eddies in the boundary layer of $\tau_k = 0.155\ s$ [Yang and Lei, 1998]. This result suggests all particles modelled are susceptible to influence by turbulent motion at the smallest scales. As atmospheric turbulence is generally unpredictable, Stokes' numbers give a more qualitative idea of how the particle flow is affected by turbulent motion. Experimental studies, as done by Wang et al., 2018, suggest that for extremely small

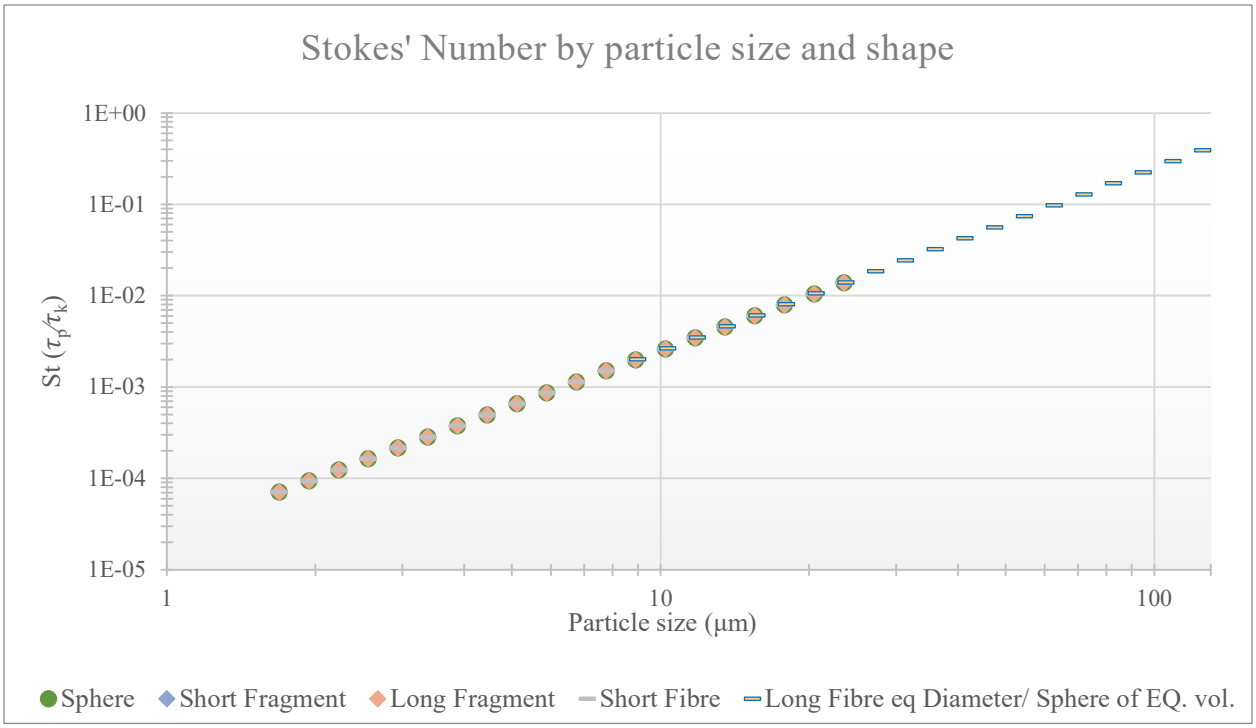

Figure 4.16: Stokes' number of particles as found using Equation 4.4. For particles with St << 1, particles generally follow the streamlines of the flow.

Stokes' numbers ($St \ll 1$), the small-scale turbulent motion slows the particles, decreasing the settling velocity, while larger eddies and turbulence can increase the settling velocity due to a sweeping effect. The largest Stokes number of particles modelled is only 0.39 for the long fibres and spheres of 125 μm size. As such, significant differences in particle deposition by shape or size found in this thesis are unlikely due to changes in particle behaviour resulting from similar turbulent effects. Additionally, the HYSPLIT model has a temporal resolution of one minute, so the turbulent velocity variance parameterizes the turbulent motion differently than would occur in the natural atmospheric environment with constantly changing conditions in the microscale.

Investigating the settling velocity and flow scales on the atmospheric transport of microplastic reveals important properties and gives insight into how the particles behave. The settling velocity significantly limits the deposition area for particles with a velocity greater than ~ 0.25 cm s^{-1}, as found by comparing the maximum deposition area. Particles with settling velocities less than ~ 0.25 cm s^{-1} had a similar deposition area within a 5% range. The tight spread of the deposition area could indicate an optimal particle settling velocity for maximizing the reach of microplastics, although further study is needed to ensure confidence that the model setup is not a limitation of the data presented in this thesis. Particles with settling velocities less than ~ 0.25 cm s^{-1} largely fall within the PM_{10} size range. As tiny particles in the PM_{10} size range significantly impact human and ecological health, the extensive transport distance of particles of all shapes at this size implies that the adverse health effects associated with microplastics are not limited to urban regions. The shape of particles and relevant numerical corrections for settling velocity must be considered when modelling atmospheric transport, as shown in Figure 4.14 and 4.15. Using Stokes' law without correcting for shape produces significant differences in the final calculated settling velocity of up to 129% for the longest fibres and risks reducing the potential deposition area.

5 -Conclusions and Future Work

This thesis investigated the atmospheric transport of microplastics using the HYSPLIT model to identify how the shape and size of particles affect the range and deposition area. The HYSPLIT model was run for July 2021 and included results on 140 particles from five shapes and twenty sizes with a range of 1.68 μm to 23.53 μm. Understanding how the shape of particles affects atmospheric transport is valuable, as microplastics have become an area of increasing concern for scientists and environmentalists due to adverse health effects across ecosystems. The results presented here contribute to understanding airborne microplastics and their deposition, provide future study recommendations and identify limitations in the data.

The burden of atmospheric microplastics varies depending on the size and shape of the particles modelled. TWP smaller than 6 μm had negligible difference (< 1%) in the total deposition area by shape. The deposition area of plastics larger than 6 μm greatly depended on the particle's shape, with the long fibrous particles depositing over the largest areas. The greatest differences between shapes occurred at the largest size (23.53 μm), where the long fibres deposited over a 32% larger area than spherical particles of equal size. Further comparison of shape between larger long fibres and spheres of equivalent volume revealed significant differences in deposition area and transport distance at all sizes, including the smallest equivalent diameter fibre modelled of 1.68 μm (volume 380 μm^3). The long fibres deposited over a 5.6% larger area than the equivalent volume spheres, even at the smallest diameter, increasing to 281% at a size of 125 μm. To this extent, the results indicate that future modelling of atmospheric microplastic transport should consider the shape of particles as a significant factor in the transport distance and deposition amount. It is imperative to accurately model these particles' reach, as tiny microplastics in the PM_{10} and $PM_{2.5}$ size ranges have the highest potential to cause adverse effects on human health due to their ease of ingestion. Microplastics smaller than 10 μm have the potential to cause the most damage, as these particles can potentially cross cell membranes, enter the bloodstream, and access many organ systems [Leslie et al., 2022]. As results in this thesis indicate particles larger than 6 μm deposit increasingly depending on the shape, larger particles in the PM_{10} size range are of heightened concern. The ability to accurately model the distribution of microplastics transported through the atmosphere is crucial to finding the potential effects across the planet.

Many considerations must be made when attempting to model real-world atmospheric microplastic emissions and transport. Here, the type of microplastics chosen was TWP, as many studies quantifying TWP production and emission into the environment have been published [Evangeliou et al., 2020, EPA, 2014, Panko et al., 2019, Sommer et al., 2018, Baensch-Baltruschat et al., 2020, Kole et al.,2017]. The limiting factors with choosing TWP are the variability in the emissions and uncertainty in the atmospheric burden of TWP by size. Such uncertainty includes the estimated proportion of TWP produced in the PM_{10} size range of 5% by mass, the VKT data and associated TWP emission rates by lightweight (7 to 360 mg km^{-1}), and heavy vehicles (107 to 1500 mg km^{-1}), and the relative burden of TWP as a source of atmospheric microplastics at up to 84% by mass over the western United States [Brahney et al., 2021]. While the uncertainty in emissions impacts the total deposition amounts found in the results, the deposition area ratio by microplastic shape should remain relatively constant regardless of emissions. Uncertainty in the emissions is found by comparison to other research and is highlighted by the differences between the results here and measurements by Evangeliou et al., 2020, Bergmann et al., 2019, and Granados-Galván et al., 2022. Other aspects of the model, such as time of year and meteorological conditions, similarly play a prominent role in the spatial distribution of deposition. As July 2021 was chosen for the model period, a synoptic scale summer flow dominated the wind patterns. The overall deposition area and location would be different than if another season was chosen to model. In future work, a longer period of modelling that includes multiple meteorological seasons would improve the consistency in the deposition area. Furthermore, choices in the meteorological models need greater consideration, as there was a noticeable pattern of increased deposition in the regions bordering the HRRR and NAM domains (Figure 3.1). Reasons for this deposition pattern primarily involve changes to the meteorological conditions as the spatial and temporal resolution of the data changes. The temporal resolution decreases between the HRRR and NAM from 1 hour to 3 hours, while the spatial resolution decreases between the HRRR, NAM, and GFS from 3 km to 12 km to ~28 km.

The parameterization of the model and the chosen equations and variables all affected how the model performed. The parameterization of turbulence likely affected the overall deposition, however, the difference in the deposition by particle shape due to turbulence was likely negligible due in part to the small Stokes' numbers found (≤ 0.39). The choice of wet deposition variables affects the total deposition, as it had the potential to undercount or

overcount deposition caused by variations in precipitation rate provided by the meteorological data. The total deposition area would likely be altered little by changing this parameter for the largest particles, as they are dominated by dry deposition (settling velocity) at 93.7% by mass. Smaller particles, primarily within the PM_{10} size range, would be most affected by changes in wet deposition values, as dry deposition of 2.56 μm particles accounted for 10.1% deposition by mass. The change in the wet deposition by shape at equal particle sizes is a possible topic for future research and would help to further quantify deposition proportion by type, especially within the PM_{10} size range.

Future studies can apply the results found here and in related research to expand the understanding of microplastic transport's atmospheric burden. As previously mentioned, microplastics in the $PM_{2.5}$ and PM_{10} size range are of heightened concern due to their potential to infiltrate living tissue. Focusing on particles with a size of 1 μm to 10 μm over a longer model time will provide more detail on the effects of shape on particle transport and reduce uncertainty in the results found here. In-situ collection studies can utilize these data as a comparison tool for the smallest particle sizes, as most sampled particles to date have been larger than 11 μm. Improving models of atmospheric microplastic transport will benefit in defining the possible effects and range of these pollutants on the global climate and across ecosystems.

References

Abbasi, S., Keshavarzi, B., Moore, F., Turner, A., Kelly, F. J., Dominguez, A. O., & Jaafarzadeh, N. (2019). Distribution and potential health impacts of microplastics and microrubbers in air and street dusts from Asaluyeh County, Iran. *Environmental pollution, 244*, 153-164.

Akhbarizadeh, R., Dobaradaran, S., Torkmahalleh, M. A., Saeedi, R., Aibaghi, R., & Ghasemi, F. F. (2021, January). Suspended fine particulate matter (PM2.5), microplastics (MPs), and polycyclic aromatic hydrocarbons (PAHs) in air: Their possible relationships and health implications. *Environmental Research, 192*, 110339. doi:10.1016/j.envres.2020.110339

Allen, S., Allen, D., Karbalaei, S., Maselli, V., & Walker, T. R. (2022, May). Micro(nano)plastics sources, fate, and effects: What we know after ten years of research. *Journal of Hazardous Materials Advances, 6*, 100057. doi:10.1016/j.hazadv.2022.100057

Allen, S., Allen, D., Phoenix, V. R., Le Roux, G., Durántez Jiménez, P., Simonneau, A., . . . Galop, D. (2019, April). Atmospheric transport and deposition of microplastics in a remote mountain catchment. *Nature Geoscience, 12*, 339-344. doi:10.1038/s41561-019-0335-5

Aves, A. R., Revell, L. E., Gaw, S., Ruffell, H., Schuddeboom, A., Wotherspoon, N. E., . . . McDonald, A. J. (2022, June). First evidence of microplastics in Antarctic snow. *The Cryosphere, 16*, 2127–2145. doi:10.5194/tc-16-2127-2022

Baensch-Baltruschat, B., Kocher, B., Stock, F., & Reifferscheid, G. (2020, September). Tyre and road wear particles (TRWP) - A review of generation, properties, emissions, human health risk, ecotoxicity, and fate in the environment. *Science of The Total Environment, 733*, 137823. doi:10.1016/j.scitotenv.2020.137823

Bagheri, G., & Bonadonna, C. (2016, November). On the drag of freely falling non-spherical particles. *Powder Technology, 301*, 526–544. doi:10.1016/j.powtec.2016.06.015

Bergmann, M., Mützel, S., Primpke, S., Tekman, M. B., Trachsel, J., & Gerdts, G. (2019, August). White and wonderful? Microplastics prevail in snow from the Alps to the Arctic. *Science Advances, 5*. doi:10.1126/sciadv.aax1157

Brahney, J., Mahowald, N., Prank, M., Cornwell, G., Klimont, Z., Matsui, H., & Prather, K. A. (2021, April). Constraining the atmospheric limb of the plastic cycle. *Proceedings of the National Academy of Sciences, 118*. doi:10.1073/pnas.2020719118

Brennen, C. E. (2005). *Fundamentals of Multiphase Flow.* Cambridge University Press.

Cai, L., Wang, J., Peng, J., Tan, Z., Zhan, Z., Tan, X., & Chen, Q. (2017, September). Characteristic of microplastics in the atmospheric fallout from Dongguan city, China: preliminary research and first evidence. *Environmental Science and Pollution Research, 24*, 24928–24935. doi:10.1007/s11356-017-0116-x

Draxler, R., & Hess, G. (1998, December). An overview of the HYSPLIT_4 modeling system for trajectories, dispersion, and deposition. *Australian Meteorological Magazine, 47*, 295-308.

Dris, R., Gasperi, J., Saad, M., Mirande, C., & Tassin, B. (2016, March). Synthetic fibers in atmospheric fallout: A source of microplastics in the environment? *Marine Pollution Bulletin, 104*, 290–293. doi:10.1016/j.marpolbul.2016.01.006

EPA. (2014). *Brake and Tire Wear Emissions from On-road Vehicles in MOVES2014.* U.S. Environmental Protection Agency, Office of Transportation and Air Quality, Assessment and Standards Division. Retrieved from https://books.google.ca/books?id=6k0tngAACAAJ

Evangeliou, N., Grythe, H., Klimont, Z., Heyes, C., Eckhardt, S., Lopez-Aparicio, S., & Stohl, A. (2020, July). Atmospheric transport is a major pathway of microplastics to remote regions. *Nature Communications, 11*. doi:10.1038/s41467-020-17201-9

Frias, J. P., & Nash, R. (2019, January). Microplastics: Finding a consensus on the definition. *Marine Pollution Bulletin, 138*, 145–147. doi:10.1016/j.marpolbul.2018.11.022

Ganser, G. H. (1993, November). A rational approach to drag prediction of spherical and nonspherical particles. *Powder Technology, 77*, 143–152. doi:10.1016/0032-5910(93)80051-b

Granados-Galván, I.-A., Kabir, A. H., Barnouin, G., Guillot, A., Malaisé, F., Silva, A. D., . . . Lu, Z. (2022). Microplastics in the Snow Depositions from Yukon, Northwest Territories andNunavut in the Canadian Arctic. *QCAR.*

Hallam, S., Josey, S. A., McCarthy, G. D., & Hirschi, J. J.-M. (2022, February). A regional (land–ocean) comparison of the seasonal to decadal variability of the Northern Hemisphere jet stream 1871–2011. *Climate Dynamics, 59*, 1897–1918. doi:10.1007/s00382-022-06185-5

Kantha, L. H., & Clayson, C. A. (2000). *Small Scale Processes in Geophysical Fluid Flows, Volume 67 (International Geophysics)* (1st ed.). Academic Press.

Kole, P. J., Löhr, A. J., Belleghem, F. V., & Ragas, A. (2017, October). Wear and Tear of Tyres: A Stealthy Source of Microplastics in the Environment. *International Journal of Environmental Research and Public Health, 14*, 1265. doi:10.3390/ijerph14101265

Kreider, M. L., Panko, J. M., McAtee, B. L., Sweet, L. I., & Finley, B. L. (2010, January). Physical and chemical characterization of tire-related particles: Comparison of particles generated using different methodologies. *Science of The Total Environment, 408*, 652–659. doi:10.1016/j.scitotenv.2009.10.016

Leslie, H. A., van Velzen, M. J., Brandsma, S. H., Vethaak, A. D., Garcia-Vallejo, J. J., & Lamoree, M. H. (2022, May). Discovery and quantification of plastic particle pollution in human blood. *Environment International, 163*, 107199. doi:10.1016/j.envint.2022.107199

Liu, K., Wu, T., Wang, X., Song, Z., Zong, C., Wei, N., & Li, D. (2019, August). Consistent Transport of Terrestrial Microplastics to the Ocean through Atmosphere. *Environmental Science & Technology, 53*, 10612–10619. doi:10.1021/acs.est.9b03427

National Centers For Environmental Prediction/National Weather Service/NOAA/U.S. Department Of Commerce. (2015). NCEP GFS 0.25 Degree Global Forecast Grids Historical Archive. *NCEP GFS 0.25 Degree Global Forecast Grids Historical Archive*. UCAR/NCAR - Research Data Archive. doi:10.5065/D65D8PWK

NOAA. (2022b). *Gridded Data Archives*. Retrieved from READY: https://www.ready.noaa.gov/archives.php

OECD. (2019). *Global Plastics Outlook: Plastics use in 2019.* Retrieved from OECD Environment Statistics (database): https://doi.org/10.1787/efff24eb-en

Panko, J., Hitchcock, K., Fuller, G., & Green, D. (2019, February). Evaluation of Tire Wear Contribution to PM2.5 in Urban Environments. *Atmosphere, 10*, 99. doi:10.3390/atmos10020099

Revell, L. E., Kuma, P., Ru, E. C., Somerville, W. R., & Gaw, S. (2021, October). Direct radiative effects of airborne microplastics. *Nature, 598*, 462–467. doi:10.1038/s41586-021-03864-x

Sommer, F., Dietze, V., Baum, A., Sauer, J., Gilge, S., Maschowski, C., & Gieré, R. (2018). Tire Abrasion as a Major Source of Microplastics in the Environment. *Aerosol and Air Quality Research, 18*, 2014–2028. doi:10.4209/aaqr.2018.03.0099

Sportisse, B. (2007, April). A review of parameterizations for modelling dry deposition and scavenging of radionuclides. *Atmospheric Environment, 41*, 2683–2698. doi:10.1016/j.atmosenv.2006.11.057

Stein, A. F., Draxler, R. R., Rolph, G. D., Stunder, B. J., Cohen, M. D., & Ngan, F. (2015, December). NOAA's HYSPLIT Atmospheric Transport and Dispersion Modeling System. *Bulletin of the American Meteorological Society, 96*, 2059–2077. doi:10.1175/bams-d-14-00110.1

Thompson, A. (2018). Earth Has a Hidden Plastic Problem-Scientists Are Hunting It Down. *Scientific American*. Retrieved from https://www.scientificamerican.com/article/microplastics-earth-has-a-hidden-plastic-problem-mdash-scientists-are-hunting-it-down/

Wang, Y., Lam, K. M., & Lu, Y. (2018, September). Settling velocity of fine heavy particles in turbulent open channel flow. *Physics of Fluids, 30*, 095106. doi:10.1063/1.5046333

Wright, S. L., Ulke, J., Font, A., Chan, K. L., & Kelly, F. J. (2020, March). Atmospheric microplastic deposition in an urban environment and an evaluation of transport. *Environment International, 136*, 105411. doi:10.1016/j.envint.2019.105411

Yang, C., & Lei, U. (1998, September). The role of the turbulent scales in the settling velocity of heavy particles in homogeneous isotropic turbulence. *Journal of Fluid Mechanics, 371*, 179–205. doi:10.1017/s0022112098002328

Zhang, J., Moran, M. D., Zheng, Q., Makar, P. A., Baratzadeh, P., Marson, G., . . . Li, S.-M. (2018, July). Emissions preparation and analysis for multiscale air quality modeling over the Athabasca Oil Sands Region of Alberta, Canada. *Atmospheric Chemistry and Physics, 18*, 10459–10481. doi:10.5194/acp-18-10459-2018

Zhang, J., Zheng, Q., Moran, M. D., Gordon, M., Liggio, J., Makar, P., . . . Taylor, B. (2012). Improvements to SMOKE Processing of Canadian On-Road Mobile Emissions.

Zhang, Y., Kang, S., Allen, S., Allen, D., Gao, T., & Sillanpää, M. (2020, April). Atmospheric microplastics: A review on current status and perspectives. *Earth-Science Reviews, 203*, 103118. doi:10.1016/j.earscirev.2020.103118